RF pulse designs for signal recovery in T_2^*-weighted functional magnetic resonance imaging

by

Chun-yu Yip

A dissertation submitted in partial fulfillment
of the requirements for the degree of
Doctor of Philosophy
(Electrical Engineering: Systems)
in The University of Michigan
2007

Doctoral Committee:

      Professor Douglas C. Noll, Co-Chair
      Professor Jeffrey A. Fessler, Co-Chair
      Professor Alfred A. Hero III
      Associate Professor John M. Pauly, Stanford University

To my parents, who saw me through the most difficult times.

ACKNOWLEDGEMENTS

First and foremost, I thank Professor Douglas C. Noll and Professor Jeffrey A. Fessler for being such incredible advisors to me during my graduate study at the University of Michigan. Doug and Jeff have a lot in common. Both of them are very knowledgeable, supportive, kind, willing to spend time with students, and liberal in letting students choose their lines of research. Yet, they have left different footprints in my journey. Doug has a very warm personality, and he is willing to step beyond being just a fine academic advisor and befriend with me on a personal level. To him I can share personal issues candidly, and he always gives me his willing hand when I stumble. On the other hand, Jeff is rigorous, critical, and he always sees the subtleties in research problems. His enthusiasm about my work has never faltered over the years. He gets me going when the going gets tough. I am immensely grateful to both Doug and Jeff. There is no other dynamic duos that I would rather work for.

I also thank Professor Alfred O. Hero and Professor John M. Pauly from Stanford in my dissertation committee. Before joining the fMRI Lab, I worked with Professor Hero for a year on a magnetic resonance force microscopy project. It was him who introduced me to the world of research and demonstrated being a good researcher. I am grateful to Professor Pauly for agreeing to be in my committee. It is a tremendous honor to have him on board, as he is the undisputed guru in the field of RF pulse design in MRI. In the Psychology Department, I thank Professor John Jonides for teaching me cognitive neuroscience, and offering me the "night-time job" of investigating the relationship between musical training

and cognitive abilities.

The fMRI Lab has been a great working environment for me. Not to mention the huge windows in our spacious student office, there I have also found collaborations, discussions, and close friendships. Sangwoo Lee has been my best friend over the years. From teaching me what a "system matrix" is to giving me advice on thesis writing, he has been a great mentor to me. He always stands by me like an elder brother. Christie Kim, another Korean labmate, offered me tremendous emotional support over the years. I use to joke that she is my "godmother". Will Grissom has been my ideal buddy in RF pulse designs. Our collaborations have always been pleasurable and productive, resulting in a good number of publications that we co-author. I thank Valur Olafsson for IT tips and valuable discussions on image reconstruction, Greg Lee and Alberto ("Towi") Vazquez for their help in pulse sequence programming, Kiran Pandey for organizing birthday parties that warm our hearts, and also Luis Hernandez for his help in my scanner experiments. Finally, I thank Scott Peltier, Chuck Nicholas, Keith Newnham, Eve Gochis for keeping the lab running from day to day.

Outside the fMRI Lab, I have been very fortunate to have good friends who keep me in perspective. Mohan Dhanasekaran and Barry Stiefel were fabulous housemates who shared with me moments of joy and tears. I thank Yi Cui, Chien-chi Chen, Yu-chun Kao and Chandrika Kalluri for their friendship, and Jason Ueda, Shirley Poon and Ray Tsai, and Sandeep Tata for the good times we had in the student club. Also, I must say thank you to my volunteer subjects for participating in my scanner experiments.

Finally I owe my eternal gratitude to my family and my parents. My aunts and uncles have been very supportive even though they are far away in Hong Kong. My parents' love basically survived me through the most difficult times in 2006 and 2007. They give me so much and never ask for anything in return. I love them from the bottom of my heart.

Chun-yu Yip

Ann Arbor, Michigan

14 September, 2007

TABLE OF CONTENTS

LIST OF FIGURES

ABSTRACT

RF pulse designs for signal recovery in T_2^*-weighted functional magnetic resonance imaging

by

Chun-yu Yip

Co-chairs: Douglas C. Noll, Jeffrey A. Fessler

In blood-oxygenation-level-dependent (BOLD) functional magnetic resonance imaging (fMRI) using T_2^* contrast, images suffer from loss of signals at brain regions close to the air-filled cavities in the human head. The artifact arises from magnetic field distortion caused by the magnetic susceptibility difference between air and brain tissues, and hampers functional studies of important brain regions such as the orbito-frontal cortex. In this research project, I investigate two methods of designing radio-frequency (RF) pulses that can recover the signal loss. In addition to slice selective excitation, both pulse designs "precompensate" the through-plane dephasing that occurs between excitation and data acquisition. One method uses three-dimensional selective excitation to achieve these goals. The other method uses spectral-spatial selective excitation, and relies on the assumption that through-plane field gradient is spatially correlated with field offset. All these sophisticated pulses are numerically designed using the iterative conjugate gradient method. To facilitate those design methods, I also propose new techniques applicable to general pulse designs, such as frameworks for pulse computation acceleration and joint design

of excitation k-space trajectory and RF pulse. With phantom and human experiments, I demonstrate that the methods are efficacious in signal recovery, but not without costs and hurdles to overcome.

CHAPTER 1

Introduction

This research project is an attempt to solve a notorious image artifact problem in functional magnetic resonance imaging (fMRI) – signal loss observed in images of the inferior brain close to the air-filled cavities in the human head. There are various stages in the magnetic resonance (MR) image acquisition process at which the problem can be tackled. In particular, we focus on the magnetization excitation stage, which is essential before magnetization can be manipulated and nuclear magnetic resonance (NMR) signals can be detected. We try to answer the following questions: How can we *design* the RF pulse waveform, such that while it achieves basic magnetization excitation, it can also counteract the signal loss mechanism, and hence recover signal loss? How effective are the sophisticated pulse designs? What are their limitations? What is the cost involved (in terms of pulse computational time, for example) in achieving signal recovery? In answering these questions, we can evaluate the feasibility of actually implementing those designs in routine fMRI studies. In this thesis, I am going to explore two major pulse design approaches that hold great promise for signal recovery. To facilitate those pulse designs, I also postulate new pulse design techniques that can be generally applied to other MR excitation applications. At the end, I will try to answers those questions.

Let us begin the journey with some background of fMRI, and the mechanisms of how

its image contrast and artifacts arise.

1.1 Functional magnetic resonance imaging

FMRI refers to the technique of acquiring a time series of MR images that capture the indirect effects of neuronal activities on local cell metabolism, blood volume, flow, or oxygenation. Along with high-resolution anatomical brain images, functional images allow localization of brain functions that evolve over the duration of an experimental paradigm. Such capability of functional localization has proven to be invaluable to researchers in neuroscience, psychology, psychiatry, and beyond. Potentially, fMRI can also be applied clinically for patient diagnosis [1].

1.2 T_2^*-weighted BOLD fMRI

There are many contrast mechanisms for fMRI. Among them, T_2^*-weighted, blood-oxygenation-level-dependent (BOLD) image contrast has by far been the most popular since its inception in the early 90's [2]. Neuronal activities, such as action potential generation and neurotransmitter release, initiates complex interactions among local blood flow, blood volume, and oxygenation level [3–5]. The process through which neuronal activity triggers such interaction is not fully understood [6]. However, we know that the net effect of the interaction is a decrease in regional deoxyhemoglobin concentration, which has been attributed to an increase in cerebral blood flow that exceeds oxygen consumption [1]. This phenomenon causes an increase in regional blood oxygenation level, which manifests as increase in blood's T_2^* value, one of the MR signal decay time constants. Therefore, T_2^* image contrast can be used to infer neuronal activities, although not without uncertainties [6].

The relationship between blood oxygenation and T_2^* relaxation can be explained by

the physical phenomenon of *magnetic susceptibility*. Magnetic susceptibility underlies BOLD image contrast, but at the same time, it is the culprit for various kinds of artifacts in functional images.

1.2.1 Susceptibility-induced BOLD contrast

The degree to which a material magnetizes in the presence of an external magnetic field is quantified by its magnetic susceptibility. In an applied external field (H_0), the field within a material (B_0) is given by

$$(1.1) \qquad\qquad B_0 \;=\; \mu(1 + \chi)H_0,$$

where μ is the permeability of free space and χ is the magnetic susceptibility of the material. The value of magnetic susceptibility can be positive or negative (paramagnetic or diamagnetic, respectively). Based on Eq. 1.1, if placed in an uniform external field, a paramagnetic object "reinforces" the applied field, and hence the field strength within the object is higher than that applied. In contrast, a diamagnetic object "opposes" the field and hence inside the object the field is weaker than applied. The magnetic field is distorted because of such variation of field strength from inside to outside of the object, particularly at the interfaces of susceptibility differences.

Blood plasma has susceptibility value close to 0, deoxyhemoglobin (deoxy-Hb) is strongly paramagnetic, while oxyhemoglobin (oxy-Hb) is slightly diamagnetic. Therefore, when blood is placed in a uniform magnetic field, red blood cells containing deoxy-Hb create more severe field distortion than those containing oxy-Hb do. Hence, local field homogeneity correlates positively with the relative concentration of oxy-Hb to deoxy-Hb.

The Larmor relationship,

$$(1.2) \qquad\qquad\qquad \omega \;=\; \gamma B_0,$$

states that the angular frequency of magnetic spin precession (ω) is proportional to the magnetic field strength (B_0) by the gyromagnetic ratio (γ). In the presence of field inhomogeneity, excited spins precess at slightly different frequencies. It leads to spatial dispersal of the phase of spins and contributes to T_2^* relaxation. Therefore, neuronal activity leads to rise in local blood oxygenation level, which improves local field homogeneity, finally resulting in slower T_2^* relaxation (higher T_2^* value).

Because of this causal relationship, fast pulse sequences that are T_2^*-sensitive can be used to detect blood oxygenation changes over time, which indicate neuronal activities. Gradient-echo (GRE) echo-planar imaging (EPI) [7] or spiral [8] sequences are typically used. With relatively long data readout, these sequences acquire a vast amount of k-space data in each repetition time (T_R), providing high temporal resolution for capturing oxygenation dynamics. To maximize T_2^* contrast in the images, the echo time (T_E) used in the sequences should be set to the average T_2^* value of tissue [9]. At 3 T, for example, T_E is commonly set to 30-50 ms, which is much longer than the typical values in other imaging methods. Also, high main field strength is preferable because of the resulting gain in T_2^* sensitivity [10–12]. Change in blood oxygenation level leads to a larger change in T_2^* if the main field is stronger, and thus results in larger contrast-to-noise ratio.

1.2.2 Susceptibility-induced image artifacts

At relatively high field, GRE EPI and spiral sequences with long readout and T_E provide good susceptibility-induced T_2^* contrast and good temporal resolution. However, such sequences also lead to acquired images that are vulnerable to susceptibility-induced artifacts. The primary artifact origin is the *bulk magnetic susceptibility* (BMS) difference between brain structures and air cavities in the head, which leads to macroscopic, morphology-based main field inhomogeneity (Fig. 1.1). Because of the Larmor relation-

ship (Eq. 1.2), field inhomogeneity leads to spatially-variant resonance frequency shifts, or "off resonance", throughout the head. BMS-induced off resonance lead to various kinds of image artifacts, plaguing brain regions such as the orbital frontal and inferior temporal cortices, which reside close to the air-filled sinuses and mastoid air cells (middle ears) [13].
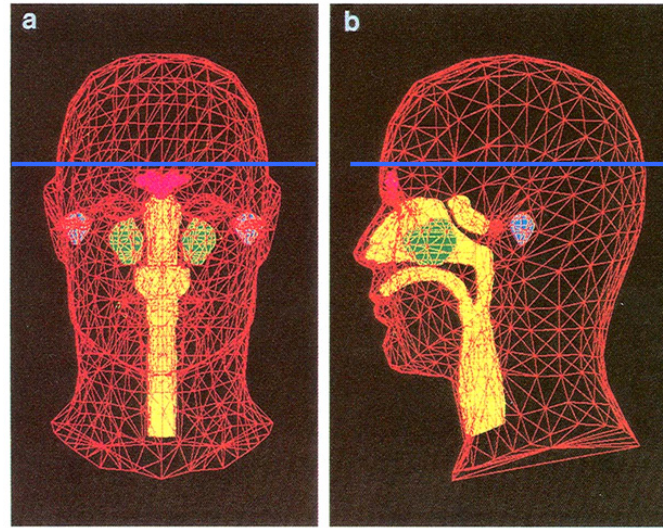
Figure 1.1: Computer model of the human head in front view (a) and side view (b). It shows the frontal sinus (magenta), sphenoid sinus (yellow), maxillary sinuses (green), mastoid air cells (blue), the nasal and oral cavities, as well as the trachea (yellow). Image acquired at the indicated slice location is susceptible to signal loss artifacts. (Adopted from Ref. [14], Copyright 1996, reprinted with permission of Wiley-Liss Inc., a subsidiary of John Wiley & Sons, Inc.)

Geometric distortion (EPI) or blurring (spiral)

One category of image artifacts caused by BMS-induced off resonance originates from phase errors during k-space data readout. Resonance frequency offsets lead to extra revolution of magnetization spins, creating phase errors that accumulate throughout the entire readout. With conventional reconstruction methods, images from such contaminated data are geometrically distorted in case of EPI, or blurred in case of spiral imaging. These artifacts are particularly prominent in functional images acquired with long readout (hence longer phase accumulation) and high field strength (hence faster phase accumulation).

They compromise images of brain regions proximal to air cavities, where the main field is highly distorted. Fortunately, they are highly corrigible in the image reconstruction process (for example, [15–17]). In this work, we do not aim to correct for this category of artifacts, and therefore will not elaborate further.

Signal loss

Signal loss artifact is also common in functional images, because of the long T_E values necessary for T_2^* contrast. The major culprit of signal loss is BMS-induced *intravoxel* field inhomogeneity, which results in intravoxal spin dephasing. If some spins within a voxel volume are in a higher field than the others and hence precess faster, then, during T_E, they will steadily gain phase relative to the slow ones. The intensity of an image voxel is proportional to the vector sum of all spins within the voxel volume. Therefore, intravoxel dephasing lead to vector cancellation, which results in partial or even complete voxel intensity drop. In 2D imaging, the slice thickness is often larger than the in-plane pixel dimensions. In that case, through-plane dephasing is usually the dominant cause of signal loss relative to in-plane dephasing. Similar to geometric distortion or blurring, signal loss plagues images of brain regions close to air cavities (Fig. 1.2). Signal loss is dominant at the affected brain regions, but it is difficult to recover in reconstruction. This project concerns the recovery of signal loss caused by through-plane dephasing.

1.3   Modeling signal loss

By incorporating field inhomogeneity in the MR signal equation [18], we can mathematically describe how through-plane dephasing causes signal loss. Let $B_0(\mathbf{r})$ be the actual field strength at location $\mathbf{r} = (x, y, z)^T$, which is spatially non-uniform because of distortions. With the frequency of the RF pulse (ω_{rf}) tuned to the Lamour frequency of
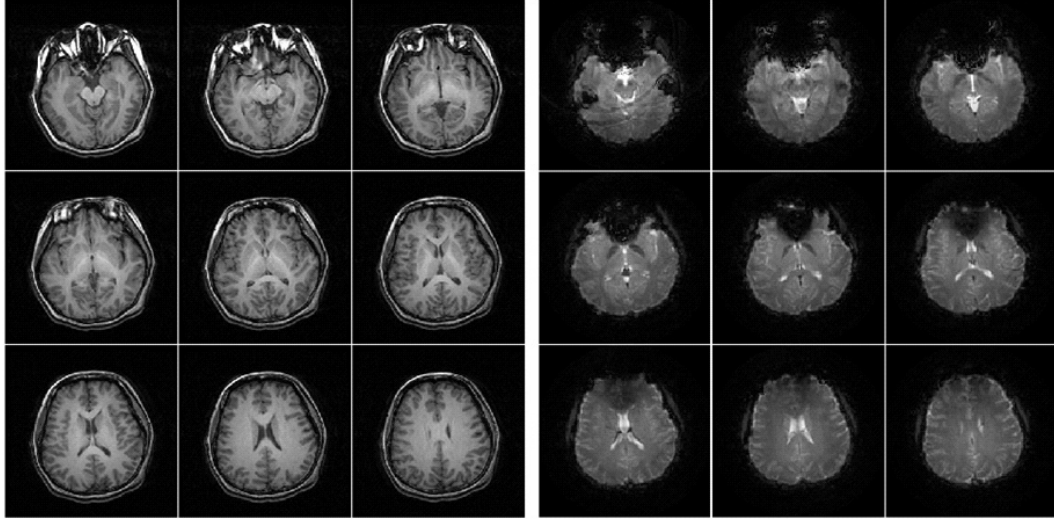
Figure 1.2: Left: T_1-weighted anatomical brain images acquired with a spoiled-gradient-recall (SPGR) sequence. Right: Corresponding functional images acquired with a GRE sequence (matrix size $= 128 \times 128$, $T_E = 30$ ms, 2 spiral-out interleaves, thickness = 5 mm). At inferior frontal and temporal brain regions proximal to the air cavities, signals are lost due to magnetic susceptibility difference between air and tissue.

water, the field offset at $\mathbf{r}$ is given by

$$(1.3) \qquad \Delta B_0(\mathbf{r}) \;\; = \;\; B_0(\mathbf{r}) - \frac{\omega_{rf}}{\gamma}.$$

Ignoring magnetization relaxation effects, we can incorporate the field offset into the MR signal equation:

$$(1.4) \qquad s(t) \;\; = \;\; \int_V f(\mathbf{r})e^{-\imath\gamma\Delta B_0(\mathbf{r})(t+T_E)}e^{-\imath 2\pi(\mathbf{k}(t)\cdot\mathbf{r})}d\mathbf{r}$$

where $\imath = \sqrt{-1}$, $f(\mathbf{r})$ denotes the three-dimensional (3D) object being imaged, V denotes the entire volume that the receive coil is sensitive to, and $\mathbf{k}(t) = (k_x(t), k_y(t), k_z(t))^T$ is the *trajectory* in spatial frequency, or k, space. Assume two-dimensional (2D) imaging with slice selection in the z dimension, with slice profile $p(z)$. If the object is separable into a 2D object ($q(x, y)$) and the slice profile, then

$$(1.5) \qquad s(t) \;\; = \;\; \int_{x,y}\int_z q(x, y)p(z) \cdot e^{-\imath\gamma\Delta B_0(\mathbf{r})(t+T_E)}e^{-\imath 2\pi(k_x(t)x+k_y(t)y)}dx\,dy\,dz.$$

Now, we Taylor expand $\Delta B_0(\mathbf{r})$ in the z dimension at the center of slice (z_0) and retain only the first two terms:

$$(1.6) \qquad \Delta B_0(\mathbf{r}) \quad \approx \quad \overline{\Delta B_0}(x,y) + g_z(x,y) \cdot (z - z_0),$$

where $\overline{\Delta B_0}(x,y)$ and $g_z(x,y)$ are the z-direction mean and gradient of frequency offset at in-plane location (x,y), respectively. By substituting Eq. 1.6 into Eq. 1.5 and rearranging, we have

$$
s(t) \quad \approx \quad \int_{x,y} \left[\underbrace{\int_z p(z-z_0) e^{\imath \gamma g_z(x,y)(z-z_0)(t+T_E)} dz}_{l(x,y,t)} \right] q(x,y)
$$

$$(1.7) \qquad\qquad\qquad\qquad \cdot e^{-\imath \gamma \overline{\Delta B_0}(x,y)(t+T_E)} e^{-\imath 2\pi (k_x(t)x + k_y(t)y)} dx\, dy.$$

The integral in $[\cdot]$ leads to signal loss due to through-plane dephasing, whereas the exponential factor with $\overline{\Delta B_0}(x,y)$ causes phase error during readout. Assuming a centered rectangular slice profile with thickness Δz, the signal loss factor, calculated at $t = 0$ when the k-space center is sampled, is given by

$$
l(x,y,0) \quad = \quad \int_{z_0 - \frac{\Delta z}{2}}^{z_0 + \frac{\Delta z}{2}} e^{\imath \gamma g_z(x,y)(z-z_0)(0+T_E)} dz
$$

$$(1.8) \qquad\qquad = \quad \mathrm{sinc}\left(\frac{\gamma \Delta z g_z(x,y) T_E}{2} \right).$$

Equation (1.8) tells us that image intensity at location (x,y) falls off as a sinc function of the product of slice thickness, through-plane gradient, and echo time. It is intuitive indeed – signal loss worsens when dephasing becomes fast (through-plane gradient increases), when dephasing time increases (echo time lengthens), or when more dephased spins are summed to form a voxel (slice thickness increases).

1.4 Current solutions to signal loss

1.4.1 Optimization of slice selection

Signal loss due to intravoxel dephasing can be mitigated by reduction of the size of brain image voxels [19–22]. In particular, loss caused by through-plane dephasing can be alleviated by usage of relatively thin slices [23], as reflected in Eq. 1.8. If the through-plane magnetization contributing to each slice is reduced, cancellation of dephased spin signals is alleviated. One major drawback of using thin slices is, obviously, a reduction in brain coverage per scan time [24]. For the same brain coverage, the number of thin slices has to be increased by multiple folds compared to when regular thick slices are prescribed. Another problem with using thin slices is a reduction in signal-to-noise ratio (SNR) in the functional images.

Some studies also suggested that certain oblique slice orientation can mitigate the signal loss problem [22, 25, 26]. With oblique slices, dephased magnetization is "redistributed" into tilted voxel volumes. It was suggested that particular orientations of slices would distribute magnetization such that phase cancellation would be minimized. However, this strategy can only partially recover BMS-induced signal loss, and the optimal slice orientation may vary from subject to subject because of structural difference, and from session to session because of shim value difference. The strategy also interferes with brain coverage preferences that are specific to the functional study.

1.4.2 Optimization of data acquisition

The fast data acquisition methods (EPI and spiral imaging) can be optimized so that signal loss is reduced. For EPI, Ref. [22] suggested that frequency-encoding should be along the direction in which the field gradient is dominant, and Ref. [27] reported that the direction of phase-encoding also significantly affects signal loss. For spiral imaging,

studies found that the "spiral in-out" trajectory [28] is better than "spiral-out" in terms of loss mitigation, and "spiral in-in" is even better than "spiral in-out" [29]. Generally, these acquisition optimization strategies only partially recover the signal loss.

1.4.3 Gradient compensation

One category of methods use z-gradient lobes, in various ways, to compensate for the BMS-induced through-plane dephasing [24, 30–35]. A z-gradient lobe, deployed after excitation, can create linear phase distribution along the z dimension that cancels out the dephasing accumulated up to data acquisition. However, gradient lobes are non-selective in the in-plane dimensions, thus the same amount of through-plane phase is created over the entire image. Because BMS-induced field gradient ($g_z(x, y)$ in Eq. 1.8) varies as a function of in-plane location, one needs to acquire multiple subimages using different lobe sizes to refocus different image regions. The subimages can be combined, in various ways [36, 37], to form a final image free of signal loss. For acceptable signal recovery, these methods generally require several subscans for each slice location, and hence a major problem of these methods is temporal resolution loss in the functional study, due to acquisition of multiple subimages for each slice location. Recently researchers proposed that the temporal resolution loss can be mitigated if subimage acquisition is applied to only a small set of slice locations [38].

1.4.4 Localized shimming

Another class of approaches to signal recovery aim directly at counteracting the BMS-induced field distortion. It can be achieved by placement of materials or coils close to the sites of field inhomogeneity. Wilson et al. [39] proposed placement of a "passive" shim (made of pyrolytic graphite) in the roof of the mouth to improve field homogeneity at the inferior frontal cortex. On the same principle, Hsu et al. [40] reported an "active" shim-

ming method, using intraoral shim coils with electrical currents adjustable on a patient-by-patient basis. To avoid intravoxel coil placement, Wong et al. [41] proposed using an external coil for active shimming.

These shimming methods were shown to be effective, to certain extents, in improving field homogeneity and therefore reducing signal loss and improving functional sensitivity [40,42]. However, for long fMRI sessions, placement of shimming hardware on subject leads to significant discomfort, which will likely increase head motion. Also, for intraoral methods, motion of the mouth or tongue can displace the shimming device so that calibration becomes inaccurate. These factors will potentially make functional images much less robust to motion. In addition, intraoral shimming is potentially hazardous to children and psychiatric patients, because of the risk of choking.

1.4.5 Excitation precompensation

Through-plane dephasing, the culprit of signal loss, can be viewed as taking place *between* RF excitation and data acquisition. It is conceivable that dephasing can be "*precompensated*" in the excitation stage, such that spins are in phase during readout, or more precisely, at the echo time. This idea was initially proposed by Cho et al. [43], who showed that pulses that excite slices with quadratic through-plane phase profiles can partially recover signal loss. However, because those RF pulses are non-selective in the plane, through-plane quadratic phase is created everywhere in the image plane. As a result, recovery in one in-plane region is coupled with signal reduction or even loss in the others, where through-plane phase may originally be coherent. Several years later, Chen et al. [44] and Glover et al. [45] proposed that one can first acquire a map of the inhomogeneous field ("field map") of the slice volume, and then design precompensatory RF pulse "tailored" to that field map. Their one-dimensional (1D) tailored RF pulse methods still suffer from

the lack of in-plane selectivity.

1.5 Three-dimensional tailored RF pulses

1.5.1 Basics

The 1D precompensation methods inspired the work of Stenger et al. [46], which demonstrated simultaneous slice selection *and* various through-plane phase precompensation at different in-plane locations. Those sophisticated *three-dimensional tailored RF* (3DTRF) pulses were designed based on the *excitation k-space* [47] perspective, under small-tip-angle approximation to the Bloch equation. To test recovering signals above the sagital sinus while preserving SNR at the remaining regions, Stenger et al. defined the desired magnetization pattern by a main disk that selected the slice volume, with a small disk subtracted from the main disk at the site of signal loss. An identical disk with through-plane linear phase was inserted in its place.

In the pulse design process, the stack-of-spirals trajectory [48] was used to cover a cylindrical volume in 3D excitation k-space (Fig. 1.3). It "frequency-encodes" the in-plane k dimensions with 2D spirals, and "phase-encodes" in the slice-select k direction with discrete sampling, implemented by gradient blips (Fig. 1.4). The RF waveform accompanying that trajectory is designed analytically, from the Fourier transformation of the desired pattern that comprises Bessel and Gaussian functions. The pulse was deployed in lieu of the sinc pulse in a GRE sequence with long echo time. It was demonstrated that a 60-ms 3DTRF pulse was effective in selecting a 2-cm-thick slice, and recovering signal loss above the sinus cavity (Fig. 1.5).

1.5.2 Pros and cons

Stenger et al.'s demonstration was exciting as a proof of the 3DTRF concept. However, to implement 3DTRF pulses into routine fMRI studies, there are major technical hurdles
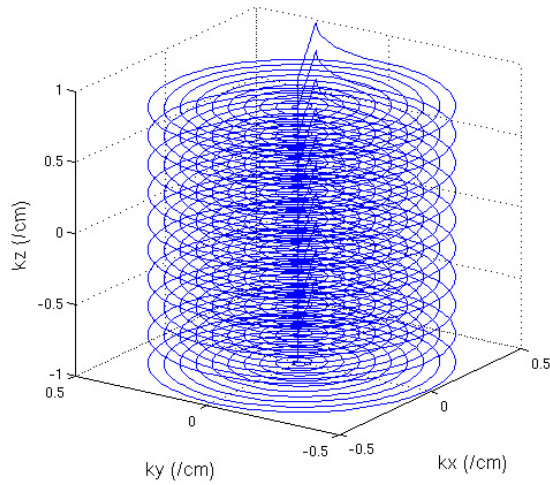
Figure 1.3: The stack-of-spirals trajectory, covering a cylindrical volume in excitation k-space, was used in the original 3DTRF method. (Note: this trajectory example does not correspond to the waveforms in Fig. 1.4.)
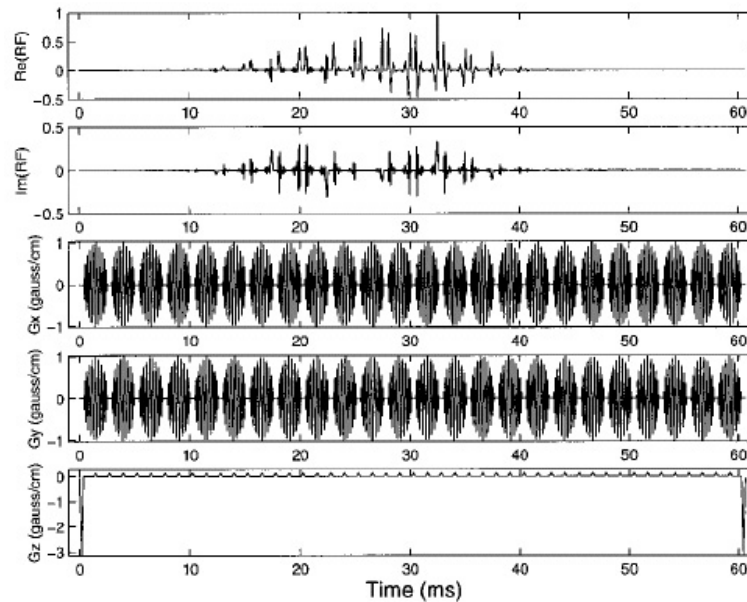
Figure 1.4: 60-ms RF and gradient (G_x, G_y, G_z) waveforms in the original 3DTRF method by Stenger et al., for a 2-cm slice with "excitation sidelobes" 10 cm apart. The pulse needs to be lengthened by multiple folds for thinner slices and sidelobes outside of the head. (Adopted from Ref. [46], Copyright 2000, reprinted with permission of Wiley-Liss Inc., a subsidiary of John Wiley & Sons, Inc.)

to overcome. First, the 3DTRF pulses were exceedingly long relative to slice-selective sinc pulses. In their demonstration, the pulse was more than eighteen fold as long as a
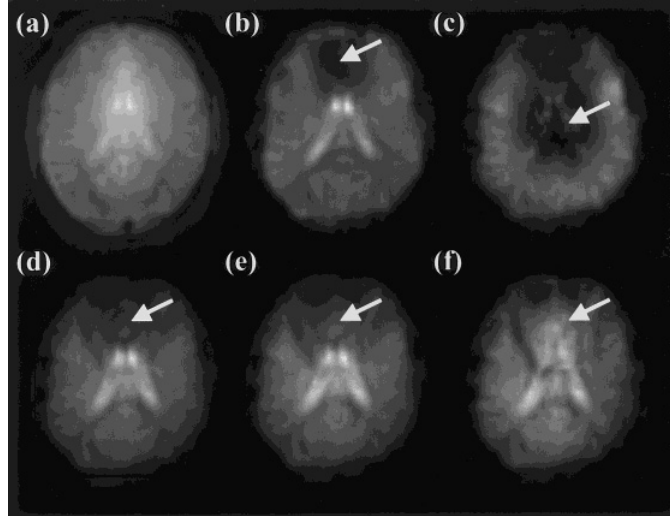
Figure 1.5: Brain images acquired with a sinc pulse with (a) 5-ms T_E and (b) 32-ms T_E (2-cm-thick slice). Arrow indicates region of signal loss above the sinus cavity. Images in (c)-(f) were taken with the same parameters as in (b), but with 3DTRF pulses instead of sinc pulse. (c): Through-plane phase pre-compensation was wrongly placed at center of brain, leading to wider signal loss (arrow). (d): After the pre-compensation region was moved to the anterior brain, signals were partially recovered (arrow). (e)-(f): Through-plane phase variation was increased (by factors of 2 and 3) compared to in (d), providing even better recovery (arrow). (Adopted from Ref. [46], Copyright 2000, reprinted with permission of Wiley-Liss Inc., a subsidiary of John Wiley & Sons, Inc.)

typical 3.2-ms sinc pulse. Note that it was selective for a fairly thick 2-cm Gaussian slice. In order to select slices finer than 2 cm (say, 5 mm in typical fMRI studies) or with sharper transitions, a wider range of k_z must be traversed, and thus the 3DTRF pulse will be much longer than 60 ms. Such lengthy RF pulses severely hamper the temporal resolution of the MR images, which is critical in an fMRI study.

In addition, because the long 3DTRF pulses are deployed in regions with highly inhomogeneous field, excitation accuracy can be severely affected by resonance frequency offsets. Particularly, because of phase-encoding in the slice-select direction, the slice profile can be significantly distorted. There may also be spatially variant slice shifting, leading to "potato-chip-shaped" slice volumes. Such slice distortions are troubling in fMRI, because of potential erroneous mapping between functional and anatomical brain images.

Despite shortcomings in its initial implementation, the 3DTRF method clearly deserves

further development for full realization of its potential. The method has several important advantages. First, it does not interfere with imaging parameters such as voxel size or slice orientation, which are typically set based on the imaging study context. Second, unlike most of the gradient compensation methods, it does not require multiple subimage acquisitions for a single image. Multiple-fold temporal resolution loss is therefore avoided. The method also obviates placement and calibration of localized shimming hardware. Finally, it can in fact be applied in conjunction with many of the exisiting methods for maximal signal recovery. For example, the 3DTRF method can be applied in concert with the localized shimming techniques. It can possibly provide the intricate corrections that gross localized shimming fails to accomplish.

1.6 Project goals

In this context, there are three major goals in the current research project:

1.6.1 Advancing the 3DTRF method

The specific aims of advancing the 3DTRF method are as follows:

Aim 1: Reduce the length of 3DTRF pulses to minimize impact on fMRI temporal resolution. For the 3DTRF method to be valuable, it has to be less costly, in terms of temporal resolution, than standard methods such as slice thinning [23] and z-shimming [24].

Aim 2: Improve excitation accuracy of 3DTRF pulses. Accuracy of slice selection is critical for functional brain mapping, and thus needs to be safeguarded. Desirably, the pulses should also be accurate in in-plane placement of through-plane phase. It assures effective recovery at loss regions and SNR preservation at unaffected regions.

Aim 3: Assure that computation of 3DTRF pulses is fast enough so that it is feasible to compute the pulses *online* (with subject lying inside the scanner).

Aim 4: Improve the robustness of the method, so that it is not overly sensitive to errors in input measurements (for example, map of frequency offsets, or "field map") and changes in design parameters.

1.6.2 Exploring an alternative RF pulse design

Besides the 3DTRF method, we are interested in exploring an alternative approach of using RF pulses for signal recovery. The new pulse design also aims to create precompensatory phase variations using selective excitation. However, instead of 3D spatially selective excitation as with 3DTRF pulses, 2D spectral-spatial selective excitation can potentially be used to achieve this goal. The idea is that precompensatory through-plane phase variations can be prescribed *not* based on where off resonance occurs spatially (probed by field maps), but instead, based on the "spectral signature that through-plane dephasing carries" (see Chapter 6). Such spectral-spatial pulse design does not rely on the pixel-to-pixel offset values in its computation. Consequently, the pulses can be computed offline *prior to* the fMRI experiment. A collection of spectral-spatial pulses can be precomputed and stored. Based on field maps currently acquired or from training data, a subset of the pulses can be deployed at different slice locations. This strategy saves the heavy pulse computation that has to be carried out online in the 3DTRF case. On the other hand, because the spectral-spatial pulses are selective in only two dimensions, they are potentially shorter, easier to compute, and hence more robust.

1.6.3 Developing new pulse design techniques

New RF pulse design techniques will be introduced for the development of the signal recovery methods. Many of the new techniques will not be specific to the signal recovery problem, and will enrich the general pulse design repertoire. In particular, techniques for single-coil excitation can be generalized to parallel excitation with multiple transmit coils.

CHAPTER 2

Fourier interpretations of selective excitation

Before we dwell on RF pulse design methods for signal recovery, let us review some fundamental theories about the MR excitation process and RF pulse design.

For magnetic spins to produce MR signals detectable by receiver coils, they have to be first *excited*. In classical physics terminology, MR *excitation* can be viewed as applying a RF magnetic field (b_1) in the transverse direction relative to a static main field (B_0), so that magnetization (average) rotates away from the main field axis to produce some detectable transverse magnetization components. In the most basic case of *non-selective excitation*, b_1 is tuned to the Larmor frequency of magnetization in the presence of only B_0, so that it excites magnetization in the entire volume sensitive to the excitation coil, without spatial or spectral (resonance frequency) selectivity.

If appropriate magnetic field gradients (g_x, g_y, g_z) are turned on during application of b_1, magnetization excitation can be restricted to a specific volume within the sample. Such *spatially selective excitation* is extremely important in all branches of MRI, because it can be used for slice selection, in which excitation provides one level of spatial localization, thereby reducing the imaging task to a 2D one. In this case, only the gradient in the slice-select direction (g_z) is turned on to give 1D selectivity. If multiple gradients are applied together with the RF field, the spatial selectivity can be multi-dimensional. When a spatial

excitation pulse is applied repeatedly over time (with the right frequency), it can also possess spectral selectivity – now the excitation pattern depends on not only the chemical species' spatial location, but its resonance frequency as well. This technique is called *spectral-spatial selective excitation* [49].

This chapter is not meant to be a comprehensive review of selective excitation and RF pulse design. Instead, I am going to focus on some special cases in which the Fourier Transformation can be applied to describe the relationship between RF pulse and its resulting excitation pattern. I will start with the Bloch equation [50] that governs MR excitation. It turns out that a small-tip-angle approximation to the Bloch equation can lead to a Fourier interpretation of spatially selective excitation. The interpretation is generalizable to multiple spatial dimensions. Surprisingly, for large-tip-angle excitation in which the approximation is no longer valid, a similar Fourier interpretation holds accurate for the tip angle, provided that certain symmetry conditions are satisfied. Next I will extend the results to pulses that are selective both spectrally and spatially. Finally I will generalize small-tip-angle excitation to parallel excitation with multiple transmit coils, which is currently an area of active research. These Fourier interpretations of selective excitation form the backbones of the RF pulse designs that we will explore in the following chapters.

2.1   The Bloch equation

The fundamental equation governing MR excitation is the Bloch equation postulated by F. Bloch in 1946 [50]. Let $\mathbf{m}(\mathbf{x}) \in \mathbb{R}^3$ be the average magnetization at spatial location $\mathbf{x}$. Bloch equation states that if we ignore the effects of field inhomogeneity and spin relaxations, the dynamics of $\mathbf{m}(\mathbf{x})$ in the *rotating frame*, which rotates at the Larmor

frequency of proton, is governed by

$$
(2.1) \qquad \frac{d\mathbf{m}(\mathbf{x})}{dt} \;=\; \gamma \begin{pmatrix} 0 & \mathbf{g}(t)\cdot\mathbf{x} & -b_{1,y}(t) \\ -\mathbf{g}(t)\cdot\mathbf{x} & 0 & b_{1,x}(t) \\ b_{1,y}(t) & -b_{1,x}(t) & 0 \end{pmatrix} \mathbf{m},
$$

where γ denotes the gyromagnetic ratio, $b_1(t) = b_{1,x}(t) + \imath b_{1,y}(t)$ denotes the complex-valued RF pulse (comprises both magnitude and phase) and $\mathbf{g}(t) = (g_x(t), g_y(t), g_z(t))^T$ denotes the applied gradients, both as functions of time (t). For the case of an initially fully relaxed magnetization aligned with the main field ($+z$ axis), $\mathbf{m}(0) = (0, 0, M_0)^T$, where M_0 denotes the equilibrium magnetization magnitude.

To selectively excite magnetization for a specific MR application, one has to design the continuous-time waveforms of $b_1(t)$ and $\mathbf{g}(t), t \in [0, T]$ where T is the end time of pulse, such that the resulting magnetization pattern at T, $\mathbf{m}(\mathbf{x}, T)$, is as close to the *desired* excitation pattern, $\mathbf{m}_{des}(\mathbf{x})$, as possible. This is the so-called *RF pulse design* problem in the MR literature (although the problem also involves designing the appropriate gradient waveforms). From a "non-linear systems" point of view, we can regard $\mathbf{u}(t) = (b_1(t), \mathbf{g}(t))^T$ as the *input* and $\mathbf{m}(\mathbf{x}, t)$, as the *state* of the nonlinear system, f, characterized by the Bloch equation (2.1):

$$
(2.2) \qquad \dot{\mathbf{m}}(\mathbf{x}, t) = f(\mathbf{m}(\mathbf{x}, t), \mathbf{u}(t)), \qquad t \in [0, T].
$$

We want to design the input to "drive" system (2.2) so that $\mathbf{m}(\mathbf{x}, T) \approx \mathbf{m}_{des}(\mathbf{x})$. This non-linear problem is generally difficult to solve, but fortunately for most cases of interest there are simple, easily computable solutions based on assumptions and approximations.

2.2 Small-tip-angle selective excitation

The data acquisition and image reconstruction processes in MRI have been facilitated by the viewpoint of spatial frequency, or k, space data sampling [51–53]. Surpris-

ingly, selective excitation can also be analyzed with an analogous *excitation k-space* concept [47], under the small-tip-angle approximation [54, 55] to the Bloch equation. Let $m_{xy}(\mathbf{x}) = m_{xy}(\mathbf{x}, T)$ be the transverse magnetization in the rotating frame, which can uniquely specify magnetization in the small-tip-angle regime of 0-90 degrees. Under the assumptions that

1. magnetization is initially aligned with main field B_0;

2. flip angles by the RF pulse are small,

$m_{xy}(\mathbf{x})$ can be quite accurately approximated by

$$(2.3) \qquad m_{xy}(\mathbf{x}) \approx \imath\gamma M_0 \int_0^T b_1(t) e^{\imath\mathbf{k}(t)\cdot\mathbf{x}} dt,$$

where $\mathbf{k}(t)$ is a spatial frequency vector variable given by the integral of the remaining gradient areas:

$$(2.4) \qquad \mathbf{k}(t) = -\gamma \int_t^T \mathbf{g}(\tau) d\tau.$$

Hence, the transverse magnetization pattern is the Fourier transform of the "RF deposition" along a k-space trajectory determined by the gradient waveforms. Equation (2.3) can be rewritten to expose the direct Fourier relationship between the spatial domain and an "excitation k-space":

$$(2.5) \qquad m_{xy}(\mathbf{x}) \approx i\gamma M_0 \int_\mathbf{K} p(\mathbf{k}) e^{i\mathbf{k}(t)\cdot\mathbf{x}} d\mathbf{k}$$

where $p(\mathbf{k})$ denotes a weighted k-space trajectory:

$$(2.6) \qquad p(\mathbf{k}) = \int_0^T \frac{b_1(t)}{\gamma|\mathbf{g}(t)|} [\delta(\mathbf{k} - \mathbf{k}(t))|\dot{\mathbf{k}}(t)|] dt.$$

Figure 2.1 illustrates how the k-space concept is applied to analyze 2D spatially selective excitation. Backward integration (Eq. 2.4) of the gradient waveforms in (a) traces out
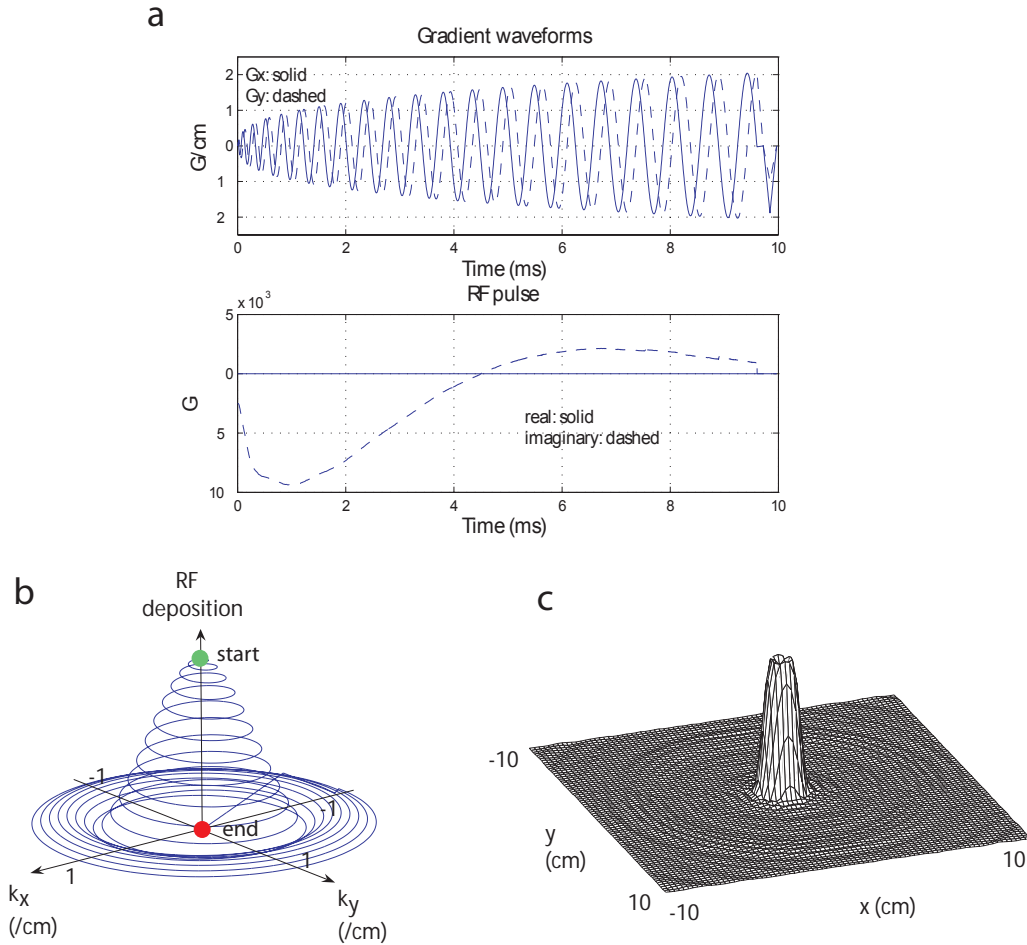
Figure 2.1: Illustration of k-space analysis of spatially selective excitation. a: gradient waveforms that constitute a 2D "spiral-out" k-space trajectory, and the complex RF pulse designed to excite a small disc at the center of space. b: These waveforms form an outward spiral in excitation k-space, depositing energy along its way. c: Bloch simulated excitation pattern. It can be very accurately approximated by the Fourier transform of the deposition in k-space.

a trajectory in excitation k-space that spirals outward from the origin to the high-spatial-frequency regions, and finally traverse back to the origin (b). The complex RF pulse shown in (a), after correction of sampling density, can be interpreted as complex "RF deposition" along the trajectory. If we numerically simulate the Bloch equation (Eq. 2.1) over a 2D spatial grid with the waveforms as input, we can obtain the resulting excitation pattern as shown in (c). This pattern can be accurately predicted by the Fourier transform of the

deposition in k-space. Note that this particular deposition pattern is discrete in the radial direction although it is continuous along the spiral. As a result, aliasing excitation takes place outside the circular "excitation FOV" (XFOV) of diameter 20 cm. Finite range of k-space sampling also leads to excitation ripples in the radial direction.

This powerful k-space analysis greatly simplifies RF pulse design in the small-tip-angle regime. It turns pulse design into the problem of choosing the appropriate gradient waveforms so that excitation k-space is adequately traversed by the trajectory, and calculating the corresponding RF deposition along the trajectory, so that the Fourier transform of the deposition pattern in excitation k-space is close to the desired excitation pattern. The well developed theories concerning Fourier transformation (e.g., [56]) can now be readily adopted in the design and analysis of RF pulses. It leads to both simplicity and sophistication that we would not have if we design pulses directly via the non-linear Bloch equation (Eq. 2.1).

2.3   Large-tip-angle selective excitation

The small-tip-angle solution assumes both the effect of the RF pulse is small and the initial magnetization is along $+z$ axis. If we abandon the initial magnetization assumption and only assume that the RF amplitude is small, a so-called *small-excitation* solution can be derived in the spinor domain [57]. The small-excitation solution, though expressed for the Cayley-Klein parameters in the spinor domain, is convenient since the solution's major constituent is still a Fourier integral of the RF-weighted k-space trajectory (same k-space definition). In the special case of *inherently refocused pulses* which

1. carry Hermitian symmetric weights in k-space, and

2. start at the k-space origin ($\mathbf{k}(0) = \mathbf{0}$),

the small-excitation solution leads to a Fourier-integral solution for rotation angle, ϕ:

$$(2.7) \qquad \phi(\mathbf{x}) \quad \approx \quad \gamma \int_0^T b_1(t) e^{i\mathbf{k}(t)\cdot\mathbf{x}} dt.$$

This result is important, because now if we have an excitation pulse that may be broken into a sequence of small-excitation inherently refocused subpulses with the same rotation axis, then the aggregate tip angle (ϕ_{total}) resulting from concatenating the subpulses is simply the sum of the individual tip angles [57]:

$$(2.8) \qquad \phi_{total}(\mathbf{x}) \quad \approx \quad \gamma \int_0^{T_{total}} b_1(t) e^{i\mathbf{k}(t)\cdot\mathbf{x}} dt.$$

This equation tells that the pulse creates total tip angle pattern approximately equals the Fourier transform of the RF-weighted k-space trajectory, and it holds for arbitrarily large tip angles. Note that this approximation is accurate only if the trajectory can be (approximately) decomposed into inherently-refocused component trajectories. This category of trajectories include the spiral and projection-reconstruction trajectories, but not, for example, the echo-planar trajectory.

All of the pulse designs in this project are restricted to the small-tip-angle regime. Therefore, Eq. 2.3 will be the fundamental equation that we work with. In fact, the small-tip-angle analysis works fairly well for flip angles up to 90 degrees [46]. Still, the large-tip-angle result is noteworthy, because it shows that small-tip-angle pulse design techniques are transferable to large-tip-angle cases.

2.4 Incorporating resonance frequency offsets

The excitation k-space equation (Eq. 2.3) has to be modified when significant off resonance is present within the sample. In practice, protons within the sample resonate at frequencies slightly deviated from the expected value. The primary cause of off resonance is that the main field within an MRI scanner is inhomogeneous, because of imperfect

hardware and magnetic susceptibility induced field variations within the sample. Also, resonance frequency shifts depending on the chemical environment in which the proton resides (often called "chemical shifts").

If one incorporates a spatial map of resonance frequency offsets ($\Delta\omega(\mathbf{x})$) in the Bloch equation, Eq. 2.1 becomes

$$(2.9) \quad \frac{d\mathbf{m}(\mathbf{x})}{dt} = \gamma \begin{pmatrix} 0 & \mathbf{g}(t) \cdot \mathbf{x} + \Delta\omega(\mathbf{x}) & -b_{1,y}(t) \\ -\mathbf{g}(t) \cdot \mathbf{x} - \Delta\omega(\mathbf{x}) & 0 & b_{1,x}(t) \\ b_{1,y}(t) & -b_{1,x}(t) & 0 \end{pmatrix} \mathbf{m}.$$

Through the small-tip-angle analysis [47], the offsets result in an extra factor inside the excitation k-space integral [58, 59]:

$$(2.10) \quad m_{xy}(\mathbf{x}) \approx \imath\gamma M_0 \int_0^T b_1(t) e^{\imath \mathbf{k}(t) \cdot \mathbf{x} + \imath \Delta\omega(\mathbf{x})(t-T)} dt.$$

This equation is comparable to the off-resonance-incorporated MR signal equation (Eq. 1.4). Inclusion of the frequency offsets "ruins" the Fourier relationship between the excitation pattern and k-space, in the sense that Eq. 2.10 is no longer a Fourier integral. This fact has computational ramifications for pulse design problems, which I will discuss in details in Chapter 4.

2.5 Extensions

2.5.1 Spectral-spatial selective excitation

The excitation k-space perspective of small-tip-angle selective excitation can be extended for analyzing and designing another class of pulses called *spectral-spatial* (SPSP) *pulses* [49]. In the previous section, resonance frequency offsets are regarded as a function of space ($\mathbf{x}$), which results in an additional exponential factor to the Fourier integral (Eq. 2.10). Now if we view resonance frequency offsets as a general variable, f (in Hertz), instead of a spatial function, Eq. 2.10 becomes
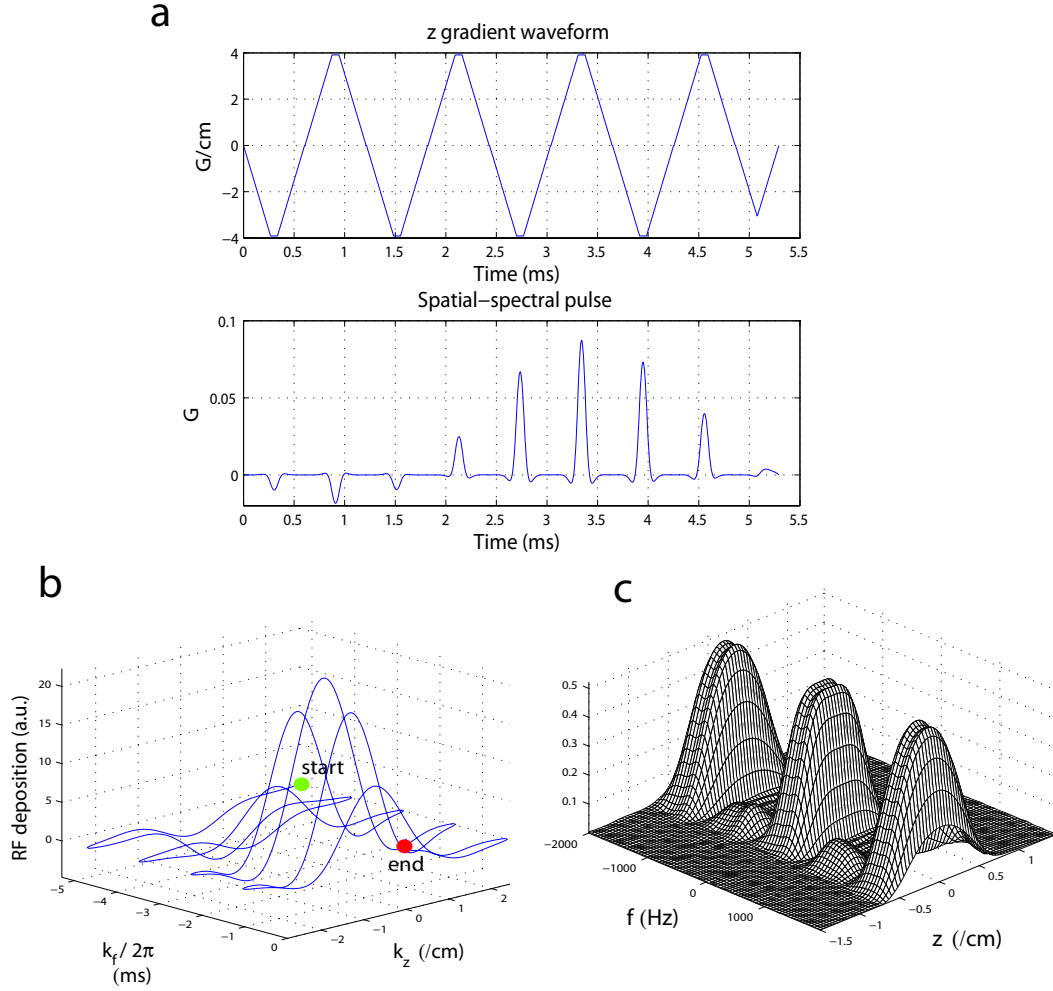
Figure 2.2: Illustration of k-space analysis of SPSP selective excitation. a: z gradient and RF waveforms of a 2D fat-suppressing slice-select SPSP pulse. b: As time elapses, a zigzag trajectory is traced out in the joint SPSP k-space. The RF pulse, after sampling density correction, deposites energy along its way. c: Bloch simulated SPSP excitation pattern. It can be accurately approximated by the Fourier transform of the k-space deposition.

$$(2.11) \qquad m_{xy}(\mathbf{x}, f) \quad \approx \quad \imath \gamma M_0 \int_0^T b_1(t) e^{\imath \mathbf{k}(t) \cdot \mathbf{x} + \imath 2\pi f \cdot (t-T)} dt.$$

If we define *joint SPSP k-space* variable $\mathbf{k}_{spsp}(t) = (\mathbf{k}(t), k_f(t))^T$ where $k_f(t) = 2\pi(t - T)$, and joint SPSP variable $\mathbf{r} = (\mathbf{x}, f)^T$, we have

$$(2.12) \qquad m_{xy}(\mathbf{r}) \quad \approx \quad \imath \gamma M_0 \int_0^T b_1(t) e^{\imath \mathbf{k}_{spsp}(t) \cdot \mathbf{r}} dt.$$

This equation implies that by weighting the trajectory in the joint SPSP k-space with the RF pulse, we can achieve excitation selectivity in both space *and* the spectral dimension – The resulting magnetization pattern, as function of space and frequency, approximately equals the Fourier transform of the weighted trajectory in the joint SPSP k-space. It is interesting that while traversal in the (k_x, k_y, k_z) subspace is determined by the gradient waveforms (Eq. 2.4), traversal along k_f is accomplished by simply letting time elapse.

Most SPSP pulses used in current MR applications are selective in the slice-select and spectral dimensions (hence "2D" SPSP pulses). Those pulses can be used to excite a slice of magnetization from one chemical species (e.g., water) while leaving magnetization of others (e.g., fat) virtually unaffected. Figure 2.2 illustrates how the joint k-space concept is applied to analyze an SPSP pulse that selects a slice of water while suppressing fat, which resonates at -420 Hz relative to water at 3 Tesla. Backward integration of the oscillating z gradient waveform in (a), and a constant progression of time (hence k_f), trace out a zigzag trajectory in the joint SPSP k-space (b), which eventually ends at the origin. The SPSP pulse, formed via cascading windowed sinc pulses and modulating them with a Shinnar-La-Roux (SLR) spectral envelope, deposits energy along the trajectory. If we numerically simulate the Bloch equation at different locations (z) and frequency offsets (f) with the waveforms as input, we obtain the resulting SPSP excitation pattern (c). It can be accurately predicted by the Fourier transform of the k-space deposition in (b). In this example, the (non-uniform) discrete sampling in k_f leads to (non-identical) periodic peaks in f, and the windowed sinc weighting along k_z provides the slice profile. Here a slice of water ($f = 0$ Hz) is excited by the main peak while fat ($f = -420$ Hz) is suppressed by the first null.

Besides fat suppression, SPSP pulses can be applied to, for example, suppression of water signals in spectroscopy or spectroscopic imaging [60]. Elaborate discussions of

2D SPSP pulse design techniques can be found in Refs. [61–63]. SPSP pulses that are selective in two spatial and one spectral dimensions have also been proposed by Morrell et al. [64]. However, those pulses are perhaps too long to be practical. To date, there has not been any reports on designs and applications of SPSP pulses that are selective in all spatial and spectral dimensions, perhaps due to prohibitive pulse length requirement.

In Chapter 6, we will postulate a novel SPSP pulse design for signal recovery. The joint SPSP k-space concept will be the fundamental workhorse behind the design.

2.5.2 Parallel excitation with multiple RF coils

So far we have focused on selective excitation using a single transmit coil with uniform transmit sensitivity pattern. The RF pulse played out with the coil is felt equally throughout the sample without regard to spatial location. In recent years, researchers have proposed *parallel excitation* with multiple transmit coils driven with independent waveforms [65, 66]. Each coil has a unique non-uniform sensitivity pattern over space, and magnetization is excited by the aggregate RF field from all the coils. In the linear small-tip-angle regime, the aggregate excitation pattern approximately equals superposition of the excitation patterns by individual coils:

$$(2.13) \qquad m_{xy}(\mathbf{x}, T) \quad \approx \quad i\gamma M_0 \sum_{r=1}^{R} s_r(\mathbf{x}) \int_0^T b_r(t) e^{i\mathbf{k}(t)\cdot\mathbf{x} + i\Delta\omega(\mathbf{x})(t-T)} dt.$$

where $b_r(t)$ represents the RF pulse for the rth coil, and $s_r(\mathbf{x})$ is its complex-valued sensitivity pattern, $r = 1, \ldots, R$. Note that superposition of individual coils' excitation patterns generally does not hold true at large tip angles, because of Bloch equation non-linearity.

Equation 2.13 is an analogue to the MR signal equation in parallel imaging (e.g., [67–69]). As parallel imaging shortens data readout, parallel excitation shortens multi-dimensional spatial pulses by multiple folds, because of simultaneous transmission and the extra "encoding" by the sensitivity patterns. Many multi-dimensional selective excita-

tion applications, which were impractical because of inhibitive pulse length requirements, now appear feasible using parallel excitation. Examples include 3DTRF pulses for B_1 inhomogeneity compensation [70, 71], and B_0 inhomogeneity compensation [46], which is the central topic of this research project. Many of the proposed pulse design methods in this thesis can be generalized to parallel excitation.

2.6 Conventional pulse design methods

Recall that the RF pulse design problem involves designing $b_1(t)$ and $\mathbf{g}(t)$ such that at pulse end, the resulting magnetization pattern is close to a certain desired pattern. With the Fourier interpretations of selection excitation that we have discussed, pulse design is significantly simplified and accelerated, because the inverse problem no longer involves the non-linear Bloch equation. In this section I will review conventional methods of designing spatial and SPSP pulses.

2.6.1 Designing spatial pulses

Let us first consider designing a spatially selective pulse transmitted with a single coil (with uniform sensitivity pattern). The problem starts with specification of the desired pattern, $d(\mathbf{x})$. Based on that pattern, the k-space trajectory is first determined. It should sample k-space dense enough so that aliasing does not take place within the field of view (FOV), and the sampling range should be large enough so that the desired excitation resolution is rendered. Next, the Fourier transform of the desired pattern is sampled along the trajectory, followed by multiplication with weighting functions:

$$(2.14) \qquad b_1(t) \quad \propto \quad \Delta(\mathbf{k}(t))|\mathbf{g}(t)| \left\{ \int_{XFOV} d(\mathbf{x}) e^{i\mathbf{k}(t) \cdot \mathbf{x}} d\mathbf{x} \right\},$$

where $\Delta(\mathbf{k}(t))$ is the inverse sampling density [72, 73], and $|\mathbf{g}(t)|$ compensates for the "velocity" with which the trajectory traverses k-space. Finally $b_1(t)$ is normalized and

scaled to provide the desired tip angles. Examples of this design approach can be found in, for example, Refs. [46, 74, 75].

If frequency offsets are incorporated into the Fourier integral (Eq. 2.10), the Fourier relationship is ruined and hence this approach of sampling the desired pattern's transform is no longer useful. Researchers proposed using the non-Fourier *conjugate-phase* (CP) method from image reconstruction [15, 76], which accounts for off resonance and thus can correct for it to some extent [58, 59]. I will reserve the mathematical details of CP for the following chapter. It is noteworthy here that the Fourier relationship can still be exploited to accelerate CP, after certain approximations are made. Those acceleration methods will be discussed in Chapter 4.

In the case of parallel excitation with multiple coils, each coil excites a different pattern. Superposition of the subpatterns, modulated by their individual sensitivity patterns, gives the final resulting pattern that resembles the desired one. Therefore, the transform of the aggregate desired pattern has to be first decomposed into the transforms of the patterns for individual coils. This decomposition problem can be tackled with direct matrix inversion or iterative methods. Subsequently, the RF waveforms for each coil can be derived as in the single-coil case. This parallel excitation design approach was postulated in the original "Transmit SENSE" paper by Katscher et al. [65]. Another design method, specifically for parallel excitation with EP trajectories, was also introduced by Zhu et al. [66].

2.6.2 Designing spectral-spatial pulses

The design of an SPSP pulse starts with specification of desired spectral and spatial profile characteristics. Based on the specified spectral main peak and null positions, one first selects the oscillating gradient waveform, which determines the trajectory in the joint SPSP k-space. That waveform dictates how long one spatial subpulse is. Next, the spatial

subpulse shape is designed according to the slice profile specifications (thickness, transition bandwidth, etc), followed by design of the spectral envelope that determines the shape of the spectral peaks (for example, how wide the peaks are). Finally, the SPSP pulse is synthesized by concatenating the spatial subpulses and modulating their amplitudes with the spectral envelope. Phase cycling techniques [61–63] can also be applied to shift or even suppress the spectral peaks. Readers should refer to Refs. [49, 61–63] for further details in SPSP pulse designs.

2.7 Conclusion

In this chapter, we have reviewed several special cases of selective excitation, for which the Fourier transformation can be applied to describe the relationship between RF pulse and its resulting excitation pattern. These Fourier interpretations are important because they greatly simplify the pulse design process. They also accelerate the pulse design, because now the Fast Fourier Transformation (FFT) can, somehow, be applied for the mapping between RF pulses and their excitation patterns. Fast design is critical particularly for applications in which pulses have to be computed online.

CHAPTER 3

Iterative RF pulse design

This chapter is based on materials from Ref. [77].

3.1   Why design RF pulses iteratively?

In the previous chapter, we have reviewed how the Fourier transformation can be applied to analyze selection excitation, and how it greatly facilitates RF pulse designs. Thanks to the Fourier interpretation, single-coil, small-tip-angle spatially selective pulses can be designed via determining an appropriate excitation k-space trajectory, sampling the Fourier transform of the desired pattern along the trajectory, and finally weighting the samples with sampling density compensation. When frequency offsets are incorporated, the conjugate phase (CP) method was proven to be effective.

In fact, these conventional pulse design approaches are non-ideal in several regards. First, in terms of minimizing excitation error, they generally produce pulses that are sub-optimal even with respect to just the linear design model. This design suboptimality is an eradicable source of excitation error, on top of the intractable amount due to the small-tip-angle approximation underlying excitation k-space. The excitation error due to design suboptimality is particularly large when the trajectory undersamples k-space, or when large off-resonance spatial gradients are present [58]. To compensate for the effects of off resonance gradients to some extent, Noll et al. [78] suggested a sophisticated density

compensation function (DCF) for CP reconstruction, but it is spatially variant and may not be readily extended to excitation. In fact, accurate DCF evaluation can generally be difficult and time consuming (see, for example, [79]). Erroneous DCF evaluation contributes significantly to excitation error.

Besides suboptimality, these approaches can handle neither the secondary objective of minimizing integrated RF power due to Specific Absorption Rate (SAR) considerations [80, 81], nor the hard constraint of peak RF power due to amplifier limitation [82]. Also, they are unable to exploit the possibility of assigning spatial weighting to excitation error. These issues suggest that there is room for improvement in the basic pulse design methodology, which would benefit current applications and possibly foster future ones.

The inverse-problem nature of pulse design suggests that an optimization approach can be beneficial. In fact, a range of optimization schemes have been used by researchers to design slice-selective 90-degree, inversion, and spin-echo pulses (for example, [80–85]). Those optimal pulses, designed with respect to the exact Bloch-equation system, achieved very accurate slice profiles. It is a natural extension to apply some of those schemes to the small-tip-angle design problem. Another inspiration for a better design method is the recent iterative image reconstruction algorithms [16, 86], which are also optimization schemes. Iterative reconstruction methods produce improved image quality relative to the CP and gridding methods [16, 86, 87]. The analogy between image reconstruction and pulse design [58] suggests that similar iterative optimization schemes can be applied to the latter.

In this context, we propose that single-coil, small-tip-angle spatial pulses can be designed via minimization of a quadratic cost function that consists of an excitation error term and regularization terms that control the integrated and peak RF power. The minimization problem can be solved iteratively via the conjugate gradient (CG) method [16].

Off resonance during excitation, particularly in the case of long pulses, has significant impact on the excitation accuracy [58, 59]. Thus, its effects are included in our design model. By Bloch simulation and scanner experiments, I will demonstrate the benefits of iterative designs over CP designs. Afterwards, I will investigate iterative spectral-spatial (SPSP) pulse design. Finally I will generalize the single-coil formulation to parallel excitation with multiple transmit coils, and point out that the advantages in the single-coil case are still applicable after generalization.

3.2 Formulation

Let us define complex function $m(\mathbf{x}; b) = m_{xy}(\mathbf{x}; b)$ as the transverse magnetization pattern resulting from the Bloch equation, with single-coil input RF pulse $b(t)$ and predetermined gradient waveforms $\mathbf{g}(t) = [g_x(t) \, g_y(t) \, g_z(t)]^T, t \in [0, T]$. As before, we assume that all magnetization is initially fully relaxed and aligned with $+z$ axis, and has equilibrium magnitude M_0. Now, an optimal small-tip-angle spatial pulse can be designed via minimizing a cost function that includes an excitation error measure, and a pulse energy term, which allows for a soft constraint on the integrated RF pulse power:

$$(3.1) \qquad b_{opt} \;\; = \;\; \arg\min_b \left\{ \int_{-\infty}^{\infty} |m(\mathbf{x}; b) - d(\mathbf{x})|^2 w(\mathbf{x}) d\mathbf{x} + \beta \int_0^T |b(t)|^2 dt \right\},$$

subject to the peak RF power hard constraint

$$(3.2) \qquad\qquad\qquad\qquad |b(t)|^2 \leq C \quad , \quad t \in [0, T].$$

In Eq. 3.1, complex function $d(\mathbf{x})$ is the desired magnetization pattern, real function $w(\mathbf{x})$ is a user-defined error weighting pattern that covers the FOV or any arbitrary region of interest (ROI), β is a regularization parameter that should be tuned based on SAR considerations, and C is a constant dependent on the RF amplifier peak power limitation. Note that for large-tip-angle pulse design, this minimization setup is also valid, except that

magnetization has to be represented by fields of 3D vectors instead of complex functions in order to avoid ambiguity. That problem was tackled in Refs. [80–82] for the 1D and constant-gradient case, but it was difficult and time-consuming due to Bloch equation non-linearity. Fortunately, under the small-tip-angle approximation, Fourier interpretation of the Bloch equation reduces Eq. 3.1 to a more easily solvable form.

Recall that a small-tip-angle excitation pattern approximately equals the Fourier transform of the RF-weighted trajectory (Eq. 2.3), and resonance frequency offsets ($\Delta\omega(\mathbf{x})$) can be incorporated by an extra exponential factor in the Fourier integral (Eq. 2.10):

$$(3.3) \qquad m(\mathbf{x}; b) \approx \imath\gamma M_0 \int_0^T b(t) e^{\imath\mathbf{k}(t)\cdot\mathbf{x} + \imath\Delta\omega(\mathbf{x})[t-T]} dt.$$

It seems natural to discretize Eq. 3.3 in time, since RF pulses are generally defined discretely in a pulse sequence before being processed by a Digital-to-Analog (D/A) converter and played out in the coil via RF circuitry. Let $b_j, j = 0, ..., N_t - 1$ be the pulse samples in the pulse sequence, and Δt be the sampling period. If the temporal point spread function[1] in the pulse physically played out is narrow, one can approximate Eq. 3.3 as

$$(3.4) \qquad m(\mathbf{x}; b) \approx \imath\gamma M_0 \sum_{j=0}^{N_t-1} b_j e^{\imath\mathbf{k}(t_j)\cdot\mathbf{x} + \imath\Delta\omega(\mathbf{x})[t_j-T]} \Delta t.$$

In space, we sample m at user-selected spatial locations $\{\mathbf{x}_i\}_{i=0}^{N_s-1}$. Now Eq. 3.4 can be expressed in matrix-vector multiplication form:

$$(3.5) \qquad \mathbf{m} \approx \mathbf{Ab}$$

where $\mathbf{m} = (m(\mathbf{x}_0; b), \ldots, m(\mathbf{x}_{N_s-1}; b))^T$, $\mathbf{b} = (b_0, \ldots, b_{N_t-1})^T$, and the elements of the $N_s \times N_t$ system matrix $\mathbf{A}$ are

$$(3.6) \qquad a_{i,j} = \imath\gamma M_0 e^{\imath\mathbf{k}(t_j)\cdot\mathbf{x}_i + \imath\Delta\omega(\mathbf{x}_i)[t_j-T]} \Delta t.$$

---

[1] The RF pulse being physically played out can be modeled as a pulse sample weighted "train of Dirac impulses", convolved with a time-invariant point spread function. The temporal spreading can arise from D/A converter characteristics and RF circuit impulse response functions. I ignore this spreading effect in the analysis here though it could be incorporated easily.

If $\mathbf{d}$ is a vector that contains spatial samples of the desired pattern, a CP pulse [15, 76] can be designed via

$$(3.7) \qquad\qquad \hat{\mathbf{b}}_{cp} \;=\; \mathbf{D}\mathbf{A}'\mathbf{d},$$

where $'$ denotes complex conjugate transpose, and $\mathbf{D}$ is a diagonal matrix containing samples of the DCF, $\{D(t_j)\}_{j=0}^{N_t-1}$, which approximately inverts $\mathbf{A}'\mathbf{A}$:

$$(3.8) \qquad\qquad \mathbf{D}\mathbf{A}'\mathbf{A} \approx \mathbf{I}.$$

Note that when frequency offsets are not incorporated in the system matrix, the CP method reduces to the conventional "sample-the-transform" design method that we discussed in the previous chapter. Alternatively, the pulse samples can be obtained via applying Eq. 3.5 to the original minimization problem (Eqs. 3.1, 3.2):

$$(3.9) \qquad\qquad \hat{\mathbf{b}} \;=\; \arg\min_{\mathbf{b}} \;\; \{\|\mathbf{A}\mathbf{b} - \mathbf{d}\|_{\mathbf{W}}^2 + \beta\mathbf{b}'\mathbf{b}\},$$

subject to

$$(3.10) \qquad\qquad |b_j|^2 \leq C, \quad j = 0, ..., N_t - 1,$$

in which $\mathbf{W}$ is an $N_s \times N_s$ diagonal matrix containing the user-selected error weighting, $\{w(\mathbf{x}_i)\}_{i=0}^{N_s-1}$, that can be used to specify spin-free regions as "don't care" regions. The $\mathbf{W}$-weighted 2-norm denotes $(\mathbf{A}\mathbf{b} - \mathbf{d})'\mathbf{W}(\mathbf{A}\mathbf{b} - \mathbf{d})$.

The dimensions of matrix $\mathbf{A}$ depend on the sample spacing in $\mathbf{m}$ and $\mathbf{d}$, and the length of the RF pulse being designed. Indeed, sample spacing in $\mathbf{m}$ and $\mathbf{d}$ dictates whether the system of equations $\mathbf{A}\mathbf{b} = \mathbf{d}$ would be overdetermined or underdetermined, when no regularization is applied. We found that it is generally beneficial, in terms of excitation error evaluated over the continuous spatial domain, to sample $d(\mathbf{x})$ finely (with higher resolution than that supported by the trajectory) so that the unregularized design problem $\mathbf{A}\mathbf{b} = \mathbf{d}$ is overdetermined.

One can now invoke the Karush-Kuhn-Tucker (KKT) Theorem in non-linear optimization theory [88] to solve Eqs. (3.9) and (3.10). The theorem states that if $\mathbf{b}^*$ is a *regular point* and a local minimizer to the problem, there exists non-negative real *Lagrange multipliers* $\{\lambda_j^*\}_{j=0}^{N_t-1}$ such that for $j = 0, ..., N_t - 1$,

$$(3.11) \qquad\qquad \lambda_j^* \cdot (|b_j^*|^2 - C) = 0,$$

and the gradient of the *Lagrangian function* evaluated at $\mathbf{b}^*$ equals $\mathbf{0}$:

$$(3.12) \qquad \nabla\{\|\mathbf{Ab}^* - \mathbf{d}\|_\mathbf{W}^2 + \beta\mathbf{b}^{*\prime}\mathbf{b}^* + \sum_{j=0}^{N_t-1} \lambda_j^*(|b_j^*|^2 - C)\} \;=\; \mathbf{0}.$$

Eqs. (3.11) and (3.12) have to be solved simultaneously for the optimizer. One can use commercial optimization packages (for example, Optimization Toolbox in Matlab) to tackle the problem, although conversion of the problem to a real-valued one may be necessary, and the process can be computationally expensive. If the multipliers are known *a priori*, $\mathbf{b}^*$ can be obtained, due to the convexity of the Lagrangian function, via

$$(3.13) \qquad \mathbf{b}^* = \arg\min_\mathbf{b}\{\|\mathbf{Ab} - \mathbf{d}\|_\mathbf{W}^2 + \beta\mathbf{b}'\mathbf{b} + \mathbf{b}'\mathbf{\Lambda}^*\mathbf{b}\},$$

where $\mathbf{\Lambda}^* = \text{diag}\{\lambda_j^*\}$. Therefore it suggests that a magnitude-constrained RF pulse can be designed via

$$(3.14) \qquad \hat{\mathbf{b}} \;=\; \arg\min_\mathbf{b}\left\{\|\mathbf{Ab} - \mathbf{d}\|_\mathbf{W}^2 + \beta\mathbf{b}'\mathbf{b} + \mathbf{b}'\mathbf{\Lambda}\mathbf{b}\right\},$$

where $\mathbf{\Lambda} = \text{diag}\{\lambda_j\}$, with $\lambda_j, j = 0, ..., N_t - 1$ denoting regularization parameters controlling the magnitude of individual RF pulse samples. $\mathbf{\Lambda}$ is predetermined by the designer, and does not necessarily equal the optimal $\mathbf{\Lambda}^*$. One can describe $\mathbf{b}'\mathbf{\Lambda}\mathbf{b}$ as a *local regularization* term for controlling peak RF power, whereas $\beta\mathbf{b}'\mathbf{b}$ is the global *Tikhonov regularization* term, often used in other imaging applications, to control integrated RF power. Regularization may degrade the fit between the resulting and desired pattern in exchange

for reducing integrated and peak pulse power. The tradeoff can be tuned by the regularization parameters. Slight Tikhonov regularization is generally needed to ensure that pulses are physically realizable.

For a certain set of regularization parameters, the designed pulse can be constraint-violating and thus the parameters have to be incremented. One heuristic approach to search for a good set of parameter values is to iteratively check integrated and peak RF power, increment β in case of integrated power violation and λ_j in case of peak power violation at pulse sample b_j, and then redesign with the new parameter values, until the integrated power is acceptable and the peak power is within amplifier limitation. This "check-and-redesign" process is sensible, because for practical pulse design problems, the RF power constraints are often not violated. The peak power constraint violation may occur at very few time points, if at all. Thus all or most of the regularization parameters can be zero. In such cases, the heuristic approach is computationally economical because it avoids simultaneously solving for the optimal pulse and KKT multipliers.

For Eq. 3.14, if the regularization parameter values are fixed, then $\hat{\mathbf{b}} = (\mathbf{A}'\mathbf{W}\mathbf{A} + \mathbf{R})^{-1}\mathbf{A}'\mathbf{W}\mathbf{d}$, where $\mathbf{R} = \mathbf{I}\beta + \mathbf{\Lambda}$. This analytical solution involves a matrix inversion, which is a computationally intensive $O(N_t^3)$ operation. To reduce the complexity, we instead apply the $O(N_t^2)$ iterative CG algorithm [16], which converges to the optimal pulse over iterations. The complexity reduction can be highly significant for design of long pulses. One can initialize CG with a CP design for a good initial guess. Alternatively, one can initialize with a zero pulse without loss of excitation accuracy, provided that enough iterations are used.

3.3 Simulation and scanner experiments

In this section, I will illustrate the merits of the iterative pulse design method over CP, using results from Bloch equation simulation and simple scanner experiments. Note, again, that when off resonance is not considered, CP reduces to the conventional "sample-the-transform" design method that we discussed in the previous chapter. I will first go through the general setups of the experiments. Subsequently I will present and discuss the method and results of individual experiments.

3.3.1 Pulse computations

RF pulses were computed offline with Matlab 6.5 (MathWorks Inc., Natick, MA). They were spatially selective in the two transverse dimensions. In all cases, single-shot spiral-out excitation k-space trajectories [89] were used, with the following gradient parameters: maximum magnitude = 4 G/cm, maximum slew rate = 18000 G/cm/s, and sampling period = 4 μs. Unless otherwise stated in specific experiments, we used a trajectory which supported 0.5 cm × 0.5 cm resolution, and an excitation field of view (XFOV) of 18 cm diameter, resulting in pulse duration of 9.01 ms.

The desired patterns had common resolution of 0.25 cm × 0.25 cm. In the simulations, the desired pattern was a 15 cm × 5 cm block, with magnitude 0.5 (unit magnitude corresponded to 90 degree tip angle), perfectly sharp edges, and 0 phase everywhere. Excitation error was equally weighted, either within a circular ROI with 20 cm diameter, or an elliptic reduced ROI, with length of major and minor axes being 18 cm and 12 cm, respectively. Outside the ROIs were "don't care" regions assigned with 0 error weighting. This setup simulated inner volume excitation of a block inside a human skull for spectroscopic imaging [60], for which the elliptic ROI covered the head within the FOV. Desired patterns and ROIs in the scanner experiments will be detailed in the Scanner Experiments Section.

The CG algorithm in the iterative method was initialized with a zero pulse, and run for 15 iterations for sufficient convergence. Except in Simulation III, Tikhonov regularization with $\beta = 2.25$ was used to avoid physically unrealizable pulse designs. Off resonance was considered in Simulation II and Scanner Experiment II. For comparison with the iterative method, CP was regarded as the standard. DCFs for CP designs were calculated based on the Jacobian formula [73].

3.3.2   Numerical simulation setup

To evaluate RF pulses, numerical simulations of the Bloch equation were performed with Matlab. The Bloch simulation was over a 2D grid covering a 20 cm $\times$ 20 cm region, with 0.25 cm $\times$ 0.25 cm resolution. Relaxation effects were ignored. In Simulation II, a field map was incorporated in the Bloch simulator. For each excitation result from the Bloch simulator ($\mathbf{m}_{bl}$), we calculated the normalized root-mean-square excitation error (NRMSE) with respect to the desired pattern. NRMSE was defined as $\|\mathbf{m}_{bl} - \mathbf{d}\|_{\mathbf{W}} / \|\mathbf{d}\|_{\mathbf{W}}$. Note that for both the iterative and CP methods, the same $\mathbf{W}$ was used for error calculation, and it covered the same ROI incorporated in the iterative scheme.

3.3.3   Scanner experiment setup

Scanner experiments were performed on a GE 3 T Signa Scanner (GE Healthcare, Milwaukee, WI), using a spherical homogeneous water phantom (GE Healthcare). 2D excitation patterns were imaged by a spin-echo (SE) spiral-out pulse sequence, in which the slice-selective sinc pulse was replaced by the 2D pulse designs. The 180-degree pulse was slice-selective, restricting the signal source to one slice. Prescans for ROI and field map (Experiment II) were acquired by a GRE spiral-out sequence. Eight acquisition interleaves were used in all sequences to minimize the off resonance effect during acquisition. Other common imaging parameters were as follows: slice thickness = 3.0 mm, FOV = 20

cm, matrix size = 64×64, T_R = 1 s, and T_E = 40 ms (SE), 7.6 ms (GRE). In each of the two experiments, flip angles of patterns being compared were matched via proper scaling of the pulses. For the 2D pulses, gradient waveforms for excitation were shifted forward by 145 μs to compensate for the delay between RF and gradient channels. Images were reconstructed from the scanner data using a fast implementation of the off-resonance compensated CP method [15]. It used field maps estimated from two images acquired with a T_E difference of 2 ms [90]. By using a SE sequence with multiple interleaves and an off resonance compensated reconstruction scheme, image artifacts due to off resonance during acquisition were insignificant.

3.3.4   Simulation I: k-space undersampling
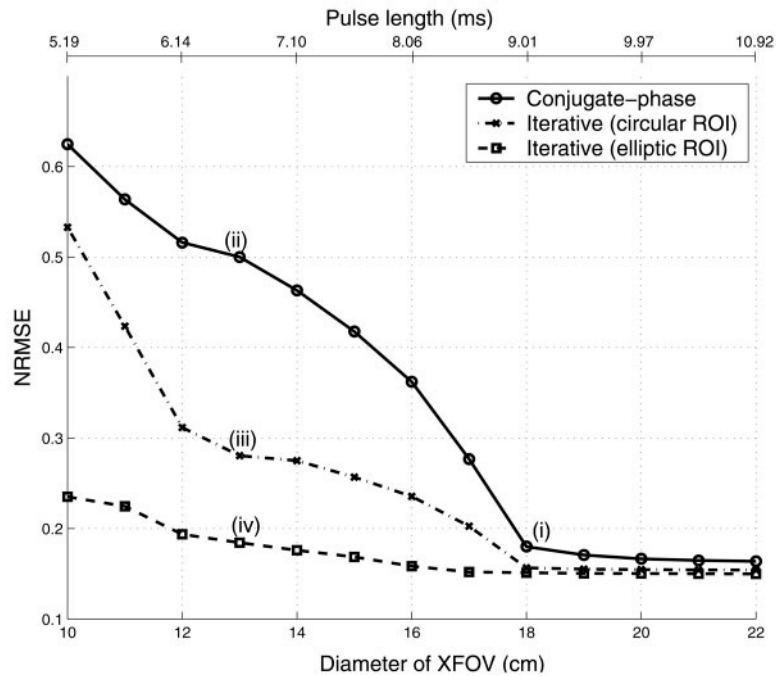
Figure 3.1: Within-ROI excitation error resulting from RF pulses designed for spiral trajectories with different XFOV (resolution held fixed). For a given trajectory, higher excitation accuracy was achieved by the iterative method, especially when the trajectory undersampled k-space. Reduction in size of ROI in the iterative method led to better within-ROI accuracy and higher tolerance of k-space undersampling. The excitation patterns and pulses at points (i)-(iv) are shown in Fig. 3.2 and 3.3.

The goal of Simulation I was to compare the CP and iterative methods used in conjunction with trajectories that undersample excitation k-space. Spiral-out trajectories being tested covered a fixed range in k-space, while the sampling interval was varied, leading to XFOV diameters ranging from 10 cm to 22 cm. For each XFOV diameter value, we computed the corresponding RF pulse designed via CP, and iterative method with either the circular or elliptic ROI. Gradient and RF pulse waveforms were then fed into the Bloch simulator, and within-ROI NRMSE was computed.

a

CP (i) : Pulse length = 9.01 ms
         NRMSE = 0.18

b

CP (ii) : Pulse length = 6.62 ms
          NRMSE = 0.50

c

Iterative with circular ROI (iii) :
        Pulse length = 6.62 ms
        NRMSE = 0.28

d

Iterative with elliptic ROI (iv):
        Pulse length = 6.62 ms
        NRMSE = 0.18
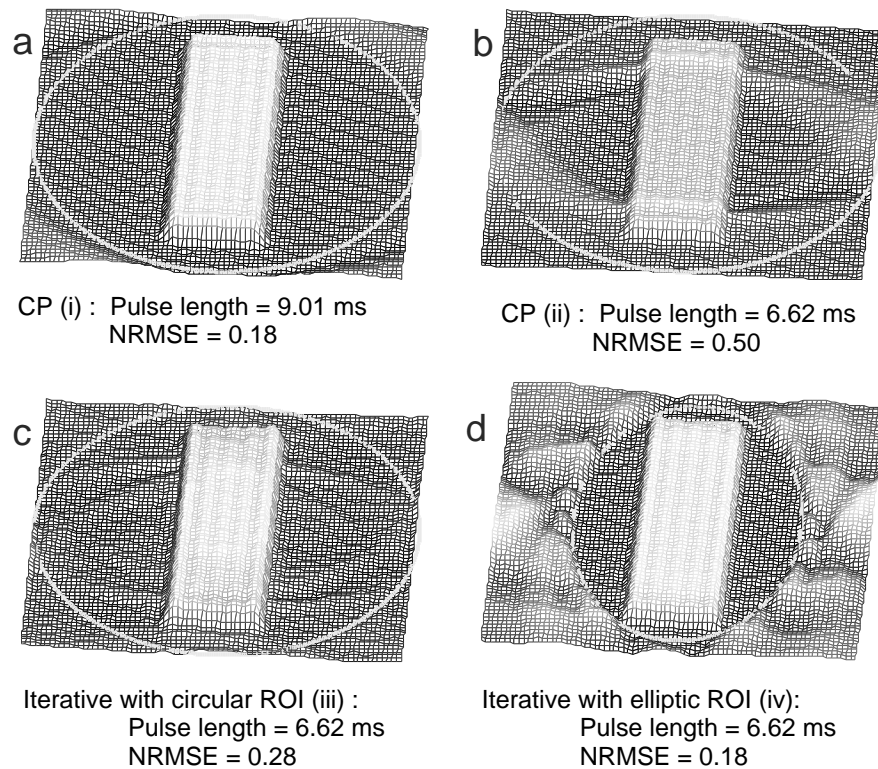
Figure 3.2: Simulated excitation patterns corresponding to points (i)-(iv) in Fig. 3.1, respectively. Interior regions of the solid lines represent the circular or elliptic ROI. a: Pattern by an adequately-sampling trajectory and a CP-designed pulse (i). b-d: Patterns by a common trajectory that undersampled k-space (XFOV = 13 cm), accompanied by pulses designed with CP (ii) or the iterative method, with different ROI specification (iii,iv).

Fig. 3.1 shows the within-ROI NRMSE versus XFOV diameter for each design method
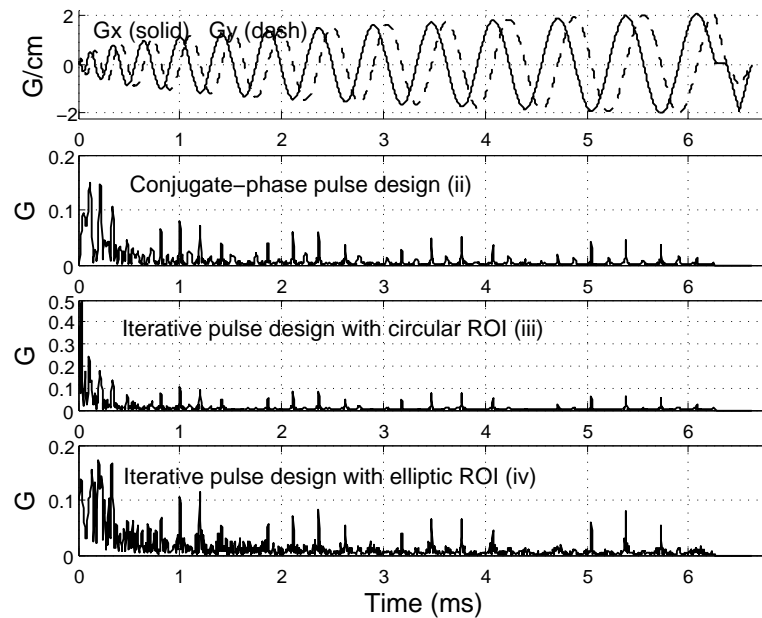
Figure 3.3: Gradient and RF (magnitude) waveforms used to produce excitation patterns in Fig. 3.2b-d, corresponding to points (ii)-(iv) in Fig. 3.1. Despite the same gradient waveforms and desired pattern in use, the RF pulse designs differed significantly. (G: Gauss)

in Simulation I. Compared to CP, the iterative method, regardless of ROI specification, led to lower within-ROI NRMSE for all XFOV diameter values. When XFOV diameter was 18 cm (adequate XFOV for our desired pattern), iterative method using the circular ROI outperformed CP, whereas iterative method using the elliptic ROI outperformed CP by a slightly larger margin. The margins became significant larger when k-space was undersampled, revealing the excitation accuracy advantage by the iterative method, and the further benefit of reducing ROI size. With CP, k-space undersampling led to excitation aliasing within ROI. The iterative method was efficacious in suppressing the aliasing effect, as the effect was accounted for in the optimization cost function, and thus minimized. ROI size reduction gave extra degrees of freedom towards better excitation accuracy.

These results also suggest that a given desired excitation accuracy can be achieved with

a shorter trajectory, using the iterative method instead of CP. The iteratively designed pulse at (iv) on Fig. 3.1 produced within-ROI accuracy close to the one by CP at (i), but its pulse length was significantly shorter (6.62 ms at (iv), 9.01 ms at (i)).

Fig. 3.2 shows the excitation patterns corresponding to (i)-(iv) on Fig. 3.1, whereas Fig. 3.3 displays the gradient and RF (magnitude) waveforms corresponding to (ii)-(iv). Although the same k-space trajectory was deployed, the design methods produced significantly different RF pulses. The iteratively-designed pulse at (iii) had a spike corresponding to a k-space location close to the origin, which could lead to peak power violation. Simulation III illustrates how regularization can be applied to suppress the spike.

3.3.5   Simulation II: off resonance correction

In Simulation II we compared the design methods' capability of correcting for off resonance during excitation. The Bloch simulator was incorporated with a field map with flat regions in the center (+60 Hz) and background (-60 Hz), bridged by a linear transition region (Fig. 3.4). The width of the linear transition region was varied to represent different roughness of the field map, with the central +60 Hz region fixed. For each transition steepness value, we simulated pulses designed with field-map-incorporated CP and iterative method, using either the circular or elliptic ROI. In all cases, NRMSE was evaluated *only* within the transition region inside the ROIs.

Fig. 3.5 shows within-ROI NRMSE in the transition region plotted against off resonance gradient magnitude. Pulses designed with CP produced increasingly distorted excitation in the transition region as the region became steeper. The degradation was consistent with results from other research studies which reported that the analogous CP reconstruction method could not correct well for rough field maps [16]. On the other hand, iteratively designed pulses were relatively immune to large off resonance gradients. The excitation

44
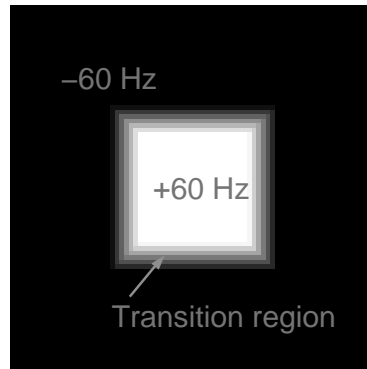
Figure 3.4: Field map incorporated in the Bloch simulator and design methods in Simulation II.
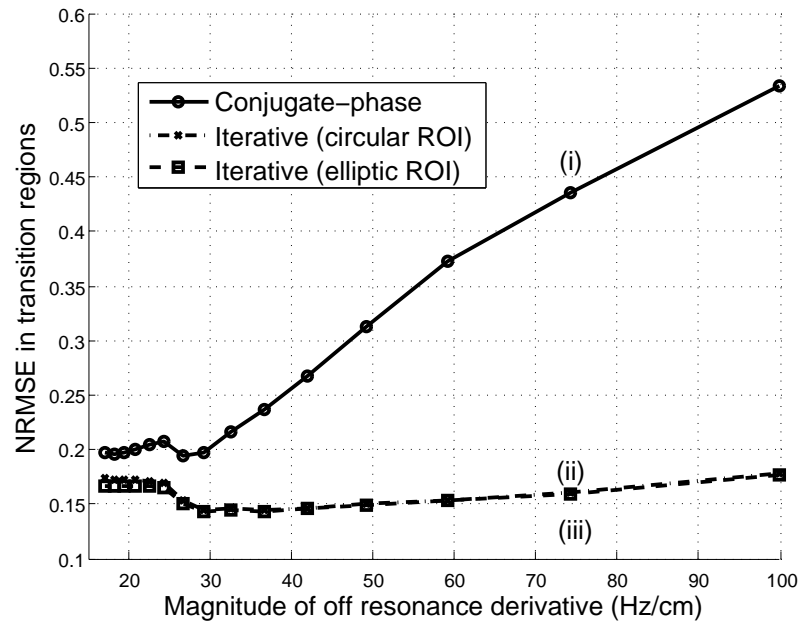
Figure 3.5: NRMSE in the transition region within ROI, versus the region's steepness. As the transition became more rapid, performance of the CP-designed pulses degraded, whereas the iteratively designed pulses were relatively immune. Fig. 3.6 shows excitation patterns at points (i)-(iii).
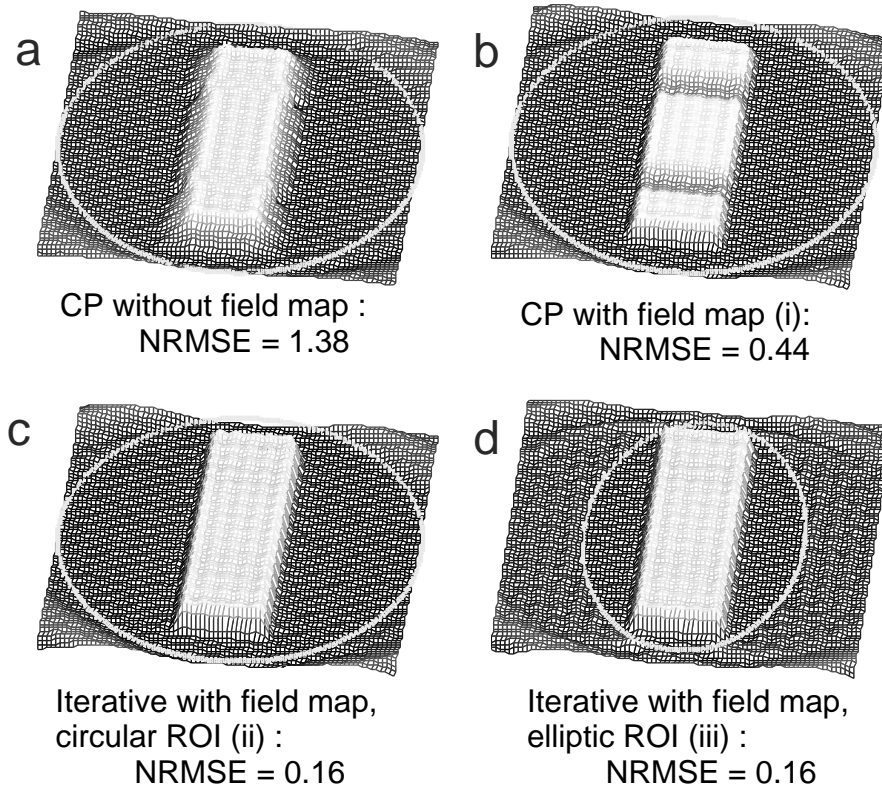
Figure 3.6: a: Simulated excitation pattern by a pulse designed using CP without incorporation of the field map in the simulator, with transition region at 75 Hz/cm. b-d: Patterns by pulses designed with field-map-incorporated CP (point (i) in Fig. 3.5) or iterative method, with different ROI specification (ii,iii). Interior regions of the solid lines represent the circular or elliptic ROI.

performance degraded relatively slowly as the gradient increased. Specification of the elliptic ROI in the iterative method did not have much effect on excitation accuracy.

Fig. 3.6a shows excitation pattern by a pulse designed with CP *without* field map incorporation, at gradient magnitude 75 Hz/cm. Without field map incorporation, the pattern was blurred due to off resonance. Patterns underlying (i)-(iii) in Fig. 3.5 are juxtaposed in Fig. 3.6b-d. In regions with zero off resonance gradient, both design methods led to apparently equal excitation accuracy. Yet, off resonance gradient in the transition region differentiated the pulses. It is surprising that degradation in Fig. 3.6b turned out to be

spatially localized.

3.3.6 Simulation III: RF pulse power management

Simulation III demonstrated the use of regularization for controlling integrated and peak RF power. The iteratively-designed pulse in Simulation I, with circular ROI, XFOV = 13 cm and $\beta = 2.25$, was treated as the original pulse. In two separate studies, we attempted to reduce its integrated power by 50% and the peak power by 75%.

For integrated power reduction, the original pulse was redesigned via iteratively incrementing β by 1.0 and rerunning the iterative scheme, until the integrated power was below 50% of the original. For peak power reduction, the original pulse was redesigned via iteratively locating pulse samples which violated the peak magnitude constraint (50% of the original peak), incrementing the local regularization parameters $\{\lambda_j\}$ at those violation points by 1.0, and rerunning the iterative scheme using the updated parameter values, until the peak RF power was below 50% of the original. As the local regularization parameters were varied, the original Tikhonov regularization ($\beta = 2.25$) was kept.

The NRMSE penalty induced by regularization was compared to that by simply scaling the original pulse by $1/\sqrt{2}$ or clipping at half of its maximum magnitude. Fig. 3.7a shows the original pulse (blue; same pulse as in the third panel of Fig. 3.3), and its redesigned versions (green, red) with Tikhonov regularization parameter β incremented to 5.25 and 11.25, respectively. Tikhonov regularization influenced the entire pulse, but predominantly on its early portion corresponding to the proximity of the k-space origin. Thus, we zoom in the pulses over the first half millisecond. The potentially unrealizable spike in the original pulse was significantly reduced with $\beta = 5.25$. It shrinked by 50% with $\beta = 11.25$, as the integrated power was roughly halved relative to the original pulse. The pulses were significantly different from scaled versions of the original pulse.
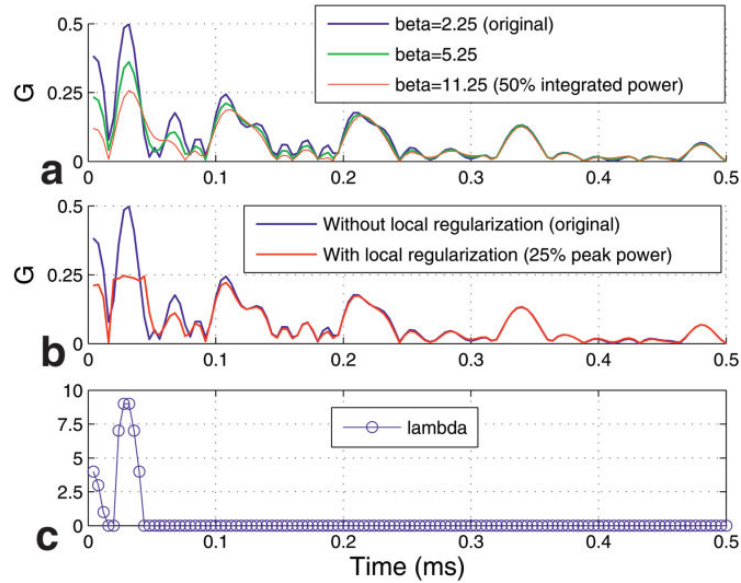
Figure 3.7: a: The original pulse (blue; same pulse as in third panel in Fig. 3.3) designed with Tikhonov regularization ($\beta = 2.25$). The pulse over the first half millisecond is plotted. Incrementing β reduced the spike height and integrated pulse power (green, red). b: Original pulse (blue), and the pulse redesigned with local regularization. Its peak power was about 25% of the original. c: The local regularization parameters used for the redesigned pulse in b. (Note: pulse magnitude is plotted in Gauss (G).)

Simulated profiles of these three pulses (at y = 0 cm) illustrated that integrated power was reduced at a low cost in excitation accuracy (Fig. 3.8). Scaling the original pulse by $1/\sqrt{2}$ was effective in cutting the original power by half, but the accuracy cost was significantly higher than when using Tikhonov regularization ($\beta = 11.25$).

Fig. 3.7b illustrates using local regularization for peak power reduction (spike suppression). The original pulse (blue) is juxtaposed with its redesigned version (red) with roughly 25% of the original peak power, computed iteratively with local regularization parameters plotted in Fig. 3.7c. Compared to the original pulse clipped at half maximum, the redesigned pulse was subtly different, and profile simulation (at y = 0 cm) revealed that it led to significantly better excitation accuracy (Fig. 3.9). Note also that 50% spike suppression was achieved at a lower cost via local regularization, compared to using the globally influential Tikhonov regularization.
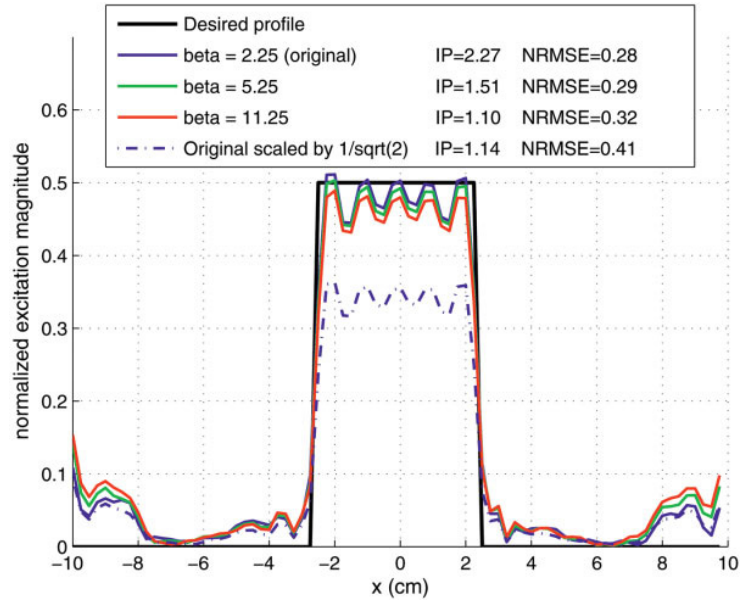
Figure 3.8: Simulated pattern profiles at y = 0 cm, created by the original pulse (blue in Fig. 3.7a), the pulses redesigned with increased Tikhonov regularization (green, red in Fig. 3.7a) and the original pulse scaled by $1/\sqrt{2}$. With regularized iterative design method, integrated power (IP) reduction was achieved with low penalty in excitation accuracy. (Note: IP is in arbitrary units.)
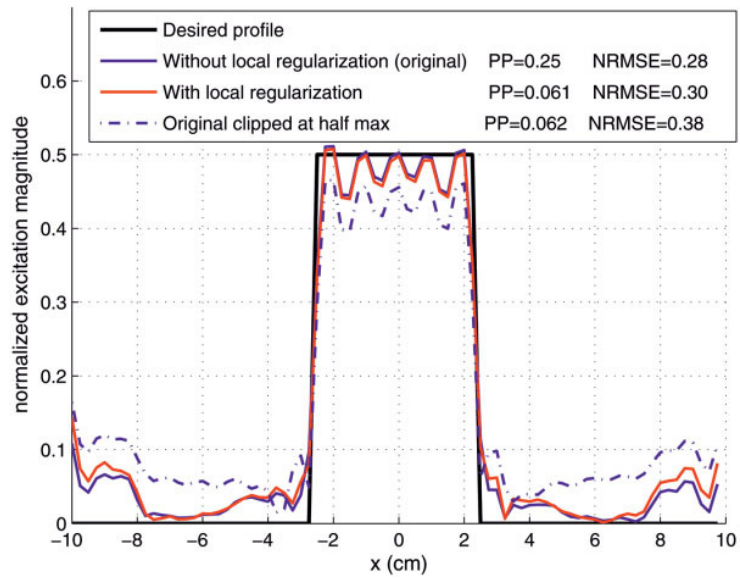
Figure 3.9: Simulated pattern profiles at y = 0 cm, created by the original pulse (blue in Fig. 3.7b), the pulse (red in Fig. 3.7b) redesigned with local regularization parameters in Fig. 3.7c, and the original pulse clipped at half maximum. With regularized iterative design method, peak power (PP) reduction was achieved with a low penalty in excitation accuracy. (Note: PP is in arbitrary units.)

These two examples highlight how the optimization design approach modifies each pulse sample to seek for an optimal tradeoff between pulse power and excitation accuracy.

3.3.7 Scanner experiment I: variable-density trajectory

Variable-density spiral trajectories [74, 91], which undersample k-space regionally, can be useful for pulse length reduction. We investigated whether aliasing could be alleviated when those trajectories were used in conjunction with the iterative design method. Excitation patterns, produced by an identical variable-density trajectory but different RF pulse designs, were imaged and compared. The variable-density spiral-out trajectory we
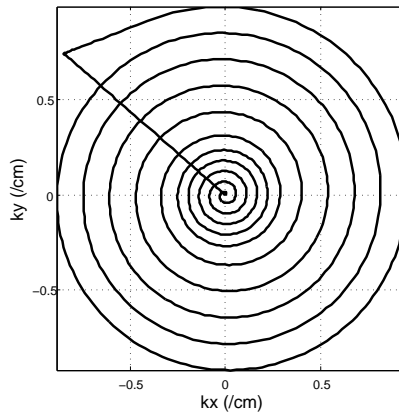
Figure 3.10: Variable-density spiral trajectory deployed in Scanner Experiment I.

deployed adequately sampled excitation k-space near the origin (XFOV = 18 cm), and undersampled by a factor of 2.5 in the high-frequency region (Fig. 3.10). Pulse length was 4.65 ms, and durations of the adequate-sampling and transition (from adequate-sampling to under-sampling) segments were 1.0 ms and 0.8 ms, respectively. To simulate ROI determination in human scanning, the phantom was prescanned with a GRE spiral sequence with a slice-selective sinc pulse, and thresholded the resulting image at 0.3 of its maximum magnitude. CP and (ROI-incorporated) iterative methods were then applied to compute

two RF pulses for the desired pattern, which was a uniform disc with 6 cm diameter and sharp edges. Selective excitation of discs is useful in applications such as inner volume excitation [60] and 2D navigator pulses [92].
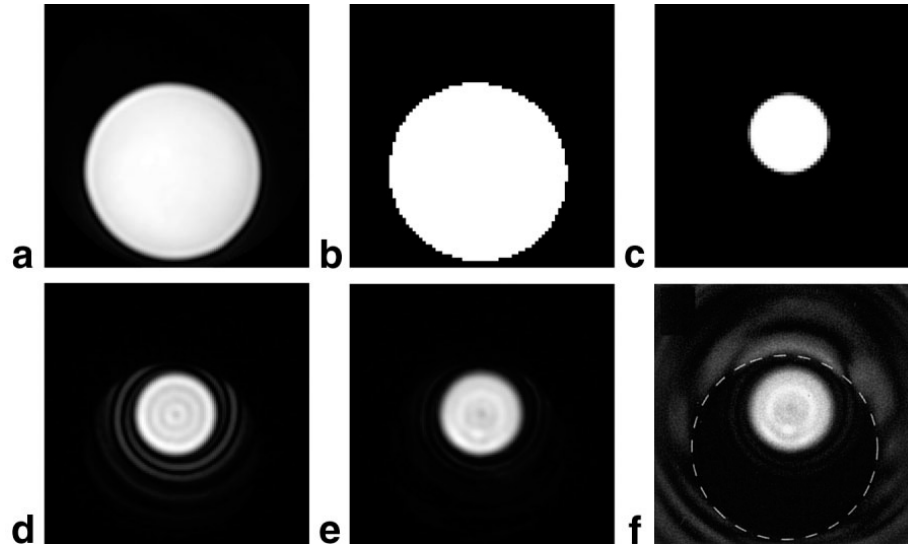
Figure 3.11: a,b: Prescanned image and ROI obtained by thresholding, respectively. c: Desired pattern. d: Measured pattern excited by CP-designed pulse, plagued by aliasing excitation. e: Measured pattern excited by pulse designed with ROI-incorporated iterative method. Compared to the CP case, aliasing was significantly alleviated. f: Bloch simulation result of the iteratively-designed pulse used in e (dash line: ROI).

An ROI was derived from thresholding a prescanned image of the phantom (Fig. 3.11a-b). Fig. 3.11c-e are respectively the desired disc pattern, and patterns excited by two pulses designed with the CP and iterative methods. Notice the aliasing effect in the CP pattern caused by undersampling of the high spatial frequency region, which contained significant energy due to the sharp disc edges. With the iteratively designed pulse, the aliasing effect was significantly reduced, although the same trajectory was deployed. It was consistent with results of Simulation I, and likewise could be explained by inclusion of the aliasing phenomenon in the optimization cost function being minimized. Bloch simulation of the iteratively-designed pulse (Fig.3.11f) revealed utilization of the extra degrees of freedom in the outside-phantom region towards enhanced within-ROI accuracy.

3.3.8 Scanner experiment II: off resonance correction

This experiment compared the design methods' capability of correcting for excitation distortion due to off resonance during pulse application. Three ferromagnetic metal pieces were attached to the phantom surface to create main field inhomogeneity. With the same 9.01 ms trajectory as in the simulations, one pulse was designed using the iterative method *without* field map incorporation, whereas two other pulses were designed using CP and iterative methods, both *with* field map incorporation. As in the previous experiment, we prescanned the phantom and performed image thresholding to determine the ROI. The resulting excitation patterns were then imaged and compared.

The field map was estimated from two GRE images [90], with T_E values of 7.60 ms and 8.60 ms. It was masked with the ROI, and then smoothed using a regularized weighted least-squares method [93] before incorporation. The desired pattern was an arbitrary "stripes" pattern, which covered the entire phantom and demonstrated off resonance correction well.

Fig. 3.12a-b show the "stripes" desired pattern and the pattern excited by an iteratively-designed pulse *before* the three metal pieces were attached to the phantom surface. Fig. 3.12c shows the field map of the axial plane being imaged, which was inferior to the attached pieces. It revealed global distortion of the main field. Such field inhomogeneity is comparable to, for example, that in brain regions near air cavities in the human skull. The same iteratively-designed pulse, now applied in a distorted field, excited a distorted pattern (Fig. 3.12d). The field map was then incorporated in the design methods. Fig. 3.12e-f show patterns excited by pulses designed with field-map-incorporated CP and iterative methods, respectively. The pattern distortion was significantly alleviated in both cases, but the iteratively designed pulse performed slightly better, as can be observed at regions with high off resonance gradient magnitude (white arrows). Accuracy at regions with low
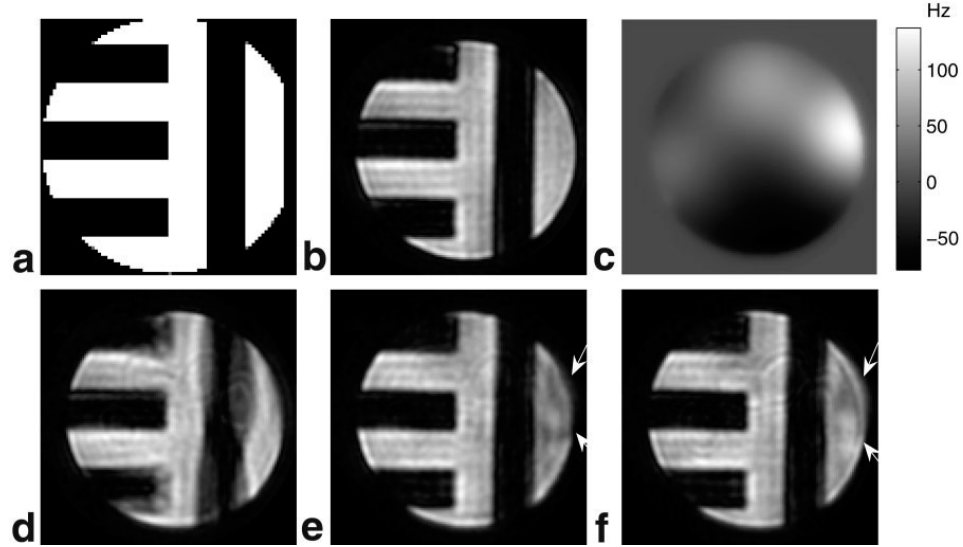
Figure 3.12: a: Desired excitation pattern. b: Pattern by iteratively-designed pulse, before metal pieces were attached to the phantom. c: Field map after attachment of the metal pieces. d: Pattern by pulse in b, distorted due to the inhomogenous field. e: Pattern by pulse designed with CP with field map incorporation. f: Pattern by pulse iteratively designed, with field map incorporation. Field correction by the iterative method was slightly better at regions with high off resonance gradient (white arrows).

gradient magnitude was comparable. These observations were consistent with results in Simulation II. We expect the benefit of the iterative method to be more prominent when using longer pulses (for example, the three-dimensional tailored RF pulse in [46]).

3.4 Extensions of the iterative pulse design

In this section, I will discuss how the iterative approach to designing single-coil spatial pulses can be generalized to other kinds of pulse designs that are facilitated by Fourier interpretations.

3.4.1 Iterative spectral-spatial pulse design

We have seen that via defining joint SPSP k-space variable $\mathbf{k}_{spsp}(t) = (\mathbf{k}(t), k_f(t))^T$ where $k_f(t) = 2\pi(t - T)$, and joint SPSP variable $\mathbf{r} = (\mathbf{x}, f)^T$, we have a Fourier inter-

pretation of SPSP selective excitation (Eq. 2.12):

$$(3.15) \qquad m(\mathbf{r}) \approx \imath \gamma M_0 \int_0^T b_1(t) e^{\imath \mathbf{k}_{spsp}(t) \cdot \mathbf{r}} dt.$$

Similar to spatially selective excitation, it is straightforward to discretize Eq. 3.15 to N_t time points and N_r SPSP locations, and write

$$(3.16) \qquad \mathbf{m}_{spsp} \approx \mathbf{A}_{spsp} \mathbf{b}$$

where $\mathbf{m}_{spsp} = (m(\mathbf{r}_0), \ldots, m(\mathbf{r}_{N_r-1}))^T$, and the elements of the $N_r \times N_t$ system matrix $\mathbf{A}_{spsp}$ are

$$(3.17) \qquad a_{spsp,i,j} = \imath \gamma M_0 e^{\imath \mathbf{k}_{spsp}(t_j) \cdot \mathbf{r}_i} \Delta t.$$

Hence, an SPSP pulse can be iteratively designed via:

$$(3.18) \qquad \hat{\mathbf{b}} = \arg \min_{\mathbf{b}} \left\{ \| \mathbf{A}_{spsp} \mathbf{b} - \mathbf{d}_{spsp} \|_{\mathbf{W}}^2 + R(\mathbf{b}) \right\},$$

where $\mathbf{d}_{spsp}$ is a vector of desired SPSP pattern samples, and $R(\mathbf{b})$ denotes a general regularization term that penalizes RF power.

For designing simple 2D SPSP pulses that are slice and spectrally selective (e.g., exciting a slice of water or fat), there is little advantage for iterative design over the conventional method of separately designing the subpulse shape and spectral envelope (Fig. 2.2). However, the iterative method is potentially convenient for designs that target highly tailored spectral selectivity profiles ("spectral editing"). It also facilitates designs with complicated SPSP desired patterns, which cannot be designed with the conventional method of separate spectral and spatial designs. However, up to date there is no applications in which such complicated patterns are needed. In Chapter 6, we will explore a SPSP signal recovery approach that does involve complicated desired patterns for which the iterative design must be used.

3.4.2 Iterative parallel excitation pulse design

The iterative pulse design formulation for a single coil can be generalized for parallel excitation with multiple transmit coils. Recall from the previous chapter that in the small-tip-angle regime, the aggregate excitation pattern approximately equals the superposition of the patterns by individual coils (Eq. 2.13):

$$(3.19) \qquad m(\mathbf{x}) \quad \approx \quad i\gamma M_0 \sum_{r=1}^{R} s_r(\mathbf{x}) \int_0^T b_r(t) e^{i\mathbf{k}(t)\cdot\mathbf{x}+i\Delta\omega(\mathbf{x})(t-T)} dt.$$

where $b_r(t)$ represents the RF pulse for the rth coil, and $s_r(\mathbf{x})$ is its sensitivity pattern, $r = 1, \ldots, R$. As for single coil (Eq. 3.5), we can discretize time to N_t samples and space to N_s samples:

$$(3.20) \qquad \mathbf{m} \quad \approx \quad \sum_{r=1}^{R} \mathbf{S}_r \mathbf{A} \mathbf{b}_r,$$

where $\mathbf{m} = (m(\mathbf{x}_0), \ldots, m(\mathbf{x}_{N_s-1}))^T$, $\mathbf{S}_r = \text{diag}\{s_r(\mathbf{x}_0), \ldots, s_r(\mathbf{x}_{N_s-1})\}$, $\mathbf{b}_r = (b_r(t_0), \ldots, b_r(t_{N_t-1}))^T$, and $\mathbf{A}$ is the system matrix with elements given by Eq. 3.6. Now, Eq. 3.20 can be rewritten via horizontal concatenation of the matrices $\mathbf{S}_r \mathbf{A}$ and vertical concatenation of the vectors $\mathbf{b}_r$, $r = 1, \ldots, R$, resulting in:

$$(3.21) \qquad \mathbf{m} \quad \approx \quad \begin{pmatrix} \mathbf{S}_1\mathbf{A} & \ldots & \mathbf{S}_R\mathbf{A} \end{pmatrix} \begin{pmatrix} \mathbf{b}_1 \\ \vdots \\ \mathbf{b}_R \end{pmatrix}$$

$$(3.22) \qquad = \quad \mathbf{A}_{full}\mathbf{b}_{full}.$$

It leads to the multiple-coil version of the minimization problem in Eq. 3.14:

$$(3.23) \qquad \hat{\mathbf{b}}_{full} \quad = \quad \arg\min_{\mathbf{b}_{full}} \left\{ \|\mathbf{A}_{full}\mathbf{b}_{full} - \mathbf{d}\|_{\mathbf{W}}^2 + R(\mathbf{b}_{full}) \right\},$$

where $R(\mathbf{b}_{full})$ denotes a general regularization term that is a function of the RF samples. It can comprise the Tikhonov regularization term $\beta \mathbf{b}'_{full} \mathbf{b}_{full}$ for integrated power control,

and/or the local regularization term $\mathbf{b}'_{full}\mathbf{\Lambda}\mathbf{b}_{full}$, where $\mathbf{\Lambda} = \text{diag}\{\lambda_j\}, j = 0, \ldots, R \cdot N_t - 1$, for peak power control. As in the single-coil case, this minimization problem can be solved iteratively using CG.

This "spatial domain" pulse design method is approximately equivalent to the "frequency domain" method by Katscher et al [65], in the special case that (1) a field map is not incorporated in $\mathbf{A}$, (2) error weighting is not specified, and (3) Tikhonov regularization is used. However, in general, the spatial domain method offers the extra advantages of ROI specification, field map incorporation, and faster computation. For further details and experimental results about the iterative parallel excitation pulse design, please read Ref. [94] that Grissom, I, and other coworkers published.

3.5 Discussion

In this chapter, I have introduced an iterative method to design pulses for single-coil, small-tip-angle spatially selective excitation. It is beneficial in several ways.

In simulations and scanner experiments, iteratively designed pulses, which were optimal with respect to the linear design system model, produced significantly more accurate excitation patterns from the Bloch equation, compared to the conventionally designed pulses. I found experimentally that this was generally true, despite the fact that iteratively designed pulses were not optimized with respect to the nonlinear Bloch equation. The accuracy benefit was particularly prominent when the trajectory undersampled k-space (either partially or entirely), since aliasing was taken into account by the optimization scheme when it sought the cost-minimizing pulse. This important feature makes the iterative method stand out from non-iterative ones. Secondly, iteratively designed pulses excited more accurately at spatial regions with large off resonance gradients. This was partially attributable to the obviation of DCF evaluation in the design process. As discussed,

accurate DCF determination is generally difficult in the presence of large off resonance gradients, and DCF errors contribute significantly to excitation error. The iterative method simply does not require the separate task of DCF evaluation.

I have also demonstrated using excitation error weighting for controlling excitation precision at different spatial regions. With the iterative method, designers can assign zero weights to "don't-care" regions and large weights to ROIs. In particular, assigning "don't-care" labels to uninteresting body regions, or regions where there is zero or low spin density (for example, outside-body regions), can boost precision in the ROI.

In addition to precision improvement, the iterative method can potentially lead to shorter pulse lengths, as undersampled k-space can be used at lower penalty of accuracy. In applications such as the 3DTRF method, slightly compromised overall excitation precision may be more tolerable than exceedingly lengthy pulses. Lastly, regularization can be used to trade excitation accuracy for RF power reduction. The global Tikhonov and local regularization techniques enable the designer to avoid suboptimal strategies to make pulses implementable (for example, scaling or clipping). RF power management can be crucial in pulse design problems in high-field MRI.

The cost of all the benefits above is an increase in algorithm complexity, and thus computational time. However, computational time was only a minor issue for 2D designs. On our Linux system with a 3.2GHz processor and 2GB memory, the 15-iteration computation of the pulses in Fig. 3.3 took only 7.07 seconds. However, computational time (and memory) required for pulse designs for volumetric selective excitation (for example, [46, 70]) could be an issue, particularly when off resonance is taken into consideration. In the next chapter about the 3DTRF method, I will propose a computational scheme that accelerates the iterative design significantly.

The iterative method, and its advantages, can be extended to SPSP pulse design, as

well as generalized to pulse designs for parallel excitation. Although currently there is no applications that necessitate iterative SPSP pulse design, it fosters new applications such as the SPSP signal recovery method in Chapter 6. On the other hand, iterative pulse design for parallel excitation has already received considerable attention in the parallel excitation research community. It has been the chosen design method in studies of major research groups (for example, Refs. [95, 96]).

CHAPTER 4

Advanced three-dimensional tailored RF pulse for signal recovery

This chapter is based on materials from Ref. [97].

4.1 Introduction

In the beginning chapter I have reviewed several categories of solutions to the signal loss problem in T_2^*-weighted BOLD fMRI. Amongst those solutions, Stenger et al.'s 3DTRF method [46] stands out to be an appealing candidate for further research and development for routine use. Its advantages include the facts that it does not interfere with scanning parameters, it does not require multiple subimage acquisitions, and it does not require placement and calibration of extra shimming hardware. However, there are technical hurdles to overcome before 3DTRF signal recovery becomes reality in functional studies. The major problem is that the 3DTRF pulses are exceedingly long, hampering fMRI temporal resolution. The accuracy of slice selection is poor, because of slice volume distortion in brain regions where the field is highly inhomogeneous (where the 3DTRF pulses are supposed to be deployed). Also, the original version postulated in Ref. [46] is an offline pulse design – computation does not occur online using in-vivo field inhomogeneity information. It is questionable whether the design process, if field inhomogeneity is to be accounted for, is fast enough so that online computation can be completed in reasonable times.

In this chapter I am going to introduce an advanced version of the 3DTRF method that attempts to address these technical challenges. The central component is a novel trajectory in 3D excitation k-space, which provides better k-space sampling efficiency and hence leads to significantly shorter pulses. It also provides slice profiles that are less susceptible to off-resonance distortion. Designed with the iterative pulse design method introduced in the previous chapter, the 3DTRF pulses account for resonance frequency offsets measured in a separate scan. It leads to improvement in slice selection accuracy and signal recovery effectiveness. To accelerate the design process, we propose a computational scheme analogous to the so-called *time* and *frequency segmentation* methods in image reconstruction [15, 16, 98, 99]. It makes the 3DTRF method potentially practical for routine fMRI experiments. Towards the end of the chapter we will demonstrate signal recovery with the advanced 3DTRF pulses, in both phantom and human head.

4.2   Synopsis of the 3DTRF method

Let us begin with generalizing the 3DTRF method [46] for an arbitrary field offset pattern. Assuming a 2D imaging scheme, let x,y denote the in-plane dimensions, and z the slice selection direction. Define $\mathbf{r} = (x, y, z)^T$, and let $\Delta B(x, y, z)$ denote the BMS-induced inhomogeneous field. When imaging at slice location z_0, the through-plane differential phase variation at in-plane location (x, y) responsible for signal loss can be described by

$$(4.1) \qquad \phi(x, y, z; z_0) \;\; = \;\; -\gamma T_E[\Delta B(x, y, z) - \overline{\Delta B}(x, y; z_0)],$$

where γ is the gyromagnetic ratio, and $\overline{\Delta B}(x, y; z_0)$ are the mean field offsets around z_0 in the through-plane direction, defined by

$$(4.2) \qquad \overline{\Delta B}(x, y; z_0) \;\; = \;\; \frac{\int p(z - z_0)\Delta B(x, y, z)dz}{\int p(z - z_0)dz},$$

where $p(z)$ is the slice profile. The mean offsets cause in-phase evolution of spin signals, and therefore do not contribute to through-plane dephasing. For T_2^* contrast, T_E needs to be relatively long (typically 30 - 50 ms), and consequently this phase variation is rapid in regions with large field variation. MR signals that originate from integration of spins in those regions are lost due to phase cancellation during readout.

The goal of the 3DTRF method is to *precompensate* for this through-plane phase variation in the excitation stage. In the ideal case, a 3DTRF pulse excites a slice-selective volume, d, with the negative of the phase pattern in Eq. 4.1 embedded:

$$(4.3) \qquad d(\mathbf{r}; z_0) \;\; = \;\; p(z - z_0) \cdot \exp(-\imath\phi(x, y, z; z_0)) \,.$$

This preemptive phase pattern, if realized, would cancel out the through-plane dephasing during T_E, and spins would be in phase when the center of acquisition k-space is sampled at T_E. Signal loss would thus be mitigated. Although the 3DTRF method described here precompensates only for through-plane dephasing, generalization for in-plane dephasing correction may be possible.

4.3   Iterative pulse design

A 3D spatially selective excitation pulse is to be designed *iteratively* for exciting such a phase-precompensating slice volume. We need to first specify the discrete desired pattern by sampling the ideal one, $d(\mathbf{r}; z_0)$, over a 3D Cartesian grid (criteria for adequate sampling of $d(\mathbf{r}; z_0)$ will be discussed in the Implementation section). Let $d_i = d(\mathbf{r}_i; z_0), i = 0, ..., N_s - 1$ be the desired pattern samples over the 3D Cartesian grid, and define complex vector $\mathbf{d} = (d_0, ..., d_{N_s-1})^T$. Using the iterative pulse design, complex 3DTRF pulse samples, $\hat{\mathbf{b}} = (\hat{b}_0, ..., \hat{b}_{N_t-1})^T$, can be computed via solving the following unconstrained

minimization problem:

$$(4.4) \qquad \hat{\mathbf{b}} \;=\; \arg\min_{\mathbf{b}} \left\{ \|\mathbf{Ab} - \mathbf{d}\|_{\mathbf{W}}^2 + R(\mathbf{b}) \right\},$$

where $\mathbf{A}$ is an $N_s \times N_t$ system matrix with elements given by Eq. 3.6 in Chapter 3. $R(\mathbf{b})$ denotes a general penalty function that, if defined as $\beta \mathbf{b}'\mathbf{b}$ and $\mathbf{b}'\mathbf{\Lambda}\mathbf{b}$, can be used to control integrated and instantaneous RF pulse power, respectively. These power penalties can be tuned through parameters β and $\mathbf{\Lambda} = \text{diag}\{\lambda_j\}, j = 0, ..., N_t - 1$. The minimization problem can be solved iteratively using CG.

Incorporating off resonance effects in the system matrix (Eq. 3.6) is crucial in context of the 3DTRF method, because the pulses are relatively long and are deployed in brain regions with severe field inhomogeneity. Unfortunately, in doing so, the Fourier relationship between excitation pattern and k-space is ruined. The efficient FFT cannot be used directly in mappings between excitation pattern and k-space, as needed in CG [16]. Acceleration techniques are needed for the computational time of the design problem to be practical, as addressed in a subsequent section.

4.4 An echo-volumar trajectory

The effectiveness of the RF pulse designed via Eq. 4.4 depends greatly on the choice of k-space trajectory in Eq. 3.6. Aiming at high sampling efficiency and excitation accuracy, we can tailor an appropriate 3D trajectory for the 3DTRF method.

The 3DTRF method has to meet high demands in the slice selection direction. The pulses need to have XFOV in z wide enough to cover the range over which MR signals can arise, and excitation resolution fine enough for rendering rapid phase variations and narrow slice profiles. In contrast, the in-plane requirements are relatively less stringent, because in-plane excitation resolution can be low due to the smooth in-plane variation of the desired pattern. The stack-of-spirals trajectory in Ref. [46], which "phase-encodes"

in z, and "frequency-encodes" in x, y, is suboptimal for the 3DTRF method. While it can efficiently support high in-plane XFOV and resolution, it is inefficient in meeting demanding z-direction requirements. Also, phase-encoding in z produces slice profiles vulnerable to off-resonance distortion.
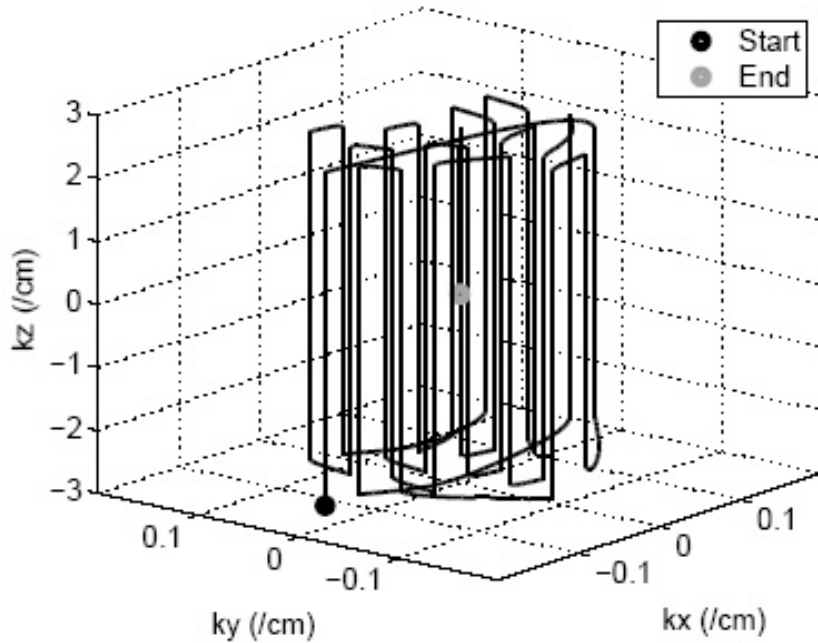
Figure 4.1: EV trajectory in 3D excitation k-space, used in the following phantom experiment. It frequency-encodes in the slice-selection direction, and phase-encodes in-plane.

We propose a novel trajectory in 3D excitation k-space that frequency-encodes in z and phase-encodes in x, y (Fig. 4.1). It traverses back and forth along the k_z direction. Such traversal can be produced by an oscillative z gradient waveform, subject to the maximum gradient magnitude and slew rate constraints (Fig.4.2b). The oscillative z gradient can be trapezoidal, sinusoidal, or of any other shape so long as it provides the desired oscillative k_z locus. In between the forward and backward k_z traversals, x and y gradient blips are deployed to take the trajectory to predetermined phase-encoding locations in k_x, k_y (Fig. 4.2a). As a result, the 3D trajectory cyclically sweeps k_z (in either positive or

63

negative direction) at a particular k_x, k_y location, and then migrates to another one. The

cycle continues until the trajectory visits $k_x, k_y = (0,0)$, and finally lands on the origin of

excitation k-space. Such a 3D trajectory resembles the one used in blipped echo-volumar

imaging (EVI) [100], and hence we coin it an echo-volumar (EV) trajectory, as extension

of the echo-planar trajectories in the pulse design literature (for example, [101]).
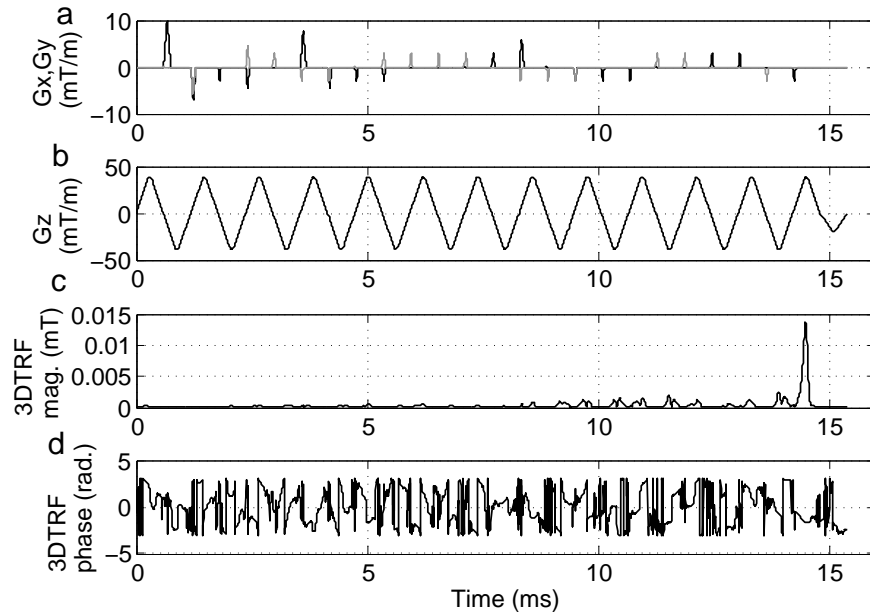
Figure 4.2: 3DTRF pulse used in the following phantom experiment. a: x- (black) and y- (gray) gradient waveforms that produce the k_x, k_y displacements of the EV trajectory in Fig. 4.1. b: z-gradient waveform that produces the k_z sweeps. c,d: 3DTRF pulse (magnitude and phase) iteratively designed with the trajectory in Fig. 4.1. The magnitude spike close to pulse end corresponds to the trajectory's visit to excitation k-space origin. This 3DTRF pulse is 15.4 ms long.

The EV trajectory eliminates the problem of "excitation sidelobes" in the z direction as

reported in Ref. [46], because during the k_z traversals, RF and z gradient waveforms are

essentially played out "continuously" in the coils after digital-to-analog (D/A) conversion.

Frequency-encoding in z also enables efficient coverage of a wide k_z range, which directly

leads to significant pulse length reduction. It also provides slice profiles that are less

vulnerable to off-resonance distortion.

4.4.1 Determination of phase-encoding locations

Using a fine Cartesian grid of phase-encoding locations in k_x, k_y would be an inefficient sampling strategy that leads to lengthy pulses. Instead, one can pick a modest set of locations, judiciously chosen to help minimize the cost function in Eq. 4.4. The trajectory can adapt to the desired pattern by traversing the highest-energy regions of its spectrum in excitation k-space. One intuitive strategy is to set the N phase-encoding locations to be the k_x, k_y coordinates corresponding to the N largest values in the desired pattern's discrete k_x, k_y power spectrum, obtained via collapsing the 3D power spectrum along the k_z dimension:

$$E(k_{x,i}, k_{y,j}) = \sum_{k=0}^{N_z-1} |D(k_{x,i}, k_{y,j}, k_{z,k})|^2,$$

(4.5)
$$i = 0, ..., N_x - 1, j = 0, ..., N_y - 1,$$

where D denotes the 3D discrete Fourier transform (DFT) of the adequately sampled desired pattern, and N_x, N_y, and N_z are the numbers of samples in the three spatial dimensions.

When off resonance is incorporated in the design process, determining the locations based on the power spectrum of the following "modified desired pattern" generally leads to lower cost (Fig. 4.3):

(4.6)
$$\tilde{d}_i = d_i \cdot e^{\imath \Delta \omega(\mathbf{r}_i)T}, \qquad i = 0, ..., N_s - 1.$$

This modification partially accounts for the off-resonance phase evolution during pulse deployment, and leads to better choice of phase-encoding locations. Further optimization of the encoding locations will be discussed in Chapter 5.

In the presence of field inhomogeneity, ordering of the trajectory's visit to phase-encoding locations critically affects excitation accuracy. The crucial encoding locations
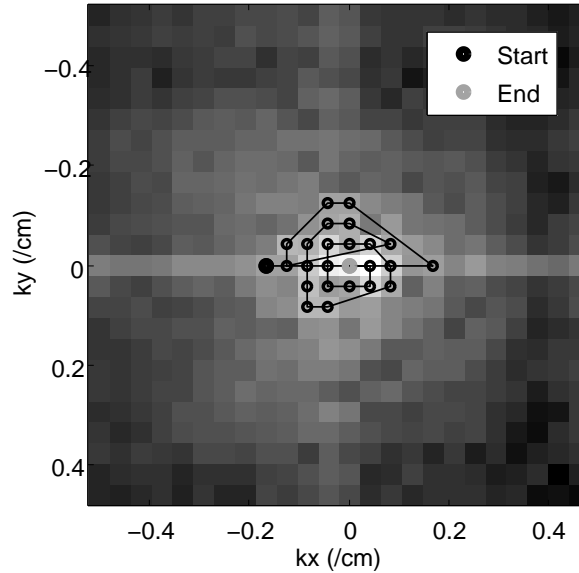
Figure 4.3: Phase-encoding locations in k_x, k_y determined as the locations corresponding to the highest magnitudes in the discrete k_x, k_y power spectrum (underlying, in logarithmic gray scale) of the "modified desired pattern". They are visited by the EV trajectory, which traverses back and forth along k_z, in a "spiral-in" order (solid line).

at k-space center ($k_x, k_y = (0, 0)$) and its proximity should be visited last, so that dephasing and decay of those encoding components is minimized. The EV trajectory can therefore "spiral in" from the high-frequency region toward the center (Fig. 4.3). Such ordering also leads to relatively good off-resonance resilience of the resulting excitation pattern.

4.5 Accelerating the iterative design

4.5.1 Motivation for fast computation

In an fMRI session, 3DTRF pulses for loss-plagued slice locations need to be designed online after a separate field map scan. Therefore, the design process must be reasonably fast. However, solving Eq. 4.4 (with non-zero field map) using CG is computationally demanding, especially in the 3D case with large numbers of desired pattern and pulse samples.

The computational bottleneck in each CG iteration lies in the backward and forward projections: $\mathbf{A}'\mathbf{e}^{(n)}$, where $\mathbf{e}^{(n)} = \mathbf{d} - \mathbf{A}\mathbf{b}^{(n)}$, and $\mathbf{A}\mathbf{b}^{(n)}$ (superscript (n) denotes the nth iteration). When a field map is not incorporated in $\mathbf{A}$ (i.e., $\Delta\omega(\mathbf{r}_i) = 0$), these multiplications can be computed efficiently with the non-uniform fast Fourier transform (NUFFT) algorithm and its adjoint, respectively [102]. NUFFT involves an $O(\kappa N_s \log N_s)$ FFT and an $O(JN_t)$ interpolation at its core, whereas its adjoint involves $O(JN_t)$ interpolation followed by $O(\kappa N_s \log N_s)$ inverse FFT. Here, J is the number of neigboring samples used in interpolation, and κ is the upsampling factor of spatial samples [102]. The NUFFT algorithm and its adjoint provide a huge computation saving when compared to the $O(N_s N_t)$ exact evaluation of the matrix-vector products. However, when field map is incorporated, matrix $\mathbf{A}$ is no longer a Fourier transformation matrix. As a consequence, the fast algorithms cannot be used directly.

An analogous computational issue has been well addressed in the context of off-resonance-compensated image reconstruction. Using the *time segmentation* [15, 16] and *frequency segmentation* [98, 99] methods, reconstruction can be sped up significantly via approximations to the frequency offset exponential term in the magnetic resonance signal equation, and the subsequent use of the efficient (NU)FFT algorithm. These segmentation methods, in the context of CG-based reconstruction, have recently been generalized in [17]. The analogy between reconstruction and small-tip-angle pulse design suggests that similar segmentation techniques can be applied to accelerate the 3DTRF pulse design process.

4.5.2 Framework of segmentation for pulse design

Based on Ref. [17], all of the known approximations to the off-resonance exponential term in Eq. 3.6 are special cases of the following general form:

$$(4.7) \qquad e^{i\Delta\omega(\mathbf{r}_i)t_j} \approx \sum_{l=1}^{L} p_{il}q_{lj}, \qquad i = 0, ..., N_s - 1, j = 0, ..., N_t - 1$$

for various choices of the L pairs of spatial and temporal functions, $\{p_{il}, q_{lj}\}, l = 1, ..., L$. L is the number of "segments", which determines the approximation accuracy. Note that the exponent in Eq. 4.7 has positive sign, and the space and k-space indices are swapped, in contrast to that in the MR signal equation. Ref. [17] describes methods for choosing p_{il} and q_{lj}, corresponding to the temporal interpolators and segments in the time segmentation method, and frequency segments and interpolators in frequency segmentation. In particular, the *histogram-based, least-square time segmentation* approach [17] is summarized in the next section.

Consider the formula of multiplying $\mathbf{A}$ with generic RF pulse vector $\mathbf{b}$. After substituting Eq. 4.7 into Eq. 3.6 and rearranging, the ith element of the product is

$$(4.8) \qquad [\mathbf{Ab}]_i \;\approx\; \imath\gamma\Delta t \cdot e^{-\imath\Delta\omega(\mathbf{r}_i)T} \cdot \sum_{l=1}^{L} p_{il}\Big[\sum_{j=0}^{N_t-1} (q_{lj}b_j)e^{\imath\mathbf{k}(t_j)\cdot\mathbf{x}_i} \Big],$$

and in matrix form,

$$(4.9) \qquad \mathbf{Ab} \;\approx\; \mathbf{S}\cdot\sum_{l=1}^{L}\mathbf{P}_l\mathbf{G}\mathbf{Q}_l\mathbf{b},$$

where $\mathbf{P}_l = \mathrm{diag}\{p_{il}\}$, $\mathbf{Q}_l = \mathrm{diag}\{q_{lj}\}$, $\mathbf{G}$ is an $N_s \times N_t$ adjoint NUFFT matrix with elements $g_{ij} = e^{\imath\mathbf{k}(t_j)\cdot\mathbf{x}_i}$, and $\mathbf{S} = \mathrm{diag}\{\imath\gamma\Delta t \cdot e^{-\imath\Delta\omega(\mathbf{r}_i)T}\}$. Eq. 4.9 depicts the following steps in approximating the multiplication:

1. For $l = 1, ..., L$:

   (a) Multiply RF pulse samples with $q_{lj}, j = 0, ..., N_t - 1$.

   (b) Apply adjoint NUFFT to $q_{lj}b_j$.

   (c) Multiply adjoint NUFFT output with $p_{il}, i = 0, ..., N_s - 1$.

2. Sum the output of the L data branches.

3. Multiply the sum by $\imath\gamma\Delta t \cdot e^{-\imath\Delta\omega(\mathbf{r}_i)T}$.
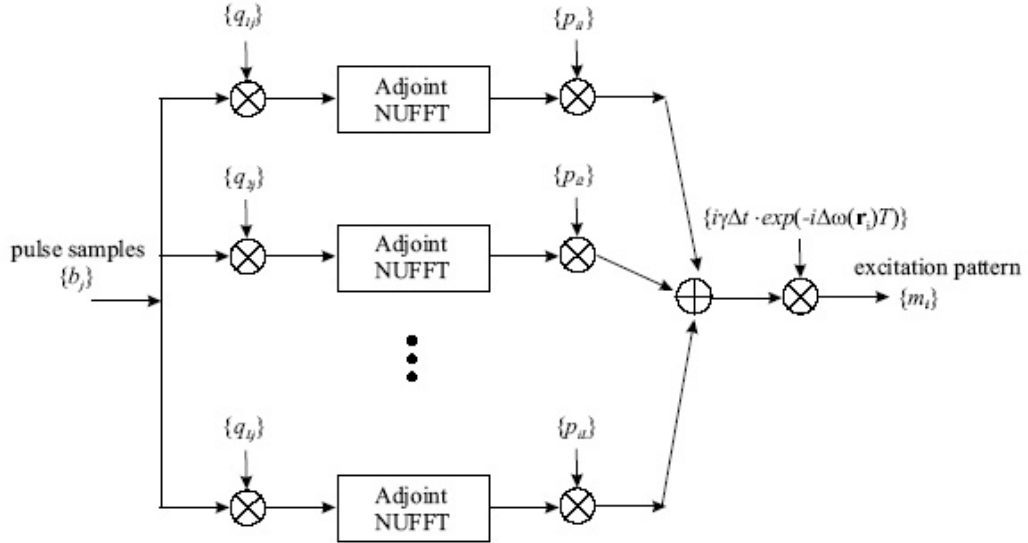
Figure 4.4: Segmentation framework for fast and accurate approximation of generic $\mathbf{m} = \mathbf{A}\mathbf{b}$.

This procedure is illustrated in Fig. 4.4. It can be handled efficiently using L adjoint NUFFT calls, and with good choices of p_{il} and q_{lj}, a small L (4-8 for typical field maps in human head) is usually sufficient for the approximation in Eq. 4.8 to be accurate. Therefore this procedure is significantly faster than the $O(N_s N_t)$ direct implementation of $\mathbf{A}\mathbf{b}$. Similarly, multiplication of $\mathbf{A}'$ with generic spatial vector $\mathbf{e}$ can be approximated with L NUFFT calls. The complexity reductions in each CG iteration lead to significant acceleration of the 3DTRF pulse design process.

4.5.3 Histogram-based, least-square time segmentation

Let me summarize, in the segmentation framework for pulse design acceleration, the *histogram-based, least-square time segmentation approach* [17] in deriving $p_{il}, i = 0, ..., N_s - 1$, and $q_{lj}, j = 0, ..., N_t - 1$. Define uniform time samples $\tau_l, l = 1, ..., L$, within the pulse duration, and form L temporal segments, $p_{il} = e^{i\omega(\mathbf{r}_i)\tau_l}, l = 1, ..., L$. Now, the goal is to determine temporal interpolator, q_{jl}, that we pair up with the l-th segment. Suppose the histogram of the field map, $\Delta\omega(\mathbf{r}_i)$, has K bins, and ω_k and h_k are the center and

occurrence frequency of the k-th bin [1]. Define matrices

$$(4.10) \qquad \mathbf{E} = \{e_{kj}\}, \qquad e_{kj} = e^{\imath \omega_k t_j},$$

$$(4.11) \qquad \tilde{\mathbf{P}} = \{\tilde{p}_{kl}\}, \qquad \tilde{p}_{kl} = e^{\imath \omega_k \tau_l},$$

$$(4.12) \qquad \tilde{\mathbf{Q}} = \{q_{lj}\},$$

$$(4.13) \qquad \mathbf{H} = \text{diag}\{h_k\},$$

where $i = 0, ..., N_s - 1, j = 0, ..., N_t - 1, k = 1, ..., K$, and $l = 1, ..., L$. The L temporal interpolators can be computed by the following histogram-weighted least-square formula:

$$(4.14) \qquad \tilde{\mathbf{Q}} = (\tilde{\mathbf{P}}'\mathbf{H}^2\tilde{\mathbf{P}})^{-1}\tilde{\mathbf{P}}'\mathbf{H}\mathbf{E}.$$

The l-th row in $\mathbf{Q}$, $q_{lj}, j = 0, ..., N_t - 1$, is the temporal interpolator to be paired with segment $p_{il}, i = 0, ..., N_s - 1$. The L pairs are to be used in the segmentation framework. Readers should refer to Ref. [17] for elaboration on this approach and alternative options.

4.6 Implementation

In this section, I elaborate on the field map acquisition and implementation of the 3DTRF pulse design process. Parameter values used in the experiments presented in the subsequent section will also be given.

4.6.1 Scanning for field map

To acquire a field map, a separate scan was performed, in which two multi-slice 2D GRE image sets with an echo time difference, ΔT_E [90], were obtained. ΔT_E should be small enough so that no phase evolution during the period exceeds $\pm\pi$. The field map, in Hz, was estimated by dividing the phase difference between the two image sets by $2\pi\Delta T_E$.

---

[1]Occurrence count of the frequency offset at $\mathbf{r}_i$ could be weighted by the error weighting, W_i.

The prescribed slices should be thin and dense enough to capture the phase variations through the target slices in the actual fMRI study. In-plane resolution can be relatively low. FOV in z should cover the slice locations at where 3DTRF pulses are targeted. In fact, field map coverage larger than the target range is beneficial for off resonance compensation in the design. To exclude fat signals from the pulse design process, fat presaturation was applied to attenuate the fat signals. We thresholded the magnitude images to obtain masks covering only the brain, and then applied the masks to crop out the fat regions in the field map (i.e., assign 0 Hz everywhere except within the brain). The masked map was smoothed in the next step.

In the phantom and human experiments, field maps were acquired with a 2D GRE spiral-out sequence, with common parameters as follows: slice thickness = 0.1 cm, number of slices = 40, flip angle = 60°, FOV_{xy} = 24 cm, matrix size = 64 × 64, T_R = 2 s, T_E = 6.8 ms, number of interleaves = 4, and ΔT_E = 1 ms.

4.6.2 3DTRF pulse design

Fig. 4.5 summarizes the 3DTRF pulse design process with the field map and its associated magnitude images as input. First, regularized in-plane smoothing was applied to the masked field map [103]. The procedure denoised the field map, and extrapolated it into image gaps and background. We then smoothed the field map in the z direction with a 1D Hanning kernel. The magnitude images, which would be used to determine the ROI, were smoothed with a 2D Hanning kernel. This smoothing ensured that the ROI covered brain regions with low signal intensities. Subsequently, the smoothed field map and magnitude images were interpolated onto the lattice grid on which the desired pattern would be specified.

There are several considerations in choosing the desired pattern grid. First, the sam-
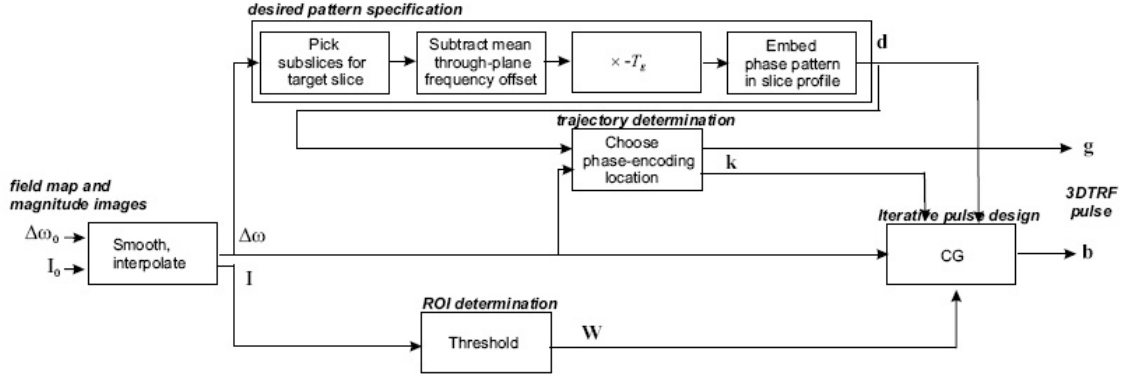
Figure 4.5: Flowchart of the 3DTRF pulse design process, with field map and corresponding magnitude images as input.

pling rates in each spatial dimension should at least match the spatial frequency bandwidth of the continuous desired pattern (Eq. 4.3). Therefore, sampling in z should be fine because of the rapid through-plane phase variation and narrow slice profile, whereas coarser sampling in x, y is allowable, because usually the phase of the desired pattern is smooth in-plane. Second, the sampling ranges in the three dimensions must cover the entire volume of interest, implying that the grid has to cover a wide range of z from which MR signals can arise.

Sampling parameters of the desired pattern in our experiments were as follows: FOV = 24 cm $\times$ 24 cm (x, y) $\times$ 12.8 cm (z), with spacings 1 cm $\times$ 1 cm (x, y) $\times$ 0.1 cm (z).

Desired pattern specification

For the slice targeted for recovery, we selected a set of processed 2D field maps corresponding to the subslices that constituted the target slice. From these field maps, the complex desired pattern was formed based on the discretized version of Eqs. 4.1, 4.2 and 4.3. T_E was defined as the interval between pulse end and time of acquisition k-space origin. Zeros were assigned to desired pattern grid locations outside the slice volume. Finally,

regardless of the target slice location, the desired pattern was specified centered in the z dimension. Slice placement off the iso-center can be achieved by frequency modulation implementable in the pulse sequence.

In both of the experiments, the desired pattern had Gaussian-shaped slice profile with full-width half maximum (FWHM) = 0.5 cm and tip angle = 30°. T_E = 30 ms.

Trajectory and ROI determination

We then proceeded to determine the k-space trajectory based on the field map and desired pattern. We determined the phase-encoding locations from the spectrum of the modified desired pattern (Eq. 4.6). The trajectory's k_z coverage should be large enough for the required slice thickness and through-plane phase variation. Thresholding the interpolated magnitude images generated the ROI that covered the brain where excitation accuracy was important. This threshold should be lower than the one for fat region exclusion, so that brain regions with low signal intensity are included in the ROI.

In the experiments, gradient trapezoids were compliant to the maximum gradient magnitude and slew rate constraints, which were 40 mT/m and 150 T/m/s, respectively. We used 25 phase-encoding locations and k_z coverage of [-2.65,+2.65] cm^{-1}, resulting in pulse length = 15.4 ms. A "spiral-in" ordering of the phase-encoding locations, as illustrated in Fig. 4.3, was adopted.

Iterative pulse design

After determining the field map, desired pattern, trajectory, and ROI, the 3DTRF pulse was designed iteratively with CG, implemented with Matlab (Mathworks Inc., Natick, MA, USA) on a 3.2 MHz Pentium workstation. Tikhonov regularization (with small β) was applied to avoid unrealizable pulse designs. In case of pulse power violation in the final design, one can cyclically increment regularization parameters (β and Λ) and run

extra CG iterations [77], until pulse power is within acceptable range. In the experiments presented here, an *ad hoc* penalty function of the form $\alpha \mathbf{b}' \cdot \text{diag}\{k_x(t_j)^2 + k_y(t_j)^2\} \cdot \mathbf{b}$ was added to Eq. 4.4, which smoothed the in-plane excitation pattern. Similar to β and Λ, α is a design parameter. To accelerate the design as proposed, we precomputed temporal interpolators for the segmentation scheme as described in the Appendix, and NUFFT interpolators based on Ref. [102]. The interpolators were stored and utilized in each CG iteration.

The 3DTRF pulses in the experiments were designed with 50 CG iterations, $\beta = 1$, $\lambda_i = 0$, all i, and $\alpha = 5000$ (with trajectory samples in cm^{-1}). RF pulse computation was accelerated with the histogram-based, least-squares time segmentation method. There were 8 bins in the field map histogram ($K = 8$), and 4 temporal segments at uniform intervals ($L = 4$). For the NUFFT algorithm [102], 4 neighbors for interpolation ($J = 4$) and an upsampling factor of 2 ($\kappa = 2$) were used in all three dimensions.

The outputs of the design process were magnitude and phase waveforms for the RF envelope to be frequency modulated, accompanied by gradient waveforms underlying the 3D trajectory. These waveforms were incorporated into the pulse sequence.

4.7   Phantom and human experiments

Scanner experiments were conducted on our GE 3 T Excite MRI scanner (GE Healthcare, Milwaukee, WI, USA), with a head coil for both transmission and reception. The phantom experiment was performed on a spherical homogeneous water phantom. A healthy volunteer participated in the human experiment, approved by the Institutional Review Board of the University of Michigan, after providing informed consent. In both phantom and human experiments, high-order shimming was performed prior to field map acquisition. Gradient and RF waveforms were shifted slightly to compensate for delays between

the RF and gradient channels. 2D images were reconstructed using the off-resonance-compensated conjugate-phase method [15].

4.7.1 Signal recovery in phantom

The goals of the experiment were (1) to demonstrate signal recovery using a 3DTRF pulse in a homogeneous water phantom; (2) to image the slice volume excited by that 3DTRF pulse, using a 3D imaging sequence. With the slice volume image, we evaluated fidelity of the magnitude and phase profiles of the excited slice.

To induce an inhomogeneous field, a small piece of ferromagnetic metal (half piece of staple) was attached to the phantom surface, 6 cm inferior to the imaging plane at isocenter. The created inhomogeneous field led to signal loss in a GRE image at iso-center, acquired with a conventional 3.2 ms-long, Hanning-windowed, sinc-shaped (with 1 sidelobe) RF pulse that was selective for a 5-mm slice. The other imaging parameters were as follows: spiral-out acquisition with matrix size 128×128, FOV = 24 cm, 8 interleaves, $T_E = 30$ ms, $T_R = 1$ s, and flip angle = 30° (matched with the 3DTRF case). The use of small pixel size and multiple interleaves minimized image artifacts due to in-plane dephasing and the phase error during acquisition. Therefore, through-plane dephasing was the dominant cause of signal loss.

We subsequently attempted to recover the lost signals with a 3DTRF pulse. We scanned the phantom for field map and designed a 3DTRF pulse, as described above. The sinc pulse in the GRE sequence was replaced by the 3DTRF pulse, with the same imaging parameters. The image acquired with the 3DTRF pulse was compared with that acquired using the sinc pulse.

In a separate scan, with metal still attached and shim values unchanged, the slice volume excited by the 3DTRF pulse was imaged using a 3D SE stack-of-spirals sequence.

The sequence was identical to the 2D GRE sequence with 3DTRF pulse, except for an additional 180° pulse midway between the end of 3DTRF pulse and start of the spiral acquisition, a z gradient blip for phase-encoding (Fig. 4.6), and a shorter T_R (300 ms). The 180° pulse rewound the off-resonance-induced phase evolution, so that the magnetization pattern at the beginning of acquisition would be identical to that at the end of the 3DTRF pulse. In the experiment, the z gradient blip provided a 4-cm FOV in z, with 1-mm resolution. The 180° pulse selectively excited a 4 cm slab centered at the iso-center. 3D image of the slice volume was reconstructed from the 2D spiral images via inverse FFT along the phase-encoded z dimension.
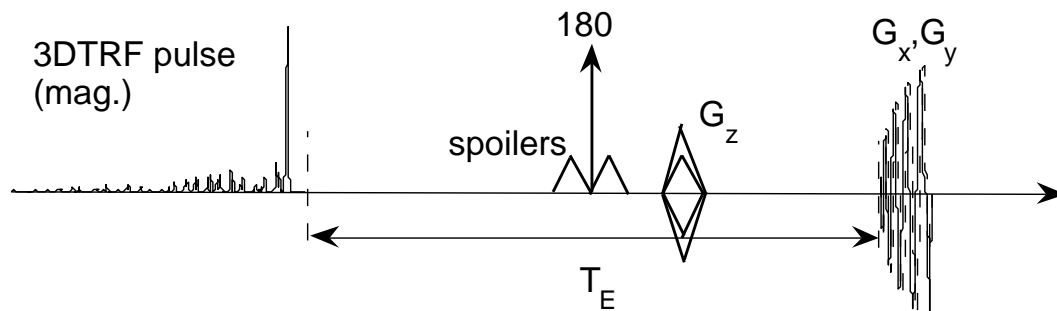
Figure 4.6: Spin-echo, stack-of-spirals sequence used to image the slice volume excited by the 3DTRF pulse.

Fig. 4.7a shows estimated field maps interpolated to the desired pattern grid, for nine 1-mm subslices around the iso-center ($z = 0$). The maps revealed global main field inhomogeneity, while the anterior phantom region, superior to the metal attachment, exhibited significant frequency offsets (white "hot spot"). Map of the z-direction field gradient (Fig. 4.8a) was estimated via linear regression of the through-plane field variation. At the hot spot, the gradient was around -15×10^{-2} mT/m, a typical value measured in the ventral brain at 3 T.

The desired phase pattern (Fig. 4.7b, only the central nine subslices are shown) was
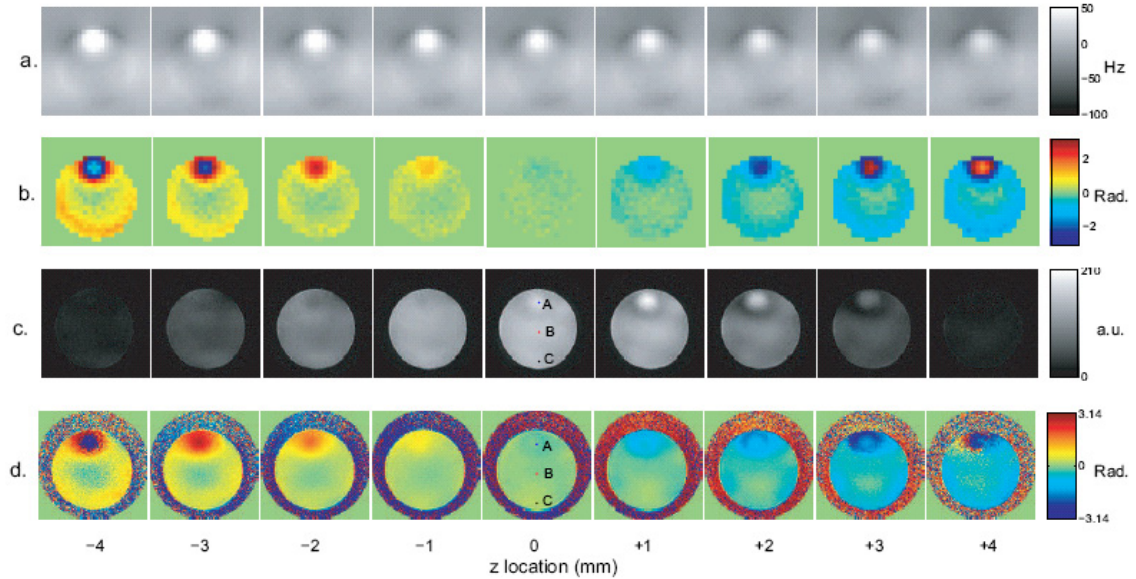
Figure 4.7: a: Field maps on 1 mm subslices around the iso-center, revealing a "hot spot" of off resonance at the anterior phantom region (white). b: Desired phase pattern. c,d: Slice volume excited by the 3DTRF pulse, as imaged by the 3D sequence. The images provided evidence for fidelity of the slice-selective magnitude profile, and good match between the desired and achieved phase pattern. Slice profiles at locations A-C are plotted in Fig. 4.9. (a.u.: arbitrary units)

subsequently derived from the differential field map and T_E. It contained rapid, approximately linear through-plane phase variation at the hot spot, and minimal phase variation near the phantom center. Note that the pattern shown in Fig. 4.7b was masked by ROI's covering only the phantom. Finally the complex desired pattern was formed by embedding that phase pattern in a Gaussian profile with FWHM = 5 mm. Together with the field map, the desired pattern gave rise to 15.4-ms gradient waveforms (Fig. 4.2a) that produced the EV trajectory in Fig. 4.1. A complex RF pulse (Fig. 4.2b,c) was computed with CG in 257 seconds.

With the sinc pulse, signal loss was observed at the hot spot (Fig. 4.8b), predominantly caused by the through-plane field gradient (Fig. 4.8a). In contrast, the 3DTRF pulse excited the slice with signal recovered at the hot spot, while SNR at the remaining phantom regions was undiminished (Fig. 4.8c). Images of the slice volume, as captured by the
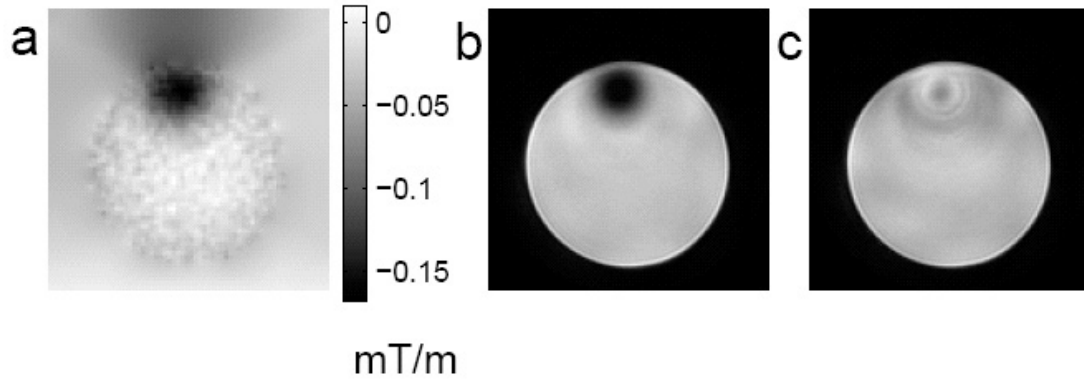
Figure 4.8: a: Through-plane field gradient map at the iso-center, estimated from linear regression on field maps of phantom subslices. b: GRE image plagued by signal loss. c: GRE image with signal recovery using a 3DTRF pulse.
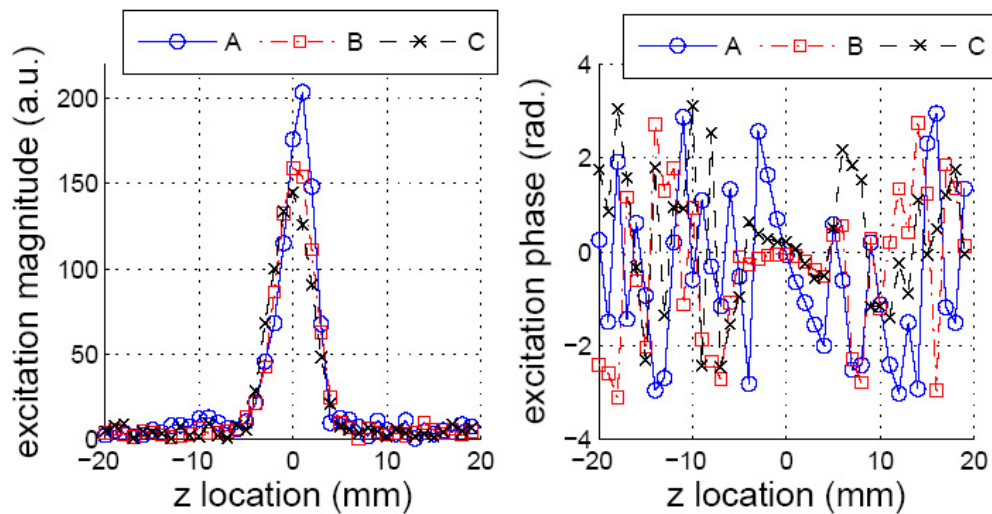
Figure 4.9: Magnitude and phase of slice profiles at locations A-C in Fig. 4.7. (a.u.: arbitrary units)

3D sequence (Fig. 4.7c (magnitude), and d (phase)), indicated that the 3DTRF pulse indeed excited a 3D precompensatory phase pattern as intended. The imaged phase pattern (Fig. 4.7d) matched the desired one closely. The desired phase variation at the hot spot was achieved, whereas the phase through the phantom center remained coherent. Additionally, in the magnitude image of the slice volume, no excitation beyond the slice profile

at iso-center was observed (not shown). The magnitude profile appeared centered and approximately Gaussian. Fig. 4.9 shows the magnitude and phase profiles at three different in-plane locations (A-C), confirming fidelity of the excited slice volume. One can observe, from the phantom images and profiles, that SNR uniformity was slightly compromised with the 3DTRF pulse. Non-uniformity occured particularly at regions with rapid in-plane transition in field map and desired phase. Nevertheless, slight SNR non-uniformity could generally be tolerated in fMRI.

4.7.2   Signal recovery in vivo

The goal of the human experiment was to show that the 3DTRF method was effective in the human head, in which the field variations were more complex than in the homogeneous phantom. For both the sinc and 3DTRF pulses, the same GRE sequence as in the phantom experiment was used, except that only two spiral interleaves were used for image acquisition. The field map acquisition and 3DTRF pulse design were as described previously for the phantom experiment. Brain images obtained with the 3DTRF pulses were compared to those with sinc pulses.

The structural brain image obtained at iso-center with a spoiled gradient recall (SPGR) sequence (Fig. 4.10a) contained structures (for example, thalamus and closing of the lateral ventricles) that indicated an inferior brain slice location. With sinc pulse excitation, the GRE image at the same location was plagued by signal loss (Fig. 4.10c). Signals from the inferior frontal cortex (IFC) were almost completely lost. Through-plane linear regression on the field maps of subslices resulted in a gradient map as shown in Fig. 4.10b, in which the regions of high gradient magnitudes were consistent with regions of signal loss. Fig. 4.10d shows the image acquired using a 3DTRF pulse, computed in 260 seconds. Signals from the IFC was significantly recovered, while those from other brain regions

remained mostly unaffected.
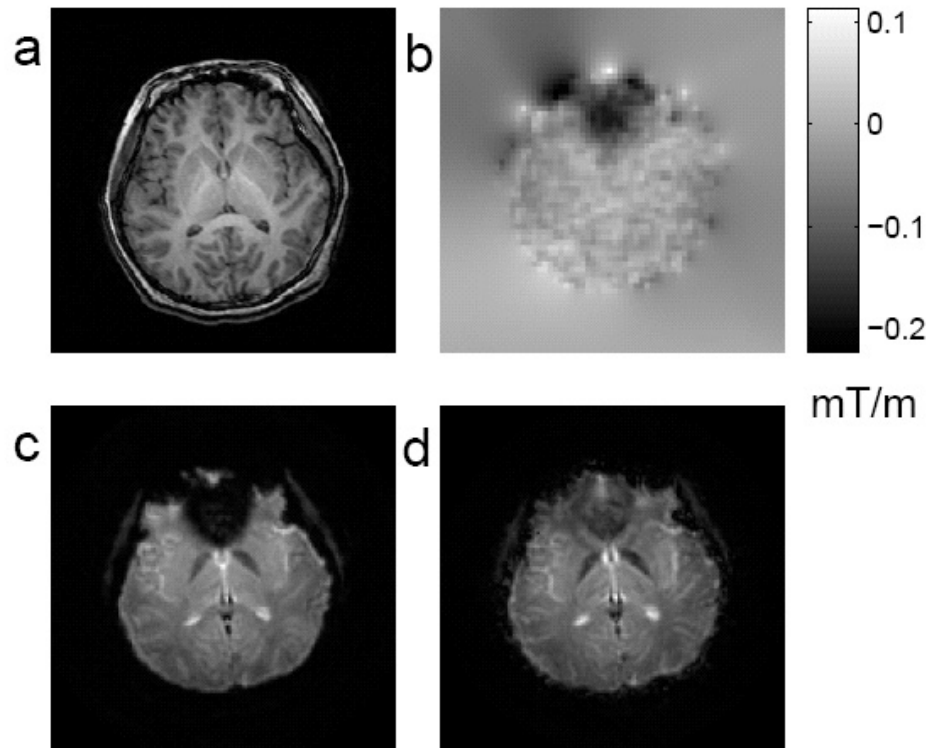
Figure 4.10: a: SPGR image of an inferior brain slice. b: Through-plane field gradient map of the slice. c: GRE image plagued by signal loss. c: GRE image with signal recovery using a 3DTRF pulse.

4.8 Discussion

Several important advances have been introduced to the original 3DTRF method reported in [46]. We have introduced the new EV trajectory that enables accurate and fine slice selection. It avoids excitation sidelobes [46], and therefore obviates complimentary techniques for sidelobe removal, such as the asymmetric spin echo (ASE) method [104]. The EV trajectory, which is adaptive to the desired excitation pattern, is also efficient in sampling the desired pattern's spectrum in k-space, significantly reducing pulse length. We also adopt the iterative pulse design method, which allows frequency offset compensation for enhanced excitation accuracy. The pulse design process is greatly accelerated by

the segmentation framework from the image reconstruction literature [15–17,98,99]. With orchestration of all the new components, successful signal recovery was demonstrated in a relatively thin (5 mm) slice in both phantom and inferior brain, using 3DTRF pulses that were only 15.4 ms long. Note that for the same slice thickness, the original design approach would require either very long pulses (> 100 ms) [46] or multi-shot excitation [75]. In our phantom experiment, we also showed good fidelity in the magnitude and phase of the excited slice volume, even in regions where the field was inhomogeneous.

4.8.1 Temporal resolution and SNR advantages

The advances represent a major step toward a fully effective 3DTRF method for routine fMRI studies in loss-plagued brain regions. Indeed, the method is attractive compared to other popular methods such as z-shimming [24] and thin slice acquisition [23], in terms of temporal resolution and SNR of the fMRI time series.

To see the advantage in fMRI temporal resolution, consider a time series acquired using a single-interleave 2D GRE sequence, covering a specified FOV in z with N slices. Relative to the baseline case with sinc pulse for slice selection, the 3DTRF method demands that the minimum sampling interval in the time series (ΔT_{min}) increases by $N \cdot s$, where s is the extra time needed for deploying a 3DTRF pulse in lieu of the sinc pulse. In contrast, for the same z coverage, n-step z-shimming or n-time slice thickness reduction results in an increase of ΔT_{min} by a *factor* of n. Therefore, given that s is short (12.2 ms in our experiments), the temporal resolution cost of the 3DTRF method can be much lower than that of z-shimming or slice thickness reduction.

The method also has a relative SNR advantage. Relative to the baseline SNR for a given slice thickness attainable in a loss-free brain region, a composite image formed from combining n subimages of $\Delta z/n$-thick slices has its SNR reduced by a factor of $\sqrt{n}$. A

composite image formed from n z-shimming steps also has a lower average SNR, by a factor depending on the number of z-shimming steps and the step size. With the 3DTRF method, the baseline SNR can be preserved at image regions not plagued by signal loss, whereas SNR at loss-plagued regions can be comparable, provided that signal recovery there is nearly complete. However, SNR uniformity across image can be affected slightly, even at regions that are originally not plagued by signal loss (see Fig. 4.8).

4.8.2 Limitations

The currently proposed 3DTRF method is effective in signal recovery under two conditions. First, the target phase pattern has to be smooth in the in-plane dimensions because of the scarcity of phase-encoding locations. Recovery efficacy is limited when there are multiple regions of signal loss (for example, on a slice with loss caused by *both* the air-filled middle ears and sinuses). One might be tempted to add phase-encoding locations to pursue the necessary in-plane excitation variability. Unfortunately, additional phase-encoding, implemented via extra pulse segments appended to the beginning of the original pulse, becomes increasingly marred by the off-resonance dephasing up to the pulse end. As a result, the addition become less and less "usable" by CG in approximating the desired pattern. This "phase-encoding ceiling" exists even though the dephasing is modeled in the design and accounted for. The ceiling poses a limit on the in-plane variability that a 3DTRF pulse can possibly render.

Note that the dephasing that causes the ceiling is proportional to both the phase accumulation time and frequency offset magnitude. Large frequency offsets impose low phase-encoding ceilings, potentially leading to insufficient in-plane encoding for successful recovery. Therefore, the second critical condition for successful recovery is that the magnitude of frequency offsets is not too large (below 75 Hz at 3 T). Large frequency off-

sets are devastating to the in-plane excitation accuracy, though the effect in the z direction is minimal.

Strategies to break through the phase-encoding ceiling will enable signal recovery at multiple image regions, in the presence of large frequency offsets. Any prospective approach to the 3DTRF method must provide encoding capability that is less vulnerable to dephasing. Toward this goal, parallel excitation can potentially be beneficial. Alternatively, successful signal recovery with the current design approach can be accomplished over the entire brain, if frequency offsets are somehow reduced. The localized intraoral and external shimming methods [39–41] were demonstrated to be effective in improving overall field homogeneity. The 3DTRF method, if applied in concert with those shimming techniques, could potentially provide the intricate corrections that gross localized shimming fails to do.

CHAPTER 5

Joint design of trajectory and RF pulse

This chapter is based on materials from Ref. [105].

5.1   Why joint design?

Recall that in the advanced 3DTRF method, the phase encoding locations in k_x-k_y plane are *predetermined* based on the DFT of the desired pattern, after which the RF pulse is iteratively designed. The choices are confined to the discrete spatial frequency locations at which the DFT is defined. An interesting question is: instead of choosing from discrete locations, would choosing the encoding locations from the *entire* continuous k_x-k_y plane be advantageous, in terms of excitation accuracy and pulse power management? If so, how can those locations be determined? Because the design cost function (Eq. 4.4) is not separably dependent on the encoding locations and RF pulse, it is inadequate to optimize the encoding locations and RF pulse in separate steps. It motivates a new design process that *jointly* optimizes the encoding locations and RF pulse.

In fact, this problem is encountered in the general pulse design for single-coil and parallel excitation. In the common pulse design methods, one predetermines the gradient waveform (hence, k-space trajectory), and subsequently designs the corresponding RF pulses for a given desired excitation pattern. Such trajectory predetermination is indeed unnecessarily restrictive, because the desired pattern is known completely prior to design,

unlike the analogous data acquisition process in which the object (and its spectrum) is unknown a priori. It is likely that by jointly designing the trajectory and RF pulses, we might be able to exploit the design freedom to a fuller extent. The extra freedom could be channeled towards excitation accuracy improvement and/or pulse power reduction. Such benefits may be particularly significant in parallel excitation at high speedup factors, when the design problem becomes increasingly ill-posed, and "a proper interplay between the coil sensitivity profiles and the involved trajectories has to be found." [106].

There are surprisingly few studies on joint trajectory and pulse design in the literature. Hardy et al. [85] jointly optimized the gradient and RF waveforms for 2D single-coil selective excitation. They expressed both the gradient and RF waveforms as Fourier series, and applied simulated annealing to seek the Fourier coefficients that globally minimized the excitation error. For designing single-coil large-tip-angle pulses, Levin et al. [107] approximated the spiral trajectory by concentric circles and jointly optimized their radii together with the RF pulse.

In this chapter, we will explore a new framework of joint trajectory and pulse design, suitable for the 3DTRF method and general pulse design for single-coil or parallel excitation. We propose that the joint design can be implemented as an *alternating* optimization process of trajectory parameters and RF pulses. In each iteration, the pulse optimization problem is solved using CG, followed by a simple update of the trajectory parameters using gradient descent (GD). The cost function gradient, with respect to the trajectory parameters, can be computed efficiently using an analytical formula. This design process is efficient and produces trajectory and RF pulses that minimize the cost function *locally*. By Bloch equation simulation, We will explore the benefits of applying the joint design concept to parallel excitation and the single-coiled 3DTRF method. It turns out that for parallel excitation, joint designs can excite target patterns with significantly im-

proved accuracy and/or reduced total integrated pulse power, compared to designs with predetermined trajectories. However, for the 3DTRF method, jointly designing the pulse and phase-encoding locations only improve excitation accuracy marginally. The benefit was insufficient to break through the limitations that we encountered in our 3DTRF experiments.

5.2 Alternating optimization

The joint design framework is an extension of the iterative pulse design method in Chapter 3. Consider the general case of pulse design for R-coil, small-tip-angle spatially selective excitation in 2D, without loss of generality. When $R = 1$, it corresponds to the single-coil design problem which the 3DTRF method involves. Let $\mathbf{b}_r = (b_r(t_0), \ldots, b_r(t_{N-1}))^T$ be complex RF pulse samples for the rth coil, $r = 1, \ldots, R$, and $\mathbf{k}_x(\boldsymbol{\phi}_x) = (k_x(t_0; \boldsymbol{\phi}_x), \ldots, k_x(t_{N-1}; \boldsymbol{\phi}_x))^T$, $\mathbf{k}_y(\boldsymbol{\phi}_y) = (k_y(t_0; \boldsymbol{\phi}_y), \ldots, k_y(t_{N-1}; \boldsymbol{\phi}_y))^T$ be the excitation k-space trajectory parameterized by $\boldsymbol{\phi}_x = (\phi_{x1}, \ldots, \phi_{xL})^T$, $\boldsymbol{\phi}_y = (\phi_{y1}, \ldots, \phi_{yL})^T$, respectively. Let $\mathbf{A}(\mathbf{k}_x(\boldsymbol{\phi}_x), \mathbf{k}_y(\boldsymbol{\phi}_y))$ be the pulse design system matrix as a function of the trajectory samples, and $\mathbf{S}_r = \text{diag}\{s_r(\mathbf{x}_0), \ldots, s_r(\mathbf{x}_{M-1})\}$ be sensitivity pattern samples of the rth coil. The trajectory and RF pulses can be jointly designed via solving the following minimization problem:

$$(5.1) \qquad (\hat{\boldsymbol{\phi}}_x, \hat{\boldsymbol{\phi}}_y, \hat{\mathbf{b}}_1, \ldots, \hat{\mathbf{b}}_R) = \underset{\boldsymbol{\phi}_x, \boldsymbol{\phi}_y, \mathbf{b}_1, \ldots, \mathbf{b}_R}{\arg\min} \Psi(\boldsymbol{\phi}_x, \boldsymbol{\phi}_y, \mathbf{b}_1, \ldots, \mathbf{b}_R)$$

where the cost function, Ψ, comprises total weighted squared excitation error and total integrated pulse power terms:

$$\Psi(\boldsymbol{\phi}_x, \boldsymbol{\phi}_y, \mathbf{b}_1, \ldots, \mathbf{b}_R) =$$

$$(5.2) \qquad \left\| \mathbf{d} - \sum_{r=1}^{R} \mathbf{S}_r \mathbf{A}(\mathbf{k}_x(\boldsymbol{\phi}_x), \mathbf{k}_y(\boldsymbol{\phi}_y)) \mathbf{b}_r \right\|_{\mathbf{W}}^2 + \beta \sum_{r=1}^{R} \|\mathbf{b}_r\|^2$$

With Eq. 5.1, one seeks the trajectory parameters and RF pulses that produce an excitation pattern close to the desired pattern, $\mathbf{d} = (d(\mathbf{x}_0), \ldots, d(\mathbf{x}_{M-1}))^T$, with the secondary objective of reducing the total integrated power. These two objectives are balanced by regularization parameter β. Note that other regularization terms can be devised to control peak power and trajectory smoothness. $\mathbf{W}$ is a diagonal matrix containing error weights for defining ROI.

Eq. 5.1 can be implemented as the following *alternating* minimization process:

for $n = 0 : N_{alt} - 1$

$$(5.3) \qquad (\hat{\boldsymbol{\phi}}_x^{(n+1)}, \hat{\boldsymbol{\phi}}_y^{(n+1)}) = \begin{cases} (\hat{\boldsymbol{\phi}}_x^{(0)}, \hat{\boldsymbol{\phi}}_y^{(0)}) & \text{if } n = 0, \\ \arg\min_{\boldsymbol{\phi}_x, \boldsymbol{\phi}_y} \Psi(\boldsymbol{\phi}_x, \boldsymbol{\phi}_y, \hat{\mathbf{b}}_1^{(n)}, \ldots, \hat{\mathbf{b}}_R^{(n)}) & \text{if } n \neq 0, \end{cases}$$

$$(5.4) \quad (\hat{\mathbf{b}}_1^{(n+1)}, \ldots, \hat{\mathbf{b}}_R^{(n+1)}) = \arg\min_{\mathbf{b}_1, \ldots, \mathbf{b}_R} \Psi(\hat{\boldsymbol{\phi}}_x^{(n+1)}, \hat{\boldsymbol{\phi}}_y^{(n+1)}, \mathbf{b}_1, \ldots, \mathbf{b}_R)$$

end

In words, by fixing the RF pulses from the nth iteration, we obtain the $(n+1)$th updated trajectory parameters via Eq. 5.3; and subsequently by fixing the $(n+1)$th trajectory parameters, we design the $(n+1)$th optimal RF pulses via Eq. 5.4. This alternating minimization process is initialized with $(\hat{\boldsymbol{\phi}}_x^{(0)}, \hat{\boldsymbol{\phi}}_y^{(0)})$ and continues until $n = N_{alt} - 1$. The final trajectory and RF pulses, $(\mathbf{k}_x(\hat{\boldsymbol{\phi}}_x^{(N_{alt})}), \mathbf{k}_y(\hat{\boldsymbol{\phi}}_y^{(N_{alt})}))$ and $(\hat{\mathbf{b}}_1^{(N_{alt})}, \ldots, \hat{\mathbf{b}}_R^{(N_{alt})})$, are to be deployed on a parallel excitation system.

Both of the RF and trajectory optimization problems are constrained. The integrated and peak power constraints on the pulses can be handled via regularization [94]. On the other hand, when computing $(\hat{\boldsymbol{\phi}}_x^{(n+1)}, \hat{\boldsymbol{\phi}}_y^{(n+1)})$ via Eq. 5.3, we must ensure that the resulting trajectory satisfies the peak gradient amplitude and slew rate limits. Thus, Eq. 5.3 is

constrained by

$$|D_1\mathbf{k}_x(\boldsymbol{\phi}_x)| \leqslant G_{max}, \qquad |D_2\mathbf{k}_x(\boldsymbol{\phi}_x)| \leqslant S_{max},$$

(5.5) $$|D_1\mathbf{k}_y(\boldsymbol{\phi}_y)| \leqslant G_{max}, \qquad |D_2\mathbf{k}_y(\boldsymbol{\phi}_y)| \leqslant S_{max},$$

where D_1 and D_2 are first and second order time-derivative operators, and G_{max}, S_{max} are the peak gradient amplitude and slew rate, respectively. These constraints can be handled with special strategies of trajectory parameterization that will be discussed in the following section.

The pulse design problem (Eq. 5.4) can be solved efficiently using CG ; whereas the trajectory optimization (Eq. 5.3) is a much more difficult nonlinear minimization problem, with many local minima in its cost function. It is possible to find its *global* minima using simulated annealing [85] or direct search methods such as Nelder-Mead [108]. However, the computational cost of these algorithms is very high, rendering them unsuitable for the online joint design problem in which Eq. 5.3 has to be solved repetitively.

We can, instead, solve Eq. 5.3 by applying the GD algorithm, and running it for a small number of iterations, possibly just one:

$$\hat{\boldsymbol{\phi}}_x^{(n+1)} = \hat{\boldsymbol{\phi}}_x^{(n)} - \alpha \nabla_{\boldsymbol{\phi}_x} \Psi(\boldsymbol{\phi}_x, \boldsymbol{\phi}_y, \hat{\mathbf{b}}^{(n)}) \Big|_{(\hat{\boldsymbol{\phi}}_x^{(n)}\hat{\boldsymbol{\phi}}_y^{(n)})},$$

(5.6) $$\hat{\boldsymbol{\phi}}_y^{(n+1)} = \hat{\boldsymbol{\phi}}_y^{(n)} - \alpha \nabla_{\boldsymbol{\phi}_y} \Psi(\boldsymbol{\phi}_x, \boldsymbol{\phi}_y, \hat{\mathbf{b}}^{(n)}) \Big|_{(\hat{\boldsymbol{\phi}}_x^{(n)}\hat{\boldsymbol{\phi}}_y^{(n)})},$$

where $\nabla_{\boldsymbol{\phi}_x} \Psi, \nabla_{\boldsymbol{\phi}_y} \Psi$ denote gradients of the cost function with respect to $\boldsymbol{\phi}_x, \boldsymbol{\phi}_y$, and α is a scaling factor on the update step. This CG-GD implementation of joint design leads to a set of *locally* optimal trajectory parameters and RF pulses, that potentially excites with higher accuracy and lower pulse power than a conventional design. Note that it is important to initialize the joint design with a good trajectory to avoid convergence to an undesirable local minima.

5.3   Trajectory parameterization

We can reduce the dimension of the trajectory optimization problem via trajectory parameterization, provided that the number of parameters (L) is smaller than the number of trajectory samples (N). Also, using smooth basis functions may help enforcing the trajectory smoothness constraints (Eq. 5.5). However, the obvious drawback is that our search is limited to a subspace of the original space of all implementable trajectories.

One parameterization strategy is to express k_x and/or k_y in terms of time-shifted basis functions, and regard the basis coefficients as parameters:

$$k_x(t_j; \boldsymbol{\phi}_x) = \sum_{l=0}^{L-1} \phi_{xl} h_x(t_j - l\Delta t), \qquad \text{and/or}$$

$$(5.7) \qquad k_y(t_j; \boldsymbol{\phi}_y) = \sum_{l=0}^{L-1} \phi_{yl} h_y(t_j - l\Delta t).$$

Here, $h_x(t), h_y(t)$ are basis functions and Δt is a time shift. In matrix form,

$$\mathbf{k}_x(\boldsymbol{\phi}_x) = \mathbf{H}_x \boldsymbol{\phi}_x, \qquad \text{and/or}$$

$$(5.8) \qquad \mathbf{k}_y(\boldsymbol{\phi}_y) = \mathbf{H}_y \boldsymbol{\phi}_y,$$

where $\mathbf{H}_x, \mathbf{H}_y$ are matrices whose columns are the time-shifted basis samples. By invoking the chain rule, we can easily relate the cost function gradients with respect to the parameters to that with respect to the trajectory samples:

$$\nabla_{\boldsymbol{\phi}_x} \Psi = \mathbf{H}'_x \nabla_{\mathbf{k}_x} \Psi, \qquad \text{and/or}$$

$$(5.9) \qquad \nabla_{\boldsymbol{\phi}_y} \Psi = \mathbf{H}'_y \nabla_{\mathbf{k}_y} \Psi.$$

Now, to obtain the trajectory update direction in the GD step, all we need are expressions for the gradients with respect to the trajectory samples.

5.4 Deriving the cost function gradients

Because of the special form of system matrix $\mathbf{A}$, the cost function gradients, with respect to $\mathbf{k}_x$ and $\mathbf{k}_y$, can be derived algebraically. Let us define length-M error vector $\mathbf{e} = \mathbf{d} - \sum_{r=1}^{R} \mathbf{S}_r \mathbf{A}(\mathbf{k}_x(\boldsymbol{\phi}_x), \mathbf{k}_y(\boldsymbol{\phi}_y)) \mathbf{b}_r$, and length-$N$ temporal vector

$$
\begin{aligned}
\mathbf{p}_x &= \nabla_{\mathbf{k}_x} \Psi \\
&= \nabla_{\mathbf{k}_x} \|\mathbf{e}\|_{\mathbf{W}}^2 .
\end{aligned}
$$
(5.10)

The jth element of $\mathbf{p}_x$ is

$$
p_{xj} = 2 Re\{\mathbf{e}' \mathbf{W} \mathbf{q}_{xj}\},
$$
(5.11)

where $\mathbf{q}_{xj} = \frac{d}{dk_{xj}} \mathbf{e}$ is the derivative of $\mathbf{e}$ with respect to $k_x(t_j)$. The ith element of $\mathbf{q}_{xj}$ is given by

$$
\begin{aligned}
q_{xj,i} &= -\frac{d}{dk_{xj}} \left[\sum_{r=1}^{R} s_r(\mathbf{x}_i) \cdot \sum_{j=0}^{N-1} \exp(\imath k_{xj} x_i + \imath k_{yj} y_i) \, b_j \right] \\
&= -\sum_{r=1}^{R} s_r(\mathbf{x}_i) \cdot \imath x_i \cdot \exp(\imath k_{xj} x_i + \imath k_{yj} y_i) \, b_j .
\end{aligned}
$$
(5.12)

Thus,

$$
\mathbf{q}_{xj} = -\sum_{r=1}^{R} \imath \mathbf{S}_r \mathbf{X} \mathbf{a}_j b_{jr},
$$
(5.13)

where $\mathbf{X} = \operatorname{diag}\{x_0, \ldots, x_{M-1}\}$. Substituting Eq. 5.13 into Eq. 5.11 yields

$$
\begin{aligned}
p_{xj} &= 2 Re\{-\imath \mathbf{e}' \mathbf{W} \sum_{r=1}^{R} \mathbf{S}_r \mathbf{X} \mathbf{a}_j b_{jr}\} \\
&= 2 Re\{\imath \sum_{r=1}^{R} b'_{jr} \mathbf{a}'_j \mathbf{X} \mathbf{S}'_r \mathbf{W} \mathbf{e}\} .
\end{aligned}
$$
(5.14)

If we columnize p_{xj}, $j = 0, \ldots, N-1$, we obtain:

$$
\nabla_{\mathbf{k}_x} \Psi = 2 Re\{\imath \sum_{r=1}^{R} \operatorname{diag}\{\mathbf{b}'_r\} \, \mathbf{A}' \mathbf{X} \mathbf{S}'_r \mathbf{W} \mathbf{e}\},
$$
(5.15)

and defining $\mathbf{Y} = \text{diag}\{y_0, \ldots, y_{M-1}\}$:

(5.16) $$\nabla_{\mathbf{k}_y} \Psi \;=\; 2Re\{\imath \sum_{r=1}^{R} \text{diag}\{\mathbf{b}_r'\}\, \mathbf{A}'\mathbf{Y}\mathbf{S}_r'\mathbf{W}\mathbf{e}\}.$$

These two expressions provide a fast means of computing the trajectory updates in the joint design process.

5.5 Application to echo-planar pulses for parallel excitation

Echo-planar (EP) RF pulses have been used widely in parallel excitation [66, 109]. Analogous to EP imaging, those pulses are designed with EP trajectories in excitation k-space that "frequency-encode" in one spatial dimension and "phase-encode" in the other. Accelerated EP trajectories under-sample the phase-encode dimension (k_y), and the resulting aliased excitation is resolved by the blurring effect of the Fourier transforms of the sensitivity patterns in k-space (due to the convolution process [65]), which leads to deposition of RF energy in between the phase-encoding lines.

An interesting question is whether non-uniform phase-encoding locations would be superior to uniform ones as used in [66, 109], in terms of excitation accuracy and total integrated pulse power. In fact, it has been shown that non-uniform encoding in EP parallel imaging improves image quality [110]. If non-uniform phase-encoding were indeed favorable in excitation, the optimal encoding locations would depend on the desired excitation pattern and sensitivity patterns specific to the experiment. The proposed joint design approach can be used to compute locally optimal phase-encoding locations and RF pulses.

Consider joint design with an EP trajectory, $\mathbf{k}(t_j) = (k_x(t_j), k_y(t_j))$, $j = 0 \ldots N-1$, for R-coil parallel excitation. One way to parameterize the trajectory is to approximate $k_y(t_j)$ as a sum of time-shifted rectangular (rect) functions, and leave $k_x(t_j)$ unparameterized. Let $\boldsymbol{\phi}_y = (\phi_{y0}, \ldots, \phi_{y(L-1)})^T$ be phase-encoding locations, T_{PE} be the duration of one phase-encoding line, and define rect function $h(t) = 1$ for $t \in [0, T_{\text{PE}}]$, and 0

otherwise. We can parameterize $k_y(t_j)$ by ϕ_y via

$$(5.17) \qquad k_y(t_j; \phi_y) \quad \approx \quad \sum_{l=0}^{L-1} \phi_{yl} h(t_j - lT_{\text{PE}}),$$

or in matrix-vector form, $\mathbf{k}_y(\phi_y) \approx \mathbf{H}\phi_y$, where $\mathbf{H}$ is a matrix whose columns contain samples of time-shifted rect functions. Provided that the y gradient blips underlying the phase-encoding are within the peak gradient and slew rate limits, this parameterization ensures that the constraints (Eq. 5.5) are satisfied, resulting in a virtually constraint-free joint design. Now, one is ready to jointly design ϕ_y and $\mathbf{b}_r, r = 1, \ldots, R$.

5.5.1 Simulation setup

We implemented the joint design of phase-encoding locations and EP pulses for a four-coil ($R = 4$) parallel excitation scenario, and compared it to a conventional design [94] using predetermined trajectory. EP trajectories with uniform phase-encoding were used to initialize the joint design, and as the predetermined trajectories for the conventional design. By 2D Bloch simulation (FOV = 24 cm $\times$ 24 cm, matrix size = 64 $\times$ 64), we investigated the benefits of optimizing phase-encoding locations in the joint design, in terms of excitation accuracy and total integrated power. All pulse designs and simulations were performed with Matlab R2006a (Mathworks, Natick, MA, USA) on a 3.4 GHz Pentium workstation with 2 GB memory. The uniform EP trajectories, used for joint design initialization and conventional design, under-sampled in the k_y dimension. They supported 1-cm excitation resolution in both x and y. We varied their phase-encode spacing, which was inversely proportional to y-direction excitation FOV (XFOV) ranging from 4 to 12 cm. It corresponded to a range of *speedup factors*, as defined in [94], from 6 down to 2. We compared the design methods at each speedup factor, anticipating that the joint design would be particularly beneficial in some particular range. All EP trajectories were produced by x, y gradient blips that complied with the peak gradient and slew rate constraints, which
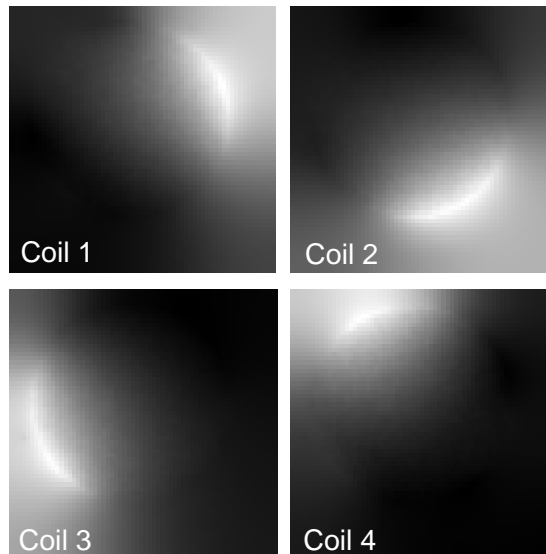
Figure 5.1: Smoothed sensitivity patterns (magnitude, in a.u.) used in pulse designs and Bloch simulations.

were 4 G/cm and 15000 G/cm/s, respectively. Sampling period was 4 μs. We compared the design methods for two desired excitation patterns. The first one was a 10 cm $\times$ 5 cm "horizontal block" of uniform 15-degree tip angle and zero phase, defined in a 24 cm $\times$ 24 cm FOV with matrix size of 64 $\times$ 64. The second pattern was a "vertical block" obtained by rotating the horizontal block by 90 degrees. Four out of eight of the complex receive sensitivity patterns (Fig. 5.1) of a head coil array (Intermagnetics, Latham, NY, USA) were acquired as described in Ref. [94], and treated as transmit sensitivity patterns in both pulse designs and Bloch simulations. Relative weight of excitation error to pulse power in the cost function was matched for the conventional and joint designs ($\beta = 4000$). The ROI was derived via thresholding the body-coil phantom image (acquired for sensitivity map estimation). Off resonance effects were ignored in the pulse designs. In each alternation of the joint design, we ran 5 CG iterations for pulse design (Eq. 5.4) and 1 GD

trajectory parameter update (Eq. 5.3), until convergence was reached (when current cost function value in CG was 99.9% of the previous one). We used the same convergence criterion for halting the conventional design. Each joint-design CG process was initialized by the pulse designed in the previous alternation (except in the first alternation, CG was initialized with a zero pulse). The scaling factor on the GD step was set small enough to ensure convergence ($\alpha = 5.2 \times 10^{-4}$).

5.5.2 Results

Fig. 5.2 compares the joint and conventional design methods, at different speedup factors, in terms of (a) normalized root-mean-square error (NRMSE) of the Bloch-simulated excitation pattern; (b) total integrated pulse power of all channels; (c) cost function (Eq. 5.2) value when the methods reach convergence; and (d) computational time for the methods to reach convergence.

For the horizontal block desired excitation pattern (black solid lines), the joint design outperformed the conventional design in a range of high speedup factors – the jointly designed pulses achieved higher excitation accuracy and their total integrated power was lower (Fig. 5.2a,b). Fig. 5.3 shows Bloch-simulated excitation patterns (magnitude) of the designs, at XFOV = 5 cm to 8 cm. The performance advantages diminished at low speedup factors. The superiority of the joint design at high speedup factors could be attributed to the lower cost function values that it attained (Fig. 5.2c), at the cost of increased computational time (Fig. 5.2d). Fig. 5.4a shows the uniform EP trajectory (at XFOV = 6 cm) used in the conventional method (and for initializing the joint design), and the non-uniform one that the joint design converged to. The joint design evidently adjusted the phase-encoding locations so that the central region of the desired excitation pattern spectrum (Fig. 5.4, underlying) became better sampled, leading to the observed excitation accuracy
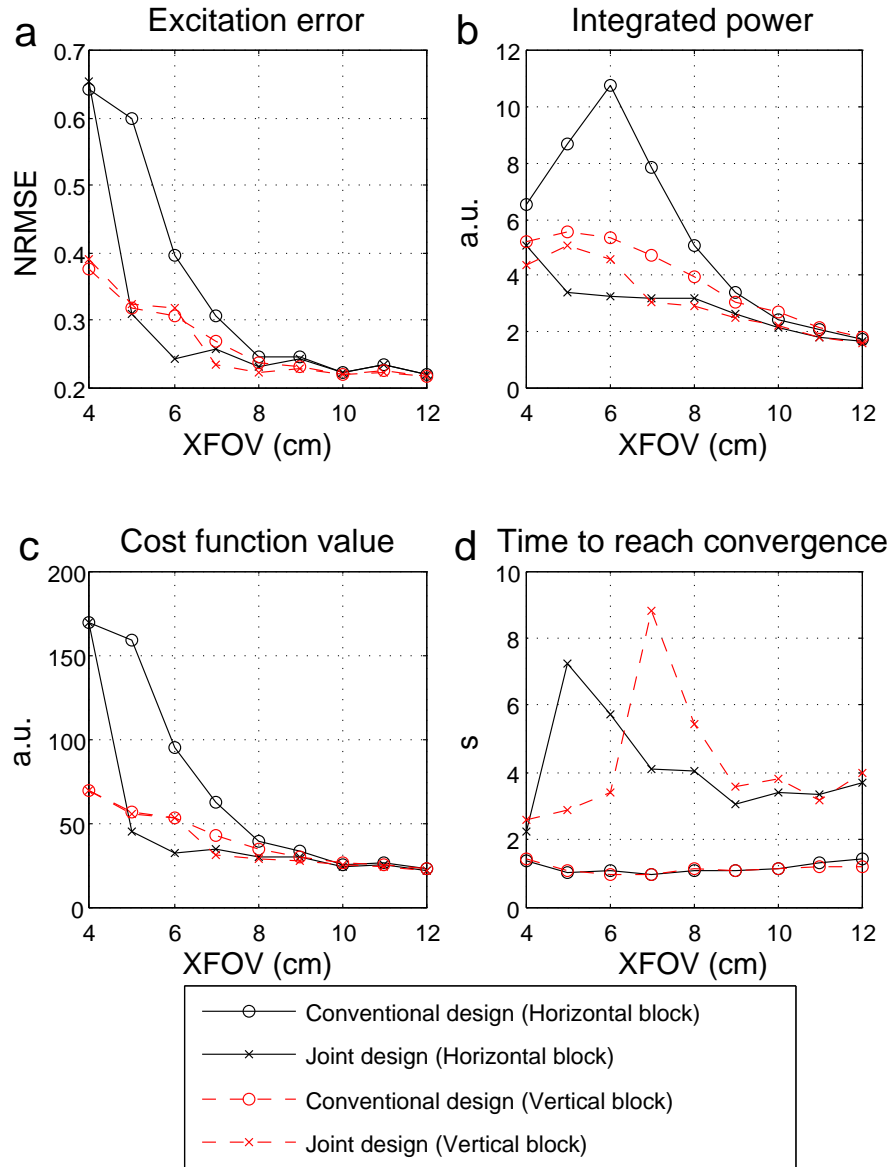
Figure 5.2: Based on Bloch simulations, performance of the joint and conventional design methods are compared at different speedup factors. With cost in computational time, joint designs are often advantageous over the conventional designs, in terms of excitation accuracy and total integrated pulse power. This cost-benefit tradeoff is dependent on the choice of desired excitation pattern (in parentheses).
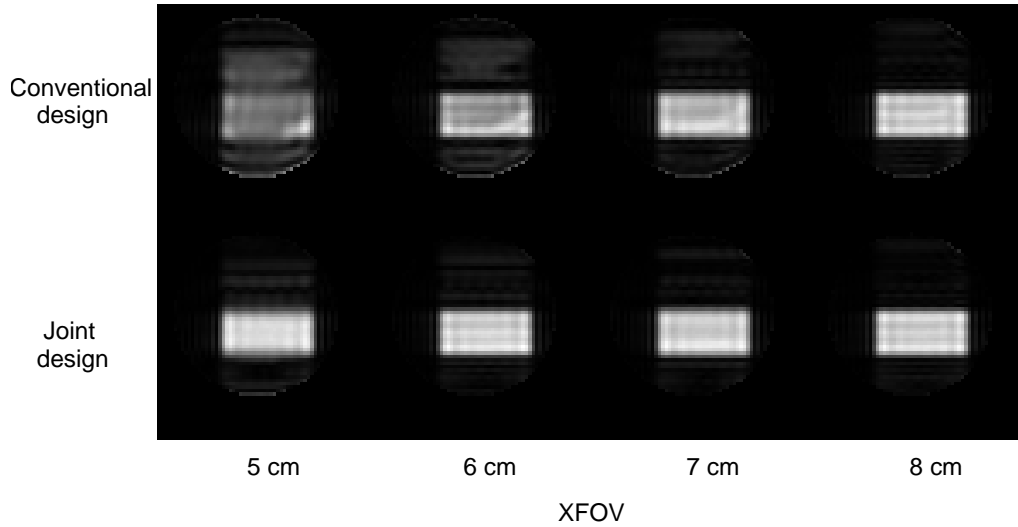
Figure 5.3: Bloch-simulated excitation patterns (magnitude) by conventional and joint designs at high speedup factors. Adjustments of the phase encoding locations in the joint design lead to improved resolution of the aliased excitation.
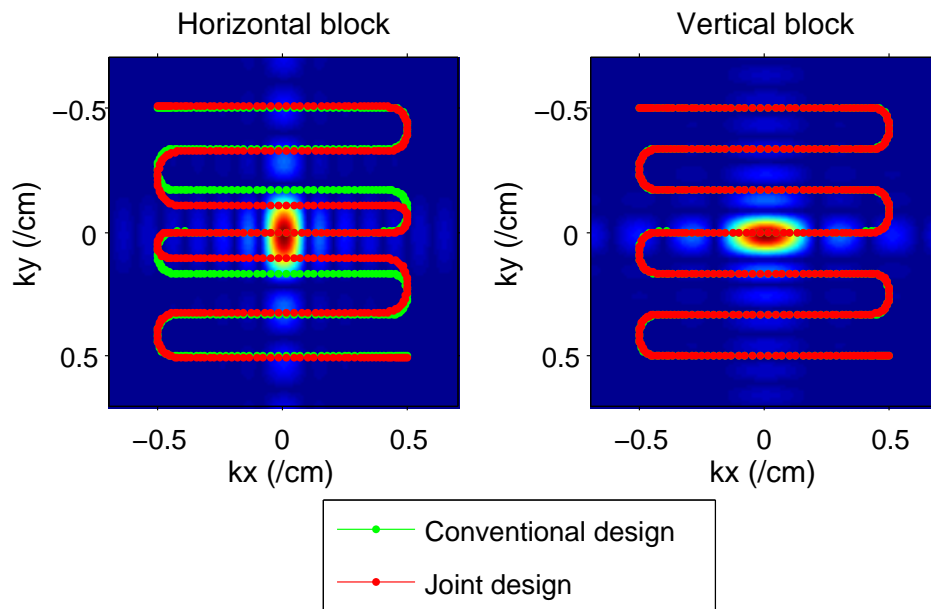
Figure 5.4: EP trajectories with uniform phase-encoding used in the conventional method, and EP trajectories with encoding locations adjusted by the joint design method (XFOV = 6 cm). The adjustments, which are dependent on the specific desired excitation pattern, lead to improvement in excitation accuracy and reduction in total integrated pulse power. The improvement is particularly prominent at high reduction factors. (underlying: desired excitation pattern spectrum)

improvement and pulse power reduction.

We repeated the Bloch simulations for the vertical block desired excitation pattern (Fig. 5.2, red dashed lines), with identical design and simulation parameters. It was interesting that the previously observed margin in excitation accuracy at high speedup factors vanished, while a margin in total integrated power still existed, although it was smaller compared to the horizontal block case (Figs. 5.2a, b). The cost function values that the methods attained were now close for all XFOVs, although the joint design still required significantly longer computational time to reach convergence (Figs. 5.2c,d). One can see, at XFOV = 6 cm for example, that the conventionally and jointly designed trajectories were almost identical (Fig. 5.4b). It suggested that the uniform phase encoding locations were in fact close to being locally optimal for this desired excitation pattern.

5.6   Application to 3DTRF pulses

The joint design framework can also be applied to 3D pulse design problems, such as the 3DTRF pulse design (single-coil). The echo-volumar (EV) trajectory used in the 3DTRF design (Fig. 4.1) can be parameterized in a similar fashion as for the EP trajectory. Let us represent the $x-$ and $y-$ components of the trajectory by a complex function of time: $k_{xy}(t_j) = k_x(t_j) + \imath k_y(t_j), j = 0, \ldots, N-1$. Define complex in-plane phase-encoding locations, $\boldsymbol{\phi} = (\phi_{x0} + \imath\phi_{y0}, \ldots, \phi_{x(L-1)} + \imath\phi_{y(L-1)})^T = (\phi_0, \ldots, \phi_{L-1})^T \in \mathbb{C}^L$. As in Eq. 5.17, $k_{xy}(t_j)$ can be parameterized by $\boldsymbol{\phi}$:

$$(5.18) \qquad k_{xy}(t_j; \boldsymbol{\phi}) \approx \sum_{l=0}^{L-1} \phi_l h(t_j - lT_{\text{PE}}),$$

where $h(t)$ is the rect function and T_{PE} is the duration of one k_z traversal. In matrix form, we can write $\mathbf{k}_{xy}(\boldsymbol{\phi}) \approx \mathbf{H}\boldsymbol{\phi}$, where $\mathbf{H}$ is a matrix whose columns contain samples of time-shifted rect functions. Now, the 3DTRF pulse and its phase-encoding locations can be jointly designed.

Jointly designed 3DTRF pulses were evaluated via Bloch simulations. Compared to the baseline 3DTRF pulse designs described in Chapter 4, joint designs were able to achieve slightly higher excitation accuracy with respect to the desired pattern. The improvements were marginal, though. Disappointingly, the joint design approach could not help to break through the major performance limitations of the 3DTRF pulses. Joint designs were still unable to excite accurately enough, when there were multiple regions of signal loss, or when the resonance frequency offsets were large. Computational time for the joint designs were also overwhelmingly long due to the alternating optimization process, even though the number of CG iterations in the pulse optimization step (Eq. 5.4) could be reduced significantly compared to the baseline case. It renders joint 3DTRF pulse design impossible for online computation.

5.7   Discussion

In this chapter we have proposed a framework for joint design of trajectory and RF pulses for single-coil or parallel excitation. Compared to conventional designs with predetermined trajectories, joint designs can often excite target patterns with significantly improved accuracy and/or reduced total integrated power. The improvements are particularly prominent in parallel excitation at high reduction factors. The benefits come at modest expense of computational time, which could be affordable in practice. The cost-benefit tradeoff depends on the specific desired excitation pattern, and in fact, sensitivity patterns as well (results not shown).

The joint design concept was originally conceived for more flexible choices of phase-encoding locations in the single-coil 3DTRF pulse design. Disappointingly, its benefits are minimal and it cannot help breaking through the performance limitations of the original design. Besides, computation of 3D joint design is too high for online 3DTRF pulse

design.

Stability of the current joint design implementation (i.e., whether it converges to a local minimum or diverges) is sensitive to the threshold of cost function ratio in CG for declaring convergence (we used 99.9% in our simulations), and to a larger extent, the scaling factor on the GD step (α). To ensure convergence in the EP pulse design, we experimented with the technique of *optimization transfer* [111] for updating the phase-encoding locations – the step was determined via constructing a quadratic *surrogate* function that lied above the original cost function, and minimizing it instead of the original cost. This approach guarantees a monotonic decrease in the cost function, effectively preventing divergence. However, implementation of optimization transfer in the joint design requires a large amount of computation, which increases the total joint design computational time. Thus, it may not be favorable for online design purposes.

Besides EP and EV trajectories, the joint design framework can be applied to various non-Cartesian trajectories. One can, for example, expand a spiral trajectory in basis functions such as splines, and jointly optimize the spline coefficient and RF pulses. However, the coefficients have to be updated without violating the peak gradient and slew rate constraints (Eq. 5.5), rendering the trajectory update a constrained optimization problem.

CHAPTER 6

Spectral-spatial pulse for signal recovery

6.1   Introduction

In Chapter 4, I introduced an advanced version of the 3DTRF method. We demonstrated successful signal recovery in a thin slice in both phantom and human head, using 3DTRF pulses as short as 15.4 ms. However, the method failed to provide satisfactory recovery under relatively "harsh" imaging conditions. First, it could not simultaneously recover multiple regions of signal loss, which typically appear in slices close to *both* the air-filled middle ears and sinuses. Second, the magnitude of frequency offsets in the slice volume could not be too large (>75 Hz at 3T). These two limitations render the 3DTRF method inadequate for imaging the most inferior regions of the brain.

The joint design framework was an attempt to break through these limitations. Unfortunately, when applied to 3DTRF pulse design, its performance benefits were marginal and its computational cost was overwhelming. As discussed at the end of Chapter 4, another potential solution is to apply parallel excitation to the 3DTRF method. Thanks to localized transmit coil sensitivity patterns, parallel excitation can provide improved in-plane selectivity compared to using only one coil. It will potentially make in-plane phase-encoding with the echo-volumar (EV) trajectory more effective, resulting in fewer phase-encoding locations and hence shorter pulse length. The performance limitations can potentially be

relaxed. However, the introduction of parallel excitation is bound to increase the complexity of the 3DTRF pulse design. The online pulse design time, which was already overwhelmingly long in the single-coil case, will further increase by multiple folds. Consequently, the method will become even more impractical. In addition, for parallel excitation, extra pre-scans will be necessary for acquisition of the transmit coils' sensitivity maps. Combined with the field map pre-scans, the time required for all the pre-scans can be burdensome.

This predicament motivates a new RF pulse design approach for precompensating the through-plane dephasing. Ideally, the new approach will be able to recover signals over the entire brain, including the most inferior brain slices with multiple loss regions and high frequency offsets. Also, it would be desirable if the new pulses do not need to be computed *online* using the field map acquired from pre-scans. In the ideal case, the pulses can be computed *offline* prior to the fMRI experiment. A collection of pulses designed with different parameter values can be precomputed and stored. Based on field maps acquired currently or from training data, or possibly just based on speculation, a subset of those pulses can be pulled out and deployed at different slice locations. If all these are realized, pulse computational time will no longer be a concern.

To achieve these goals, we need a totally new mechanism for prescribing precompensatory phase variations where they are needed. Perhaps, the new pulse design can give up reliance on information about where dephasing *spatially* occurs (i.e., based on field maps) for adequate precompensation. Instead, it can rely on other quantities that indicate through-plane dephasing. In this chapter we are going to explore such an indicator, and how it can be exploited for signal recovery. Instead of spatially selective pulses, the new method involves sophisticated SPSP pulses that need to be designed iteratively. I will elaborate on the method's basic principles, and subsequently investigate its feasibility for

practical use.

6.2   The correlation assumption

The new signal recovery pulse design relies on a fundamental assumption: *on each individual slice, there is strong spatial correlation between resonance frequency offset and through-plane magnetic field gradient.* If it is true, frequency offset can serve as an indicator for through-plane dephasing. Indeed, correlation between frequency offset and through-plane field gradient can often be observed in axial GRE images of the human head. Fig. 6.1 (left) shows field map of a 1-mm slice close to the sinuses and its corresponding through-plane gradient map estimated via regression (data from human scanning experiment in Chapter 4). Structure of these maps is similar – voxels with high frequency offsets and through-plane gradients are both concentrated at the anterior brain region, with significant overlapping. Scatter plot of the two quantities (Fig. 6.1, right) reveals strong linear correlation.

If this assumption of frequency offset indicating through-plane dephasing is valid, it can be exploited by selective excitation pulses for the purpose of signal recovery. One can conceive a 2D SPSP pulse that is (1) spatially selective for exciting a slice profile, and at the same time, (2) spectrally selective for prescribing precompensatory through-plane phase variation with rate being a function of frequency offset. In essence, such an SPSP pulse creates through-plane precompensatory phase based *not* on the prior knowledge of where dephasing occurs (as for 3DTRF pulses), but instead on the assumption that through-plane dephasing occurs where resonance frequency is off. A collection of SPSP pulses, designed with different rate of through-plane phase variation per frequency offset, can be computed *offline* (prior to the experiment) and stored for repetitive use. In the actual functional experiment, for each slice location, an SPSP pulse is retrieved for deployment

based on the characteristics of the field map acquired online. The choice can also be made based on field maps collected during training, or possibly, just based on speculation. With the latter two options, online field map acquisition can even be abandoned. Note that since the gradient-offset relationship varies from slice to slice, different SPSP pulses have to be applied to different slice locations.
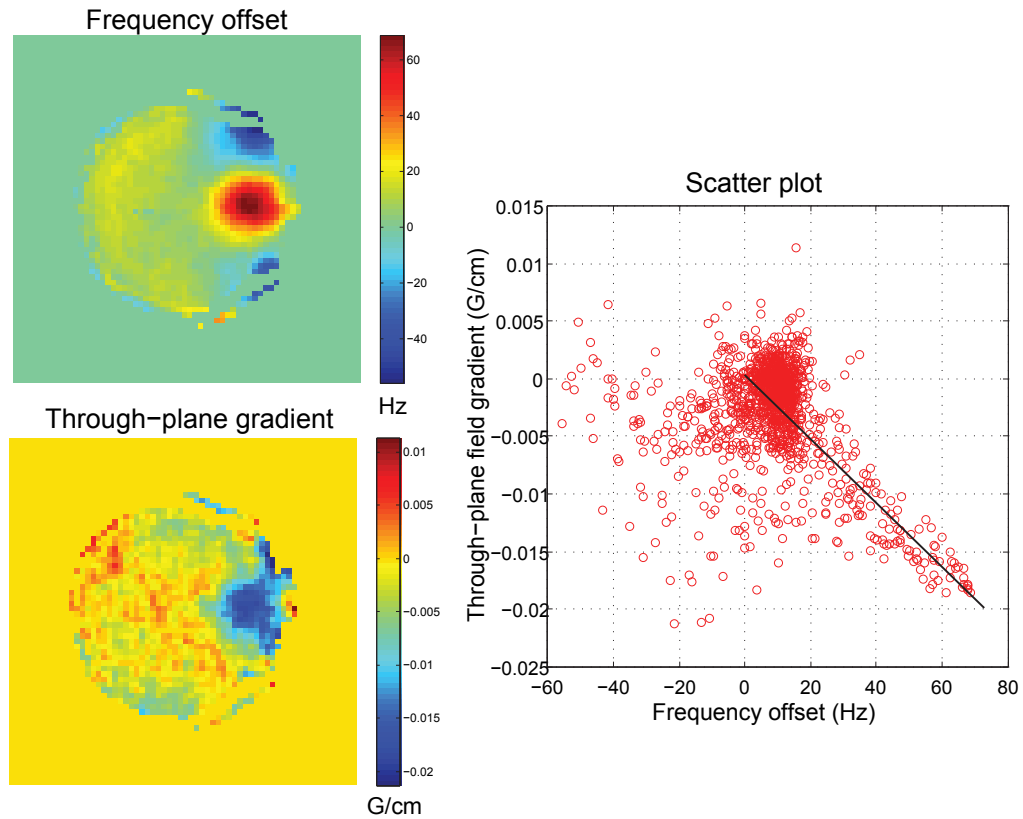
Figure 6.1: Field map of a 1-mm slice through the inferior brain, juxtaposed with its corresponding through-plane field gradient map. Voxels with high offsets and through-plane gradients both reside at the anterior brain region, with significant overlapping. Scatter plot reveals correlation between the quantities, although there are significant outliers.
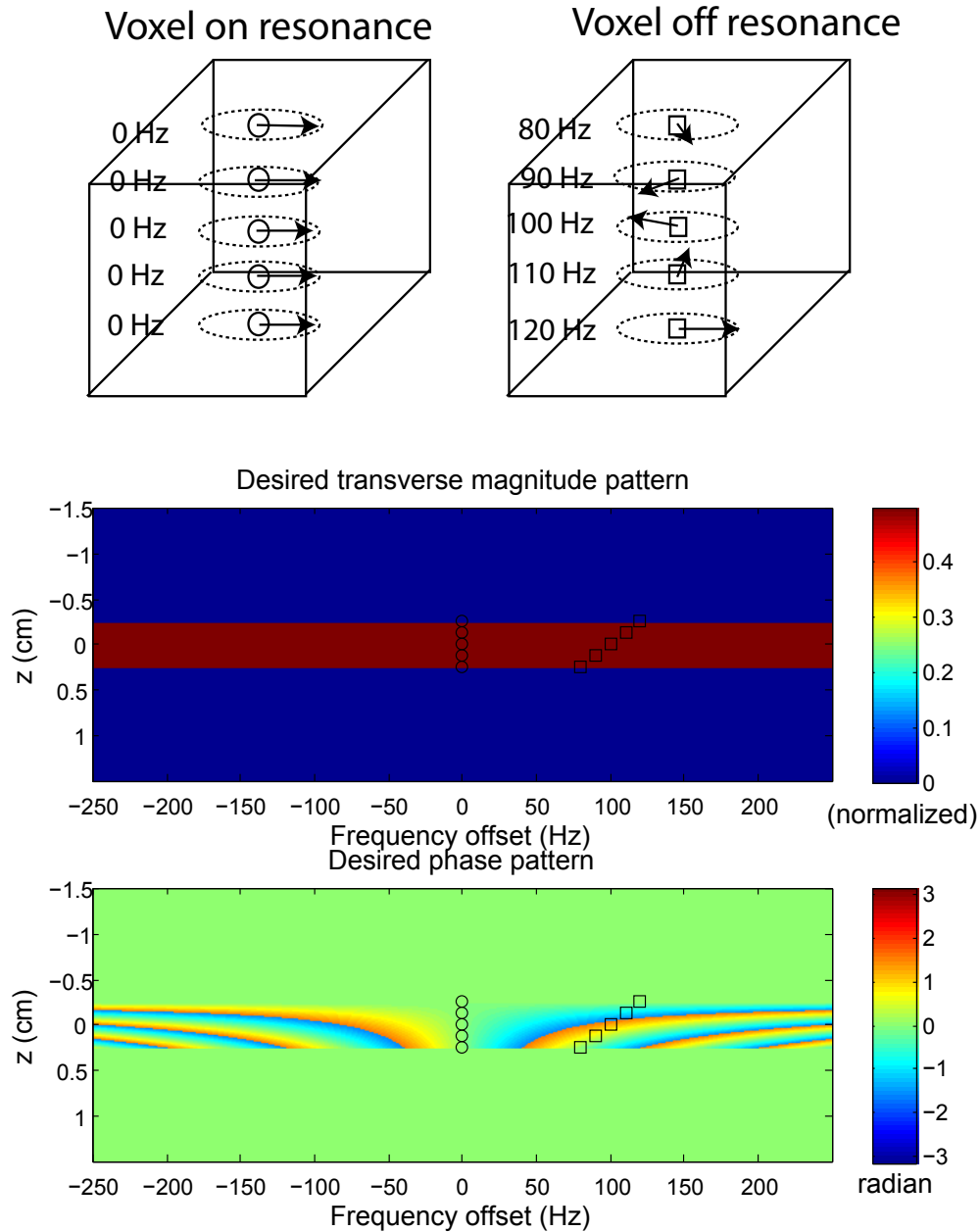
Figure 6.2: Illustration of the effects of an SPSP signal recovery pulse on on- and off-resonance voxels. Upon excitation, through-plane magnetization within the on-resonance voxel flips down and acquires the same phase, as indicated by the circles on the desired pattern. Through-plane magnetization within the off-resonance voxel flips down but acquires different phase values, as can be read off from the squares on the desired phase pattern. Ideally, this phase variation will precompensate for the through-plane dephasing after the pulse ends and hence signal loss will be recovered.

6.3 Principles of SPSP signal recovery

Figure 6.2 shows a desired SPSP excitation pattern that is potentially efficacious for signal recovery. Its magnitude pattern is specified for slice selection at the iso-center ($z = 0$).

Because the slice profile is defined over a wide range of frequency offsets, magnetization in the slice volume flips down with the intended tip angle, as long as its resonance frequency is within the specified range. The desired phase pattern comprises through-plane phase variations with rate proportional to frequency offset. Depending on its spatial position (z) and frequency offset (f), magnetization flips down to the transverse plane with various phase values, without regard to its in-plane location (x, y). A voxel of magnetization on resonance at all intra-voxel z positions get excited with through-plane phase values as indicated by the circles on the desired pattern (Fig. 6.2). The through-plane spins are excited in phase and therefore contribute constructively to the voxel intensity. Meanwhile, an off-resonance voxel with a spread of frequency offsets within (offset-gradient correlation assumed) picks up through-plane phase values such as those indicated by the squares. Phase precompensation is accomplished *if* these phase values match the negative of those caused by through-plane dephasing.

Let us derive a formula for such an SPSP pattern as shown in Fig. 6.2. Assume, as in the 3DTRF case, a 2D GRE imaging scenario. When imaging at slice location z_0 in the presence of an inhomogeneous main field with offsets $\Delta B(x, y, z)$, through-plane dephasing that occurs during the time between RF pulse end to acquisition of k-space origin (T_D) can be described with the first-order through-plane phase variation[1] :

$$(6.1) \qquad \phi(x, y, z; z_0) = -\gamma T_D g_z(x, y)(z - z_0),$$

where $g_z(x, y) = d\Delta B(x, y, z_0)/dz$ denotes through-plane field gradient evaluated at z_0.

---

[1]Note that there is a subtle difference between T_E and T_D. T_E is the time period in which *mesoscopic* spin dephasing (Chapter 1) accumulates and gives rise to BOLD contrast. The accumulation starts as soon as magnetization is flipped down onto the transverse plane (at some point during the pulse). In the basic case of excitation using sinc pulse, for example, spins flip down approximately at the middle of the pulse, and hence T_E starts counting from that time instance to k-space origin acquisition time. On the other hand, T_D is strictly defined as the amount of time allowed for phase evolution *after* the RF pulse is over, up to the time when k-space origin was sampled. In the case of a 3DTRF pulse with its peak almost at the pulse end, T_E approximately equals T_D. It is not generally true with complicated tailored pulses which flip spins down way before pulse end.

Phase precompensation entails selective excitation of a slice volume with negative of this phase pattern embedded:

$$(6.2) \qquad d(x, y, z; z_0) = p(z - z_0) \cdot \exp(-\imath \phi(x, y, z; z_0)),$$

where $p(z - z_0)$ is the slice profile centered at z_0. If frequency offset and through-plane field gradient are correlated, we can approximately express the field gradient as a function of field offset, $g_z(f)$, instead of a function of space. In particular, if the correlation is linear:

$$(6.3) \qquad g_z(f) \approx \alpha f,$$

with α being a proportionality constant. It is a design parameter that we tune to create adequate precompensatory phases. Now a desired SPSP pattern can be defined by replacing $g_z(x, y)$ in Eq. 6.1 with αf. Equation 6.2 becomes:

$$(6.4) \qquad d_{spsp}(f, z; z_0) = p(z - z_0) \cdot \exp(\imath \gamma T_D \alpha f(z - z_0)) \,.$$

An SPSP pulse with this f-z response is potentially efficacious for precompensation of through-plane dephasing.

Unfortunately, with non-zero α values, this desired SPSP pattern is not attainable, because it is physically impossible to render positive phase variations along the spectral dimension[2]. To make the pattern in Eq. 6.4 attainable, we have to introduce a z-dimension shift (z_{shift}):

$$(6.5) \qquad d_{spsp}(f, z; z_0) = p(z - z_0) \cdot \exp(\imath \gamma T_D \alpha f(z - z_0 - z_{shift})),$$

such that the phase variations along f are always non-positive within the slice ($z \in [z_0 - W/2, z_0 + W/2]$, where W is the slice thickness). A good choice of z_{shift} is $-W/2$. It

---

[2]One can see it mathematically: the phase in the spectral encoding factor $exp[2\pi \imath f(t - T)]$ in the SPSP k-space equation (Eq. 2.11) is always negative function of f, since $t \in [0, T]$.

leads to zero phase variation along f at $z = z_0 - W/2$, and the phase variation rate along f at $z = z_0 + W/2$ is kept to a minimum possible. This choice fosters shortest pulse length for a given desired pattern. Now this attainable desired pattern (e.g., Fig. 6.2) is to become the target for SPSP pulse design.

6.4   Iterative SPSP pulse design

Selective excitation of the SPSP pattern in Eq. 6.5 is facilitated by the SPSP k-space concept discussed in Chapter 2. Because of the special form of this desired pattern, the conventional method of separate designs of spatial subpulse and spectral envelope (Section 2.6.2) is not applicable. Iterative SPSP pulse design (Section 3.4.1) must be used. For iterative design, we specify the discrete desired pattern via sampling the continuous pattern (Eq. 6.5) over the $f - z$ plane (criteria for adequate sampling will be discussed in the Implementation section). As in the 3DTRF case, the samples are columnized into a vector ($\mathbf{d}_{spsp}$), and an SPSP pulse can be iteratively designed via the following minimization problem (Eq. 3.18):

$$(6.6) \qquad \hat{\mathbf{b}} = \arg\min_{\mathbf{b}} \left\{ \|\mathbf{A}_{spsp}\mathbf{b} - \mathbf{d}_{spsp}\|_{\mathbf{W}}^2 + R(\mathbf{b}) \right\},$$

where $\mathbf{A}_{spsp}$ is a system matrix whose elements are given in Eq. 3.17 in Chapter 3, and $R(\mathbf{b})$ denotes a general regularization term that penalizes RF power.

The k-space trajectory used in the system matrix is a critical design component that affects how well the desired pattern is attained. One can adopt the oscillatory z gradient waveform (Fig. 2.2) used in conventional SPSP pulse design. There are several criteria in choosing the parameters of the oscillatory trajectory. First, the k_z coverage has to be wide enough, so that the slice profile specifications are met and the z-dimension phase variations in the desired pattern can be rendered. This consideration sets a lower limit on the area of each trapezoid in the oscillatory gradient. Second, the k_f coverage has to be

wide enough so that the f-dimension phase variations in the desired pattern can be created. It sets a lower limit on the duration of oscillation. Lastly, the oscillation frequency has to be sufficiently high, such that k_f is sampled densely enough. It assures that the f-dimension excitation aliasing is not too severe, facilitating design accuracy in the ROI in f-z space.

Determining the right oscillation parameters involves finding a balance amongst meeting these criteria, while keeping the trajectory as short as possible. Notice that the larger α is in the desired pattern (Eq. 6.5), the more rapid the f-dimension phase variations become, and consequently the pulse has to be longer to render them. This explains why setting z_{shift} to $-W/2$ fosters the shortest pulse length possible for a given α – it leads to the slowest maximal phase variation along f at $z = z_0 + W/2$, while guaranteeing there are no unattainable positive variations along f at other z locations within the slice.

6.5 Implementation

This section discusses implementation issues in designing SPSP pulses for signal recovery. It also contains parameter values actually used in the designs in this chapter.

6.5.1 Desired pattern specification

The complex desired SPSP pattern was specified via sampling Eq. 6.5 over the f-z plane. There are several considerations in choosing the sampling grid. First, in the z dimension, sampling has to cover the entire range of z from which MR signals can arise. It implies that zeros have to be padded to all of the out-of-slice spatial locations. In the f dimension, the sampling range should contain the range of frequency offsets present in the entire subject head. Sampling intervals in both f and z have to be small enough, so that the slice profile and phase variations along either dimension are adequately represented according to the Nyquist criterion.

For all the pulses designed for the phantom and human experiments, the sampling range

was 500 Hz (f) × 20 cm (z), with matrix size 300 (f)× 1200 (z). The other common parameters were as follows: slice profile was rectangular with width = 5 mm, flip angle = 30 degrees, and z_{shift} = 2.5 mm (half of the slice thickness, as recommended). For testing purposes, a collection of eleven SPSP pulses were designed using α values ranging from -1×10^{-4} to -3.5×10^{-4} G/cm/Hz, at -0.25×10^{-4} G/cm/Hz intervals. They had lengths ranging from 8.35 to 16.02 ms, depending on trajectory parameters (discussed below). In all cases, T_D was assigned to be T_E (pulse sequence parameter) minus half of the pulse length. The desired SPSP pattern for $\alpha = -2 \times 10^{-4}$ G/cm/Hz is shown in Fig. 6.3 (Note that only the central 3 cm in z is shown. The rest is zero-padded.).
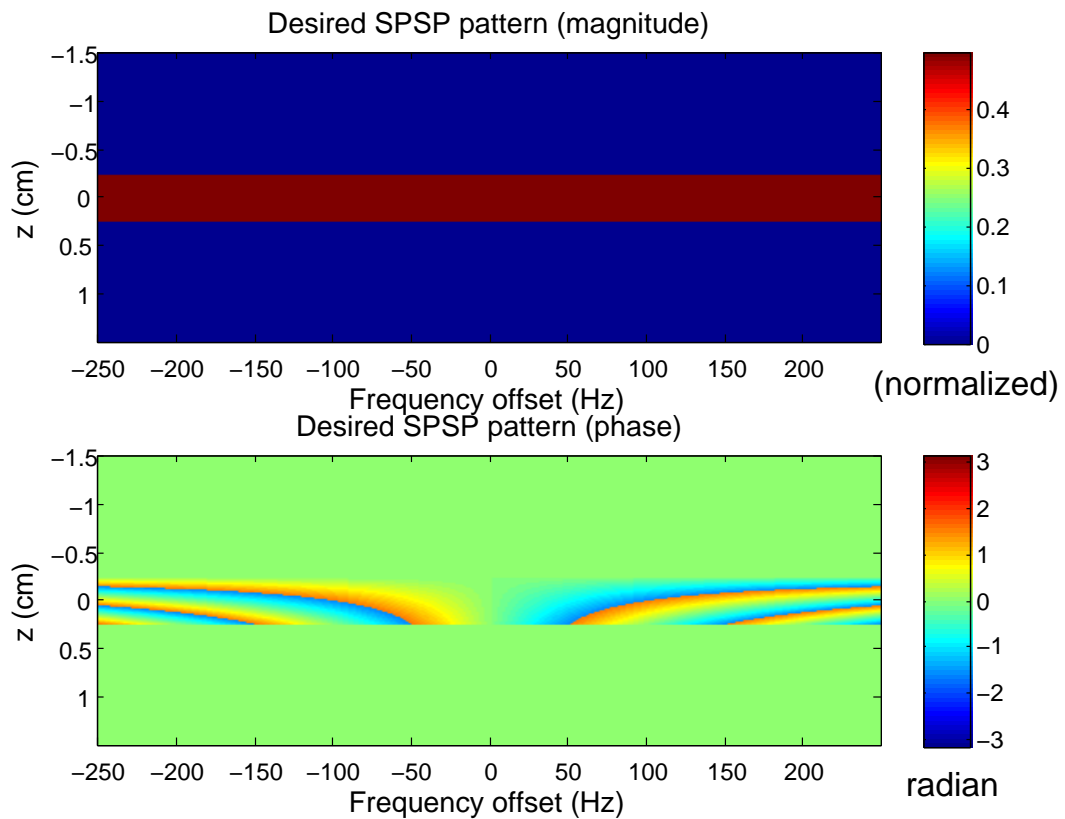
Figure 6.3: Desired SPSP excitation pattern ($\alpha = -2 \times 10^{-4}$ G/cm/Hz) for signal recovery. Note that only the central 3 cm in z is shown (the rest is zero-padded).

6.5.2   Trajectory and ROI specification

k-Space trajectories were produced by oscillatory z gradient waveforms, with gradient trapezoids compliant to the maximum gradient and slew rate constraints, which were 40 mT/m and 150 T/m/s, respectively. According to the rationale discussed previously, we manually determined trajectories in an *ad hoc* fashion based on Bloch simulations of the designs. For the eleven pulses with decreasing α values from -1×10^{-4} to -3.5×10^{-4} G/cm/Hz, we defined trajectories with increasing oscillation periods (2.5 to 3 ms) and increasing number of cycles (6 to 10). It resulted in pulse lengths ranging from 8.35 to 16.02 ms. The ROI, specified via matrix $\mathbf{W}$ in Eq. 6.6, covered the entire f-z region over which the desired pattern was specified.

6.5.3   Iterative pulse design

SPSP signal recovery pulses were designed via solving Eq. 6.6 with 100 CG iterations, which was sufficient for full convergence. No regularization was applied to the cost function (i.e., $R(\mathbf{b}) = 0$). To speed up computation, the forward and backward projections in the CG routine were handled using NUFFT [102], which used a table-based, min-max interpolator (with Kaiser-Bessel scaling) using 8 neighbors and an upsampling factor of 2 in both the spatial and spectral dimensions. A hamming window (function of k_z) was applied to suppress ripples in the slice profile caused by Gibbs phenomenon. The iterative pulse designs, implemented with Matlab on a 3.4GHz Pentium workstation with 2 GB memory, took 94.71 to 103.10 s for completion. Figure 6.4 shows the 11.48-ms SPSP pulse designed with $\alpha = -2 \times 10^{-4}$ G/cm/Hz, oscillation period = 3 ms, and 3.5 oscillation cycles.
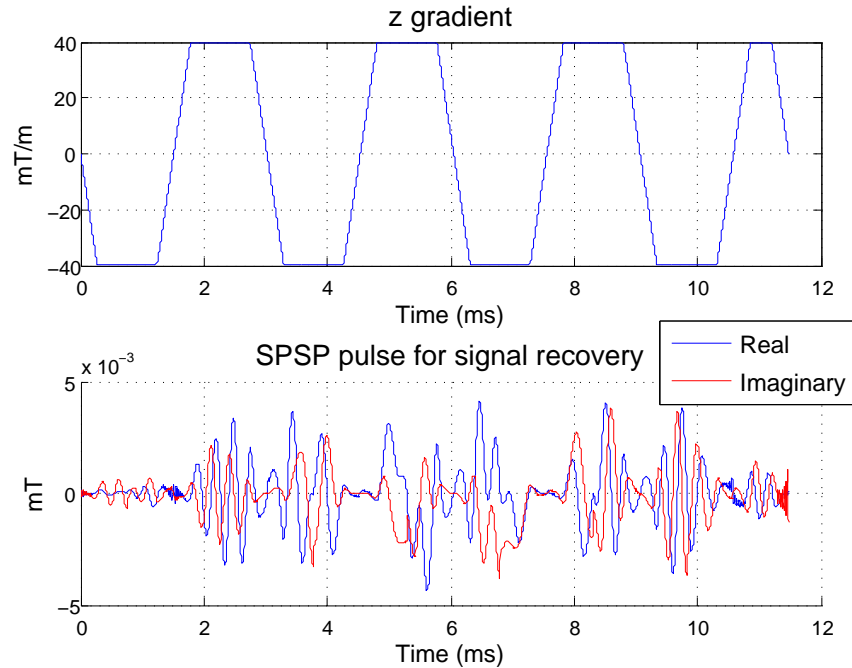
Figure 6.4: The SPSP pulse designed for the desired pattern shown in Fig. 6.3, accompanied by its oscillatory z gradient (upper panel).

6.6   Phantom and human experiments

We conducted scanner experiments to evaluate our SPSP pulse designs. They were performed on our GE 3 T Excite MRI scanner (GE Healthcare, WI, USA), with a head coil for both transmission and reception. In the first stage experiments were performed on a spherical homogeneous water phantom. Afterwards, signal recovery was tested in the actual human head. A healthy volunteer participated in the human experiment, approved by the Institutional Review Board of the University of Michigan, after providing informed consent. As discussed in the previous section, we designed and stored eleven SPSP pulses with different α values prior to the experiment. Each pulse was designed with slightly different trajectory parameters and therefore had different lengths. In both phantom and human head, we attempted signal recovery via manually choosing one of the SPSP pulses from our collection. Note that as in the case of sinc pulses, T_E was defined as the time

interval from middle of the SPSP pulse to acquisition of the spiral origin[3]. High-order shimming was performed prior to all the experiments. For the SPSP pulses, the z gradient waveform was shifted backward by 150 μs to compensate for the delay between the RF and gradient channels. Images were reconstructed using the off-resonance-compensated CP method [15].

6.6.1 Imaging the SPSP excitation pattern

First, we imaged the patterns excited by our SPSP pulses to verify that the pulses actually produced the desired SPSP responses. We used a pulse sequence commonly found in the SPSP pulse design literature [49, 61, 63]. The SPSP pulse was played out with the RF magnitude and phase channels. The oscillatory z gradient was applied to one of the transverse-plane gradient channels (G_y), while a constant gradient was applied to the other (G_x). This constant gradient simulated a frequency offset axis. Afterwards, a slice-selective 180-degree pulse was applied in the third dimension (z). It was followed by a spiral-out readout that acquired the image. The sequence's parameter values were as follows: G_x = -0.00575 G/cm, mapping the x-dimension FOV of 20 cm to a spectral FOV of 500 Hz. The oscillatory gradient waveform, played on G_y, was scaled to have maximum amplitude at 0.6 G/cm (4 G/cm in original design). It mapped the y-dimension FOV of 20 cm to a slice-select-direction FOV of 3 cm. As a result, the SPSP pattern was "magnified" along the slice-select direction so that the through-plane phase variations could be clearly observed. The other parameter values were as follows: acquisition matrix size = 128×128, number of spiral interleaves = 8, $T_E = 20$ ms, $T_R = 1$ s, and thickness of slice excited by the 180 pulse was 1.5 cm.

The acquired images provided evidence that the pulses succeeded in creating SPSP ex-

---

[3]With Bloch simulations, we verified that, on average (over f-z space), spins were flipped down to the transverse plane at the middle of the SPSP pulses.
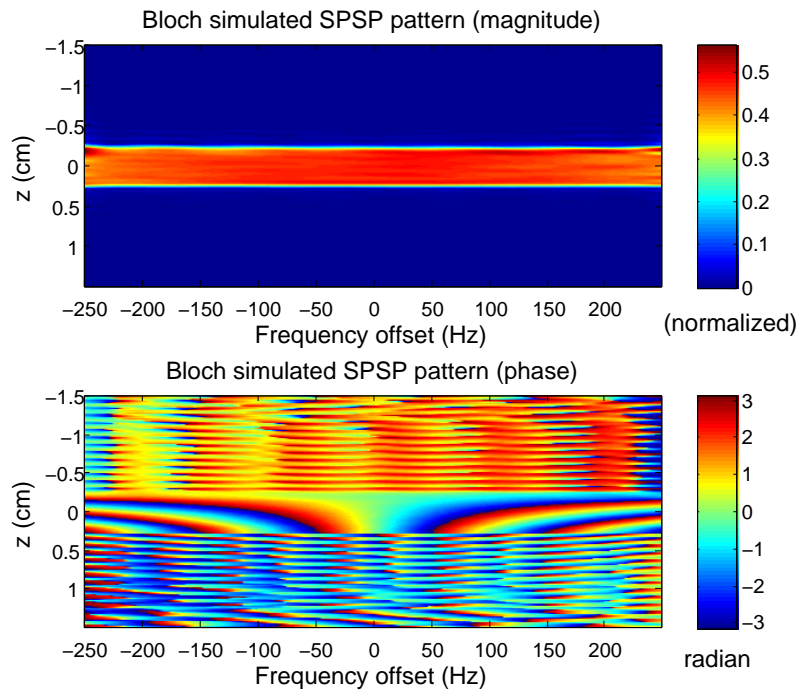
Figure 6.5: Bloch simulation of the SPSP pulse in Fig. 6.4. It closely matches the desired pattern (Fig. 6.3).
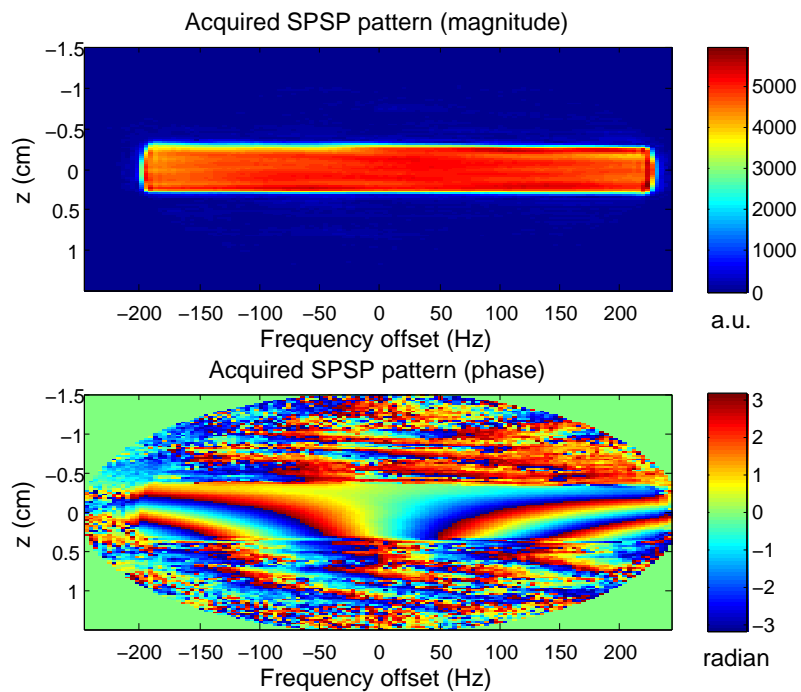
Figure 6.6: SPSP excitation pattern of the pulse in Fig. 6.4 acquired from scanner. It closely matches the desired (Fig. 6.3) and Bloch-simulated patterns (Fig. 6.5).

citation patterns close to the desired one. As an example, Fig. 6.5 shows result from Bloch simulation of the SPSP pulse in Fig. 6.4. It resembled the desired pattern (Fig. 6.3). The pulse's actual response obtained from the scanner (Fig. 6.6) closely matched the simulated response in both magnitude and phase. Fidelity of the acquired SPSP pattern suggests that the pulse was indeed properly designed and played out in the scanner. SPSP responses of other pulse designs were also imaged, showing good resemblance to their corresponding desired and simulated patterns.

6.6.2 Signal recovery in phantom

Reassured that the SPSP pulses excited the correct patterns, we proceeded to test signal recovery on the water phantom. To emulate the magnetic field distortion in the human head, a small piece of ferromagnetic metal (half piece of staple) was attached to the phantom surface inferior to the imaging plane through isocenter ($z = 0$). After high-order shimming, we estimated field maps from two sets of GRE images of 1-mm thin slices, which were acquired with a slight T_E difference [90]. Fig. 6.7 (upper left) shows the field map through iso-center, revealing significant field inhomogeneity at the phantom region superior to the metal. With field maps acquired for contiguous 1-mm slices, through-plane field gradient map (Fig. 6.7, lower left) was estimated via through-plane linear regression. Its maximum amplitude was around -0.02 G/cm, comparable to that typically measured in the inferior brain at 3 T. Resemblance of the field and gradient maps suggested strong correlation between the two quantities, as confirmed by the scatter plot (Fig. 6.7, right). The correlation was not only strong, but also appeared linear with an offset. This experimental setup provides a good venue where the correlation assumption *is* valid for testing signal recovery.

We first obtained a baseline signal loss image using a GRE sequence with a conven-
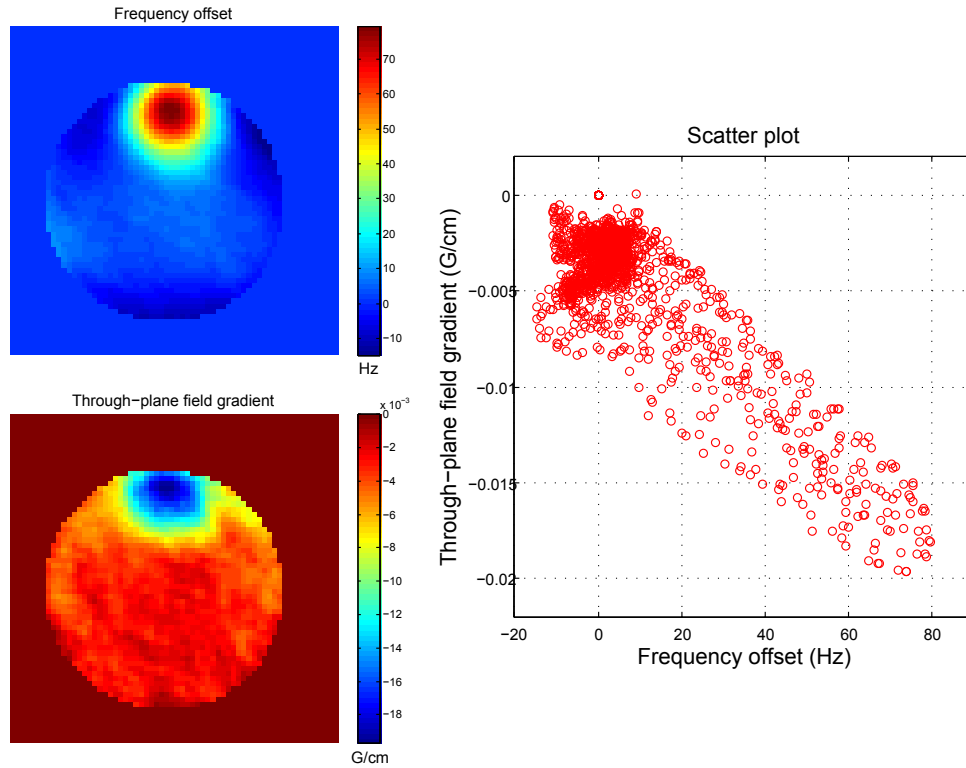
Figure 6.7: Left: field and through-plane field gradient maps of the imaging plane in the phantom experiment. Right: scatter plot reveals strong linear correlation between the quantities.

tional sinc pulse. The sinc pulse was 3.2 ms long, Hanning-windowed, and selective for a 5-mm slice with flip angle of 30 degrees. $T_E = 30$ ms. $T_R = 1$ s. For data readout, we used 16 spiral-in-out [28] interleaves for a 24 cm FOV and matrix size of 256×256. The high number of spiral interleaves minimized phase error during readout caused by field inhomogeneity, whereas the fine in-plane resolution reduced the effect of in-plane dephasing. As a result, through-plane dephasing was isolated as the dominant cause of signal loss. Fig. 6.8a shows the acquired image, with complete signal loss at the region where the through-plane field gradient had high magnitude.

Subsequently, we attempted to recover the lost signals with an SPSP pulse. While all

the parameters in the GRE sequence remained unchanged, the sinc pulse was replaced by an SPSP pulse. Amongst the eleven SPSP pulses that we designed with different α values, the 11.48-ms pulse designed with $\alpha = -2 \times 10^{-4}$ G/cm/Hz, shown in Fig. 6.4, was the most effective in recovering the signal loss (6.8b). The almost complete recovery suggested that the pulse was highly effective in precompensating the through-plane dephasing. Matching of the phantom outline in the SPSP and sinc images suggested that slice selection by the SPSP pulse was accurate. On the other hand, intensity of voxels away from the loss region remained mostly unaffected, without regard to the SPSP pulse in use.

In realistic fMRI studies, it is impossible to use 16 interleaves and large matrix size of 256×256, because of the forbiddingly high cost in temporal resolution. Therefore, we tested the effect of the SPSP pulse in a standard single-interleave spiral-in-out GRE sequence, with matrix size of 64×64. All other imaging parameters remained the same as in the high-resolution case. Fig. 6.8c shows the image acquired with the sinc pulse. At the phantom region superior to the attached metal, the image was marred by distortions caused by phase error during readout and signal loss due to in-plane dephasing, in addition to signal loss due to through-plane dephasing. With the chosen SPSP pulse ($\alpha = -2 \times 10^{-4}$ G/cm/Hz), the overall image artifact was significantly mitigated (Fig. 6.8d). Although the SPSP pulse was incapable of (because it was not designed for) counteracting the phase error during readout and in-plane dephasing, precompensation of the through-plane dephasing was effective in improving the overall image quality.

Unlike 3DTRF pulses, we found that the SPSP pulses could recover signals effectively even when frequency offsets were as high as 150 Hz (results not shown), or when there were multiple regions of signal loss. To simulate signal loss on slices proximal to *both* the middle ear air spaces and sinuses in the human head, two more pieces of metal were

Sinc, 256x256, nl=16   SPSP, 256x256, nl=16

Sinc, 64x64, nl=1   SPSP, 64x64, nl=1
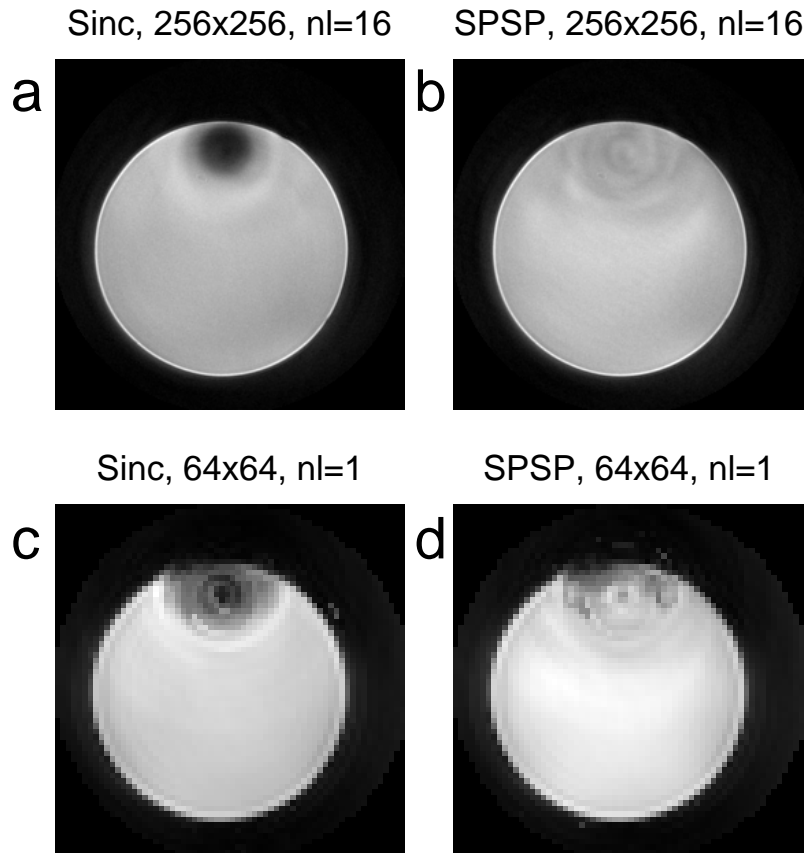
Figure 6.8: Signal recovery on phantom attached with a piece of metal on its inferior surface. a: using a GRE sequence with a sinc pulse, signal loss occured where the field was distorted. Because of the high image resolution and number of interleaves (nl), the loss was predominantly caused by through-plane dephasing. b: with the same sequence using the SPSP pulse in Fig. 6.4, the loss was almost completely recovered. c: acquired with a single spiral-in-out interleave and low resolution, the image suffers from in-plane dephasing and phase error during acquisition in addition to through-plane dephasing. d: precompensation of the through-plane dephasing using the SPSP pulse significantly improved the overall image quality.

attached to the inferior surface of the phantom. They were identical to the first piece attached, and resided at approximately the same distance from the imaging plane. After performing high-order shimming again, the previous experiment was repeated using the same sequences with the sinc and SPSP pulses.

Fig. 6.9a shows the image acquired using the spiral-in-out GRE sequence with sinc pulse (16 spiral-in-out interleaves, matrix size = 256×256). As expected, three regions

of signal loss appeared in the image close to the attached metal pieces. Using the same sequence with the chosen SPSP pulse ($\alpha = -2 \times 10^{-4}$ G/cm/Hz), the loss regions were simultaneously recovered, as shown in Fig. 6.9b. The almost complete recovery suggested that the pulse was highly effective in precompensating the through-plane dephasing, even when it occurred in multiple regions.

As before, we tested the SPSP pulse with a standard single-interleave spiral-in-out GRE sequence, with matrix size of 64×64. All other imaging parameters remained the same as in the high-resolution case. Fig. 6.9c shows the image acquired with the sinc pulse. The artifacts in the one-metal-piece image (Fig. 6.8c) now appeared at three distinct regions. Application of the chosen SPSP pulse precompensated the through-plane dephasing, and led to simultaneous artifact reduction at all three regions (Fig. 6.9d).

6.6.3 Signal recovery in human

The goal of the human experiment was to test SPSP recovery method in the human head, in which the field variations were more complex than in the homogeneous water phantom. The same collection of precomputed and stored SPSP pulses (designed with different α values) were prepared for signal recovery attempts. For both the sinc and SPSP pulses, we used the same GRE sequence as in the phantom experiment, with the same parameter values. Field maps and through-plane gradient maps were estimated in the same way as in the phantom case.

Fig. 6.10 (upper left) shows the field map of an axial slice through the inferior brain. The field at the anterior brain region, superior to the sinuses, was highly distorted. As in the phantom case, the corresponding through-plane field gradient map (lower left) shows that significant through-plane dephasing occurred at the same anterior region. Linear correlation between the offset and through-plane gradient is again revealed with a scatter plot

Sinc, 256x256, nl=16   SPSP, 256x256, nl=16

a   b

Sinc, 64x64, nl=1   SPSP, 64x64, nl=1

c   d
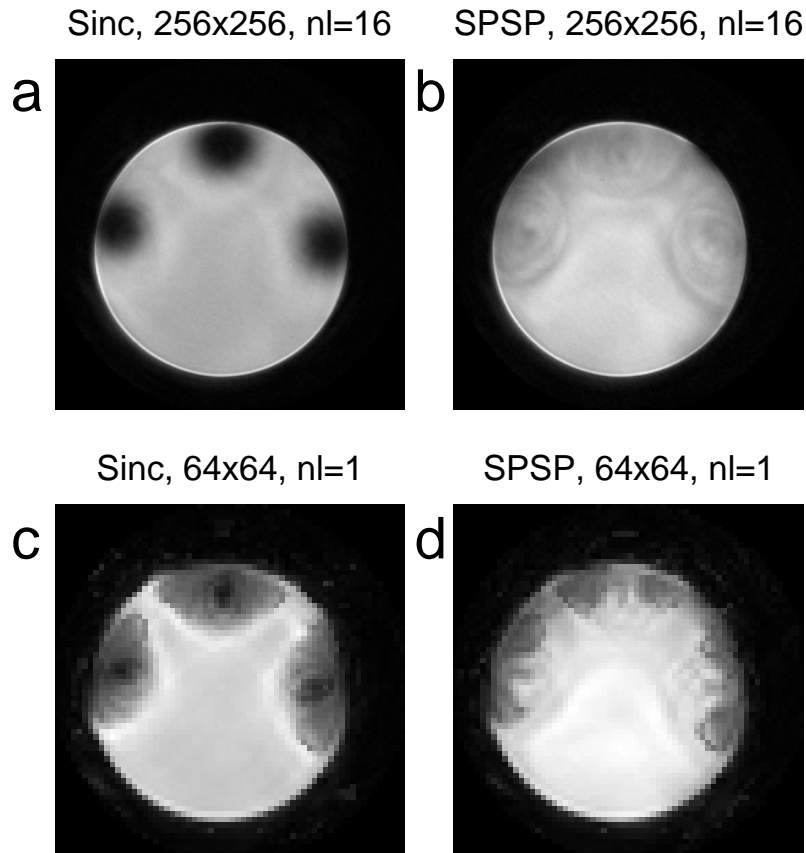
Figure 6.9: Unlike 3DTRF pulses, the SPSP pulses could recover signal loss at multiple image regions. a: using a GRE sequence with a sinc pulse (16 interleaves (nl=16), matrix size $= 256 \times 256$), signal loss was observed at the phantom regions proximal to the three attached pieces of metal. b: with the same sequence using the SPSP pulse in Fig. 6.4, the loss was almost completely recovered. c: acquired with a single spiral-in-out interleave and low resolution, the image suffered from in-plane dephasing and phase error during acquisition in addition to through-plane dephasing. d: Precompensation of the through-plane dephasing using the SPSP pulse significantly improved the overall image quality.

(right). However, compared to the phantom case (Fig. 6.7), there are significantly more outliers away from the correlation axis. They correspond to the fraction of brain regions where the correlation assumption is invalid (e.g., the latero-anterior regions next to the major site of off resonance).

Amongst the eleven SPSP pulses we computed, the 12.99-ms pulse designed with $\alpha = -2.5 \times 10^{-4}$ G/cm/Hz (Fig. 6.11) was the most effective in precompensation. Fig-
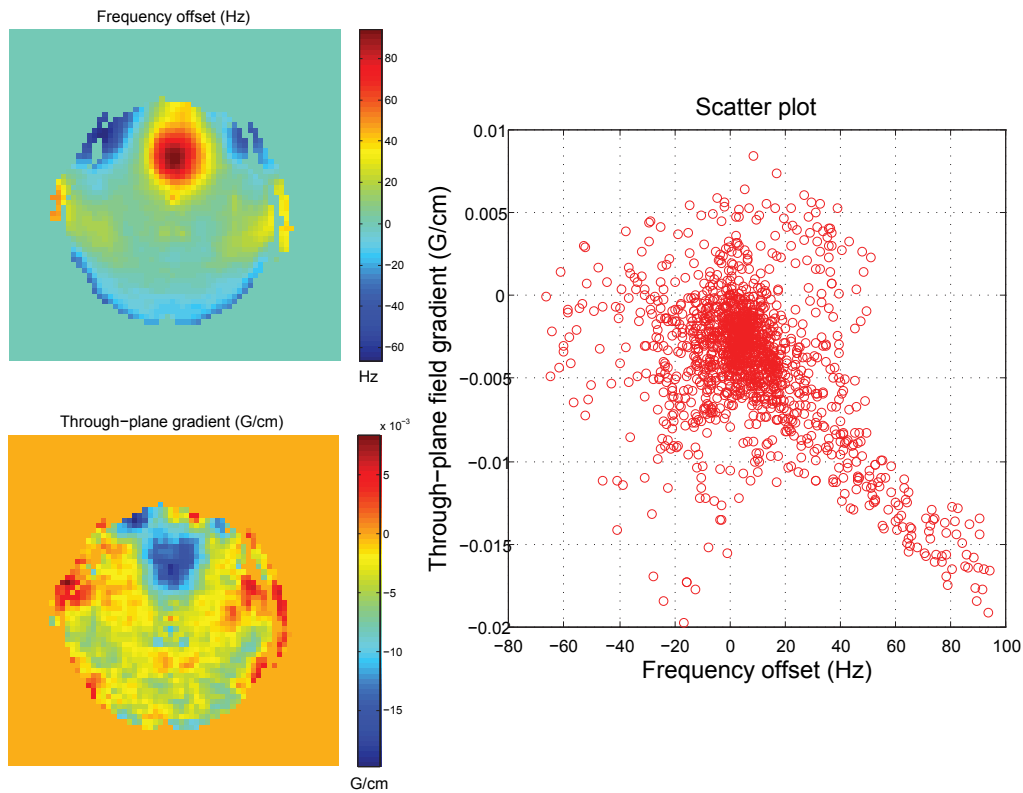
Figure 6.10: Left: field and through-plane field gradient maps of the imaging plane in the human experiment. Right: scatter plot reveals linear correlation between the quantities.

ures 6.12a,b show the high-resolution GRE images acquired using sinc and SPSP pulses, respectively. As discussed in the phantom experiment, due to the high resolution and number of readout interleaves, through-plane dephasing was isolated as the sole contributor to the signal loss in the sinc case (a). The almost complete recovery with the SPSP pulse (b) demonstrated that the pulse was very effective in through-plane phase precompensation. Matching of the brain outline with that acquired with the sinc pulse suggested that slice selection was accurate with the SPSP pulse.

Unfortunately, the SPSP pulse ceased to be beneficial when it was installed in the standard low-resolution, single-interleave sequence (Fig. 6.12c,d). In this case, field inhomogeneity at the anterior site led to rampant in-plane dephasing and acquisition phase error as well as through-plane dephasing. As a result, when the SPSP pulse was used, recovery
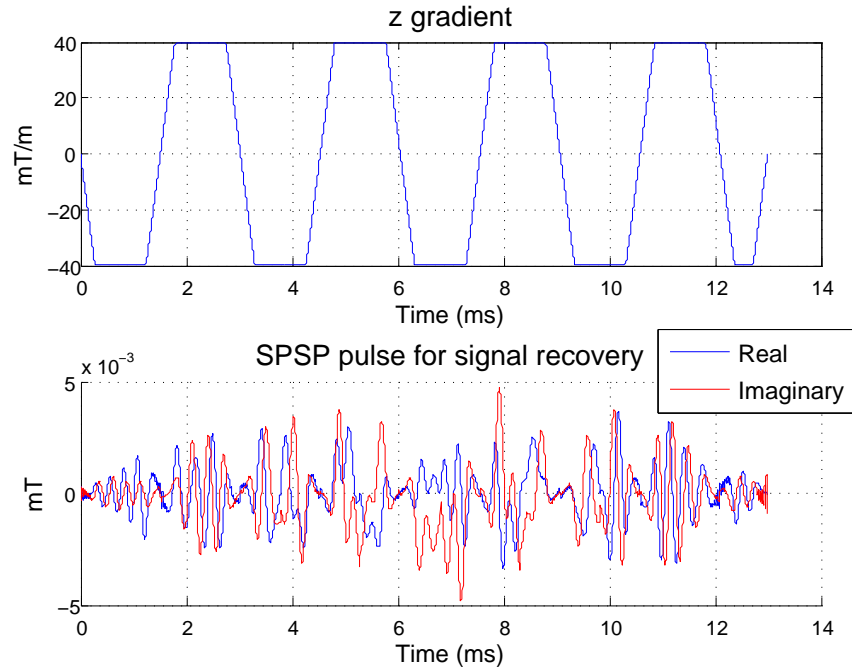
Figure 6.11: The SPSP pulse designed with $\alpha = -2.5 \times 10^{-4}$ G/cm/Hz, accompanied by its oscillatory z gradient (upper panel). This pulse was deployed in the human experiment (Fig. 6.12).

in the through-plane direction was veiled by the loss caused by the other problems. The artifact at the anterior brain remained unresolved.

Notice, also, the signal level at the posterior brain was slightly reduced (Fig. 6.12b,d) whenever the SPSP pulse was applied. This observation can be explained in terms of violation of the correlation assumption – the negative frequency offsets at the posterior region was *not* accompanied by positive through-plane gradient values (Fig. 6.10, left) as assumed in Eq. 6.3. As a result, through-plane phase variation was inappropriately created there, causing the signal loss that we observed.

6.7 Discussion

In this chapter we have explored a novel approach to precompensate through-plane dephasing for signal recovery. The method relies on the assumption that at each slice location, resonance frequency offset can serve as a good indicator of through-plane dephasing.
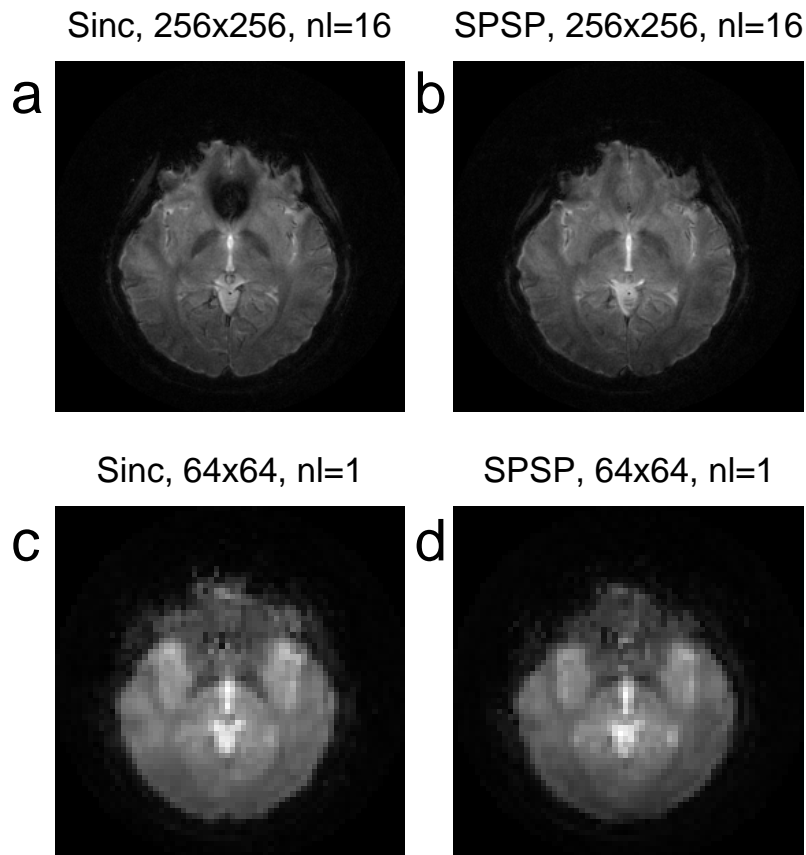
Figure 6.12: Signal recovery in the inferior human head. a: using a GRE sequence with a sinc pulse (16 interleaves (nl=16), matrix size = 256 × 256), signal loss was observed at the anterior region above the sinuses. b: With the same sequence using the SPSP pulse in Fig. 6.11, the loss was almost completely recovered. c: acquired with a single spiral-in-out interleave and low resolution, the image suffered from in-plane dephasing and phase error during acquisition in addition to through-plane dephasing. d: precompensation of just the through-plane dephasing using the SPSP pulse failed to improve image quality.

Specially designed 2D SPSP pulses exploit such correlation to create through-plane precompensatory phases, with variation rate being function of frequency offset. A collection of these SPSP pulses (designed with different parameter values) can be computed and stored prior to the fMRI study. Based on field maps acquired online or from training data, or possibly just based on speculation, individual pulses are retrieved and deployed at different slice locations.

6.7.1   Advantages

The SPSP signal recovery concept was proven in phantom and human experiments. First we successfully verified on the scanner that the pulses produced the desired SPSP responses. Afterwards, we demonstrated that the method was very effective in through-plane phase precompensation, in both phantom and human head. For images in which through-plane dephasing was isolated as the sole contributor to signal loss, the SPSP method achieved almost complete recovery. Recovery was successful even when there were multiple signal loss regions, or when frequency offsets were high ($> 150\,\mathrm{Hz}$). It represents a major step forward in signal recovery efficacy relative to the 3DTRF method. For single-interleave, low-resolution phantom images distorted *also* by in-plane dephasing and readout phase error, through-plane precompensation was effective in improving the overall image quality in the phantom case. However, in our human experiment, recovery in the through-plane direction was veiled by artifacts caused by the other problems originating from the inhomogeneous field.

The novel SPSP signal recovery mechanism is groundbreaking, not just because of its improved signal recovery efficacy, but also because it allows the cumbersome pulse computation to take place offline prior to the fMRI experiment. It saves the waiting time for pulse computation amid the fMRI study. This feature is important, because it eliminates the demanding hardware (fast computer) and software (efficient implementation) requirements for fast online computation such as in the 3DTRF case. It also avoids the potential problem of field pattern changes in between field map measurement and pulse deployment.

Another advantage of the SPSP pulses, compared to 3DTRF pulses, is a reduction in temporal resolution cost in the fMRI study. For given signal recovery efficacies, the SPSP pulses are shorter than 3DTRF pulses. For example, the 3DTRF pulse used in phantom demonstration (Fig. 4.8) was 15.4 ms long, whereas the SPSP pulse in the phantom demon-

stration in this chapter was only 11.48-ms. In addition, because pulse power is distributed throughout the entire SPSP pulse (e.g., Figs. 6.4, 6.11), it is justifiable to consider that T_2^* contrast starts accumulating from middle of the pulse (in contrast to the 3DTRF case, in which most energy was applied at the spike close to pulse end, therefore accumulation starts at pulse end). Because of these two reasons, the extra time needed for pulse application in each T_R is reduced. Hence, the temporal resolution penalty of the SPSP recovery method is lower than the 3DTRF method.

6.7.2 Problems

A potential problem of the SPSP signal recovery method is that the correlation assumption does not hold well on individual slices. When frequency offset is weakly correlated to through-plane dephasing and hence does not serve as its indicator, precompensatory phases can be misplaced – through-plane dephasing will be insufficiently or overly precompensated, and spins originally in phase will inappropriately pick up through-plane phases that result in dephasing that did not originally occur. As a result, signal recovery will not be effective, and the image will suffer from extra SNR degradation. This problem is potentially encountered on the most inferior brain slices, which are close to (or through) multiple air cavities with complicated configuration. There, the inhomogeneous field varies rapidly over space, and a simple relationship between offsets and through-plane dephasing may not exist.

It is also possible that the correlation assumption does hold well, but only within confined image regions. For example, on a particular inferior brain slice, image regions proximal to the sinuses may exhibit linear correlation with a proportionality constant very different from that in regions close to the middle ear spaces. In that case, it will be impossible to find a single SPSP pulse that simultaneously recovers signals at all those regions.

Note that multi-region signal recovery was well achieved in our demonstration (Fig. 6.9), because the metal pieces were identical and placed at the same distance from the imaging plane. It warranted that the field distortion at the three signal loss sites resembled each other, and hence could be tackled altogether with one single SPSP pulse.

Lastly, it is noteworthy that a fundamental limitation underlies both the 3DTRF and SPSP signal recovery methods: they are both engineered to precompensate only the through-plane dephasing, and they do not address the other dephasing components caused by field inhomogeneity, namely, in-plane dephasing and phase error during data readout. It implies that even if the pulse design methods are supreme in through-plane phase precompensation, images can still be severely marred because of the other dephasing problems. As an example, the single-interleave, low-resolution brain image (Fig. 6.12c) could not be improved (Fig. 6.12d) with the SPSP pulse, even though the pulse was very effective in the multi-interleave high-resolution scenario (Figs. 6.12a,b). Sophisticated image reconstruction methods (e.g., Refs. [16, 78]) can help to resolve these problems. On the other hand, localized shimming methods, either passive [39] or active [40, 41], target to improve the *overall* field homogeneity. For this reason, they may be the preferred signal recovery strategy, either alone or in conjunction with the RF pulse methods.

CHAPTER 7

Conclusion and future work

7.1 Effectiveness and limitations

In this thesis, I have explored two distinct approaches of RF pulse design for signal recovery in T_2^*-weighted fMRI – an advanced version of the original 3DTRF method, and a novel method using SPSP selective excitation. In phantom and human experiments, both methods were demonstrated to be effective in through-plane phase precompensation, and hence capable of recovering signal loss. The experiments also provided evidence that the pulses selectively excited slice volumes with good accuracy.

Nevertheless, the signal recovery methods have their limitations. First, they are both unable to provide satisfactory signal recovery in the most inferior slices very close to (or through) the air cavities. There, the magnetic field is so severely distorted that the design methods cannot accommodate. For 3DTRF pulses, the fatal problem in that region is the high frequency offset magnitude. High offsets are difficult, if not impossible, for the iterative design to counteract toward achieving the desired pattern. The rapid in-plane field variations there are also detrimental because the in-plane dimensions are phase-encoded with the EV trajectory. For the SPSP pulses, the rapid field variations in the inferior brain lead to violation of the correlation assumption that signal recovery relies on, causing ineffective recovery and extra signal loss.

The second limitation is inherent to the very concept of phase precompensation that underlies both pulse designs. The methods are engineered to precompensate *only* the through-plane component of the dephasing phenomenon. They do not address the other components, namely, in-plane dephasing and phase error during readout (Chapter 1). As a result, even if through-plane precompensation is accomplished, images can still be marred because of those other dephasing components. The benefit of through-plane precompensation is prominent only when those components are reduced via usage of high resolution and multiple readout interleaves. This issue was perfectly illustrated in the human experiment of the SPSP method – The recovery effect of the SPSP pulse, proven in the high-resolution and multiple-interleave scenario, was "covered up" in the low-resolution, single-interleave case (Fig. 6.12).

7.2 Costs

Inevitably, there are costs in applying the pulse designs to fMRI studies. The primary cost is that both the 3DTRF and SPSP pulse designs require very large amount of computations, because they commonly involve minimization of a quadratic cost function comprising a very large system matrix. As a result, the designs are very time-consuming and memory intensive. In particular, the long computational time is a big obstacle to the practical use of 3DTRF pulses. During an fMRI session, multiple 3DTRF pulses (for different slice locations) have to be computed online using freshly acquired field maps. It necessitates very fast computers running efficient design codes (e.g., code in C), or perhaps multi-thread parallel computation that can carry out multiple designs simultaneously. Issues in fast implementation of the method can itself be very challenging. On the other hand, SPSP signal recovery is free of this computation burden, because the SPSP pulses can be computed offline prior to the experiment and stored for repeated use. It allows

use of design codes that are programmer-friendly but not optimally efficient (e.g., code in Matlab).

Another cost is the reduction in temporal resolution of the fMRI study. However, as discussed in Chapter 4 for the 3DTRF case, the cost is lower than that involved in methods such as z-shimming and using thin slices. Also, compared to the standard sinc pulse, the sophisticated pulse designs are less robust to motion that causes field changes between field map measurement and pulse application.

7.3   Feasibility for routine use

After considering the pulse designs' effectiveness, limitations and costs, we face the ultimate question: is it feasible to use the pulses in routine fMRI studies? In my opinion, it could be worthwhile, if the methods were further improved such that the pulses were effective over the entire brain and with a higher level of robustness. Future shimming techniques, either global or localized, could potentially homogenize the field much more effectively, rendering the problem "easier" for the pulse designs. Coordinated use of shimming techniques and precompensatory pulse designs (especially the SPSP pulses) might prove to be powerful for acquiring functional data from everywhere in the brain. For the 3DTRF method, the computational time must be reduced so that online pulse design is affordable. Lastly, the other dephasing components (in-plane dephasing, phase error during readout) have to be handled as well. Advanced image reconstruction methods from our group, such as the iterative reconstruction [16] and conjugate phase with spatially-variant density compensation [78], could be used for that purpose.

7.4   Future work

In this final section I summarize interesting future work opportunities (ordered not based on priorities):

Enforcing the correlation assumption in the SPSP pulse design

The SPSP pulses are played out in the RF and z-gradient channels. It is feasible that we apply constant gradients in the transverse plane (G_x, G_y), simultaneous with the SPSP pulse, for the purpose of enforcing the offset-gradient correlation. By doing so, we can maneuver the in-plane field variations to place susceptibility-induced through-plane phase variations "at the appropriate spectral locations", so that through-plane spins pick up appropriate phase values for precompensation. Now, for each slice location, the designer has to decide on which SPSP pulse to apply, *and* the suitable G_x and G_y magnitudes for correlation enforcement. This is potentially a non-trivial but rewarding development direction.

Generalizing the pulse designs for parallel excitation

The pulse designs can be generalized for parallel excitation using multiple transmit coils. Because of the in-plane excitation selectivity introduced by the localized coils, the number of phase-encoding locations for the 3DTRF pulses could be drastically lowered. Signal recovery could be achieved with significantly shorter pulses. As for the SPSP pulses, in-plane excitation selectivity can be introduced to the original SPSP excitation pattern, such that the SPSP response at different in-plane regions is different. This could be beneficial for inferior brain slices within which the offset-gradient correlation varies regionally.

Concurrent use of signal recovery pulses and sophisticated image reconstruction method

In standard fMRI sequences with low resolution and single acquisition interleave, the benefit of through-plane phase precompensation is veiled by the other dephasing components, such as in-plane dephasing and phase error during readout. Iterative reconstruction [16] or the non-iterative conjugate phase method with spatially-variant density compensation [78] should be applied to reconstruct images acquired with the signal recovery pulses. We predict that the benefit of through-plane phase precompensation will become more prominent after those other dephasing components are handled.

Concurrent use of signal recovery pulses and advanced shimming methods

Passive [39] or active [40] localized shimming is effective in improving the *overall* field homogeneity in the subject head. Recently, researchers also proposed that the linear and high-order shim values can be dynamically updated from slice to slice [112]. Concurrent use of these state-of-the-art shimming methods and the RF pulse designs can potentially be efficacious in recovering all the signal loss in the inferior brain.

Acquiring BOLD signals from the recovered regions

So far, we take it for granted that BOLD contrast can be expected at image regions recovered with the pulse designs. This needs to be experimentally validated, perhaps with a breath-holding block design paradigm.

Implementing the pulse designs in routine fMRI sequences

The implementation of the pulse designs in routine fMRI sequences can be rather challenging. For the 3DTRF method, field maps have to be acquired and then automatically passed into pulse design. Subsequently the computed designs have to be installed into the pulse sequence. The sequence should be capable of deploying different pulse designs

at different slice locations. As for the SPSP method, the pulse sequence have to retrieve and deploy precomputed pulses, based on choices made prior to the experiment, or field maps estimated online. In all cases, the pulse designs need to be frequency-modulated for off-center slice locations.

Exploring alternative functional contrast mechanisms

The fMRI community should keep exploring alternative functional contrast mechanisms that are not coupled to susceptibility-induced artifacts. Recently proposed contrast methods, using steady-state-free -precession mechanism [113, 114] or diffusion weighting [115], are promising ways for acquiring images without susceptibility-induced artifacts, although they have their own hurdles to overcome.

BIBLIOGRAPHY

BIBLIOGRAPHY

[1] Detre JA and Wang J. Technical aspects and utility of fMRI using BOLD and ASL. *Clin Neurophysiol*, 113(5):621–634, May 2002.

[2] Ogawa S, Tank DW, Menon R, Ellerman JM, Kim S, Merkle H, and Ugurbil K. Intrinsic signal changes accompanying sensory stimulation: functional brain mapping with magnetic resonance imaging. *Proc Natl Acad Sci USA*, 89:5951–5955, 1992.

[3] Kwong KK, Belliveau JW, Chesler DA, Goldberg IE, Weisskoff RM, Poncelet BP, Kennedy DN, Hoppel BE, Cohen MS, and Turner R. Dynamic magnetic resonance imaging of human brain activity during primary sensory stimulation. *Proc Natl Acad Sci U S A*, 89(12):5675–5679, Jun 1992.

[4] Ogawa S, Menon RS, Tank DW, Kim SG, Merkle H, Ellermann JM, and Ugurbil K. Functional brain mapping by blood oxygenation level-dependent contrast magnetic resonance imaging. a comparison of signal characteristics with a biophysical model. *Biophys J*, 64(3):803–812, Mar 1993.

[5] Mandeville JB, Marota JJ, Ayata C, Moskowitz MA, Weisskoff RM, and Rosen BR. MRI measurement of the temporal evolution of relative $CMRO_2$ during rat forepaw stimulation. *Magn Reson Med*, 42(5):944–951, Nov 1999.

[6] Ugurbil K, Toth L, and Kim DS. How accurate is magnetic resonance imaging of brain function? *Trends Neurosci*, 26(2):108–114, Feb 2003.

[7] Stehling MK, Turner R, and Mansfield P. Echo-planar imaging: magnetic resonance imaging in a fraction of a second. *Science*, 254(5028):43–50, Oct 1991.

[8] Meyer CH, Hu BS, Nishimura DG, and Macovski A. Fast spiral coronary artery imaging. *Magn Reson Med*, 28(2):202–13, 1992.

[9] Menon RS, Ogawa S, Tank DW, and Ugurbil K. 4 Tesla gradient recalled echo characteristics of photic stimulation-induced signal changes in the human primary visual cortex. *Magn Reson Med*, 30:380–386, 1993.

[10] Gati JS, Menon RS, Ugurbil K, and Rutt BK. Experimental determination of the BOLD field strength dependence in vessels and tissue. *Magn Reson Med*, 38:296–302, 1997.

[11] Kruger G, Kastrup A, and Glover GH. Neuroimaging at 1.5 T and 3.0 T: comparison of oxygenation-sensitive magnetic resonance imaging. *Magn Reson Med*, 45:595–604, 2001.

[12] Yacoub E, Shmuel A, Pfeuffer J, Van De Moortele PF, Adriany G, Andersen P, Vaughan JT, Merkle H, Ugurbil K, and Hu X. Imaging brain function in humans at 7 Tesla. *Magn Reson Med*, 45:588–594, 2001.

[13] Lipschutz B, Friston KJ, Ashburner J, Turner R, and Price CJ. Assessing study-specific regional variations in fMRI signal. *Neuroimage*, 13(2):392–398, 2001.

[14] Li S, Dardzinski BJ, Collins CM, Yang QX, and Smith MB. Three-dimensional mapping of the static magnetic field inside the human head. *Magn Reson Med*, 36(5):705–14, 1996.

[15] Noll DC, Meyer CH, Pauly JM, Nishimura DG, and Macovski A. A homogeneity correction method for magnetic resonance imaging with time-varying gradients. *IEEE Trans Med Imag*, 10(4):629–637, 1991.

[16] Sutton BP, Noll DC, and Fessler JA. Fast, iterative image reconstruction for MRI in the presence of field inhomogeneities. *IEEE Trans Med Imag*, 22(2):178–188, 2003.

[17] Fessler JA, Lee S, Olafsson VT, Shi HR, and Noll DC. Toeplitz-based iterative image reconstruction for MRI with correction for magnetic field inhomogeneity. *IEEE Trans Signal Proc*, 53(9):3393–3402, 2005.

[18] Nishimura DG. *Principles of magnetic resonance imaging*. 1996.

[19] Yoo SS, Guttmann CR, and Panych LP. Multiresolution data acquisition and detection in functional MRI. *Neuroimage*, 14(6):1476–1485, 2001.

[20] Haacke EM, Tkach JA, and Parrish TB. Reduction of T_2^* dephasing in gradient field-echo imaging. *Radiology*, 170(2):457–462, Feb 1989.

[21] Frahm J, Merboldt KD, and Hänicke W. Functional MRI of human brain activation at high spatial resolution. *Magn Reson Med*, 29(1):139–144, Jan 1993.

[22] Chen NK, Dickey CC, Yoo SS, Guttmann CR, and Panych LP. Selection of voxel size and slice orientation for fMRI in the presence of susceptibility field gradients: application to imaging of the amygdala. *Neuroimage*, 19(3):817–825, 2003.

[23] Merboldt KD, Finsterbusch J, and Frahm J. Reducing inhomogeneity artifacts in functional mri of human brain activation-thin sections vs gradient compensation. *J Magn Reson*, 145:184–191, 2000.

[24] Glover GH. 3D z-shim method for reduction of susceptibility effects in BOLD fMRI. *Magn Reson Med*, 42:290–299, 1999.

[25] Ojemann JG, Akbudak E, Snyder AZ, McKinstry RC, Raichle ME, and Conturo TE. Anatomic localization and quantitative analysis of gradient refocused echo-planar fMRI susceptibility artifacts. *Neuroimage*, 6(3):156–167, Oct 1997.

[26] Deichmann R, Gottfried JA, Hutton C, and Turner R. Optimized EPI for fMRI studies of the orbitofrontal cortex. *Neuroimage*, 19:430–441, 2003.

[27] De Panfilis C and Schwarzbauer C. Positive or negative blips? The effect of phase encoding scheme on susceptibility-induced signal losses in EPI. *Neuroimage*, 25(1):112–121, 2005.

[28] Glover GH and Law CS. Spiral-in/out BOLD fMRI for increased SNR and reduced susceptibility artifacts. *Magn Reson Med*, 46(3):515–522, 2001.

[29] Li TQ, Takahashi A, Wang Y, Mathews V, and Glover GH. Dual-echo spiral in/in acquisition method for reducing magnetic susceptibility artifacts in blood-oxygen-level-dependent functional magnetic resonance imaging. *Magn Reson Med*, 55(2):325–34, 2006.

[30] Frahm J, Merboldt KD, and Haenicke W. Direct FLASH MR imaging of magnetic field inhomogeneities by gradient compensation. *Magn Reson Med*, 6:474–480, 1988.

[31] Frahm J, Merboldt KD, and Haenicke W. The influence of the slice-selection gradient on functional MRI of human brain activation. *J Magn Reson Imag*, 103:91–93, 1994.

[32] Ordidge RJ, Gorell JM, Deniau JC, Knight RA, and Helpern JA. Assessment of relative brain iron concentrations using T_2-weighted and T_2^*-weighted MRI at 3 Tesla. *Magn Reson Med*, 32(3):335–341, Sep 1994.

[33] Constable R. Functional MR imaging using gradient-echo echo-planar imaging in the presence of large static field inhomogeneities. *J Magn Reson Imag*, 5(6):746–752, 1995.

[34] Song AW. Single-shot EPI with signal recovery from the susceptibility-induced losses. *Magn Reson Med*, 46:407–411, 2001.

[35] Heberlein KA and Hu X. Simultaneous acquisition of gradient-echo and asymmetric spin-echo for single-shot z-shim: Z-SAGA. *Magn Reson Med*, 51(1):212–216, 2004.

[36] Yang QX, Dardzinski BJ, Li S, Eslinger PJ, and Smith MB. Removal of local field gradient artifacts in T_2^*-weighted images at high fields by gradient-scho slice excitation profile imaging. *Magn Reson Med*, 39:402–409, 1998.

[37] Constable R and Spencer D. Composite image formation in z-shimmed functional MR imaging. *Magn Reson Med*, 42:110–117, 1999.

[38] Du YP, Dalwani M, Wylie K, Claus E, and Tregellas JR. Reducing susceptibility artifacts in fMRI using volume-selective z-shim compensation. *Magn Reson Med*, 57(2):396–404, Feb 2007.

[39] Wilson JL, Jenkinson M, and Jezzard P. Optimization of static field homogeneity in human brain using diamagnetic passive shims. *Magn Reson Med*, 48(5):906–914, 2002.

[40] Hsu JJ and Glover GH. Mitigation of susceptibility-induced signal loss in neuroimaging using localized shim coils. *Magn Reson Med*, 53(2):243–248, 2005.

[41] Wong EC and Mazaheri Y. Shimming of the inferior frontal cortex using an external local shim coil. In *Proceedings of the 12th Annual Meeting of ISMRM, Kyoto*, page 520, 2004.

[42] Cusack R, Russell B, Cox SM, De Panfilis C, Schwarzbauer C, and Ansorge R. An evaluation of the use of passive shimming to improve frontal sensitivity in fMRI. *Neuroimage*, 24(1):82–91, Jan 2005.

[43] Cho Z and Ro Y. Reduction of susceptibility artifact in gradient-echo imaging. *Magn Reson Med*, 23(1):193–200, 1992.

[44] Chen N and Wyrwicz A. Removal of intravoxel dephasing artifact in gradient-echo images using a field-map based RF refocusing technique. *Magn Reson Med*, 42:807–812, 1999.

[45] Glover GH and Lai S. Reduction of susceptibility effects in BOLD fMRI using tailored RF pulses. *Proceedings of the 5th Annual Meeting of ISMRM*, 1997.

[46] Stenger VA, Boada FE, and Noll DC. Three-dimensional tailored RF pulses for the reduction of susceptibility artifacts in T_2^*-weighted functional MRI. *Magn Reson Med*, 44:525–531, 2000.

[47] Pauly JM, Nishimura DG, and Macovski A. A k-space analysis of small-tip-angle excitation. *J Magn Reson*, 81:43–56, 1989.

[48] Pauly JM, Hu BS, Wang SJ, Nishimura DG, and Macovski A. A three-dimensional spin-echo or inversion pulse. *Magn Reson Med*, 29:2–6, 1993.

[49] Meyer CH, Pauly JM, Macovski A, and Nishimura DG. Simultaneous spatial and spectral selective excitation. *Magn Reson Med*, 15(2):287–304, Aug 1990.

[50] Bloch F. Nuclear induction. *Phys Rev*, 70:460–473, 1946.

[51] Twieg DB. The k-trajectory formulation of the NMR imaging process with applications in analysis and synthesis of imaging methods. *Med Phys*, 10:610–621, 1983.

[52] Brown TR, Kincaid BM, and Ugurbil K. NMR chemical shift imaging in three dimensions. *Proc Natl Acad Sci USA*, 79:3523–3526, 1982.

[53] Ljunggren S. A simple graphical representation of fourier-based imaging methods. *J Magn Reson*, 54:338–343, 1983.

[54] Hinshaw WS and Lent AH. An introduction to NMR imaging: from the bloch equation to the imaging equation. In *Proceedings of IEEE*, volume 71, pages 338–350, 1983.

[55] Hoult DI. The solution of the bloch equations in the presence of a varying B1 field. *J Magn Reson*, 35:66–86, 1979.

[56] Bracewell RN. *The Fourier Transform and its applications*. McGraw-Hill, 1978.

[57] Pauly JM, Nishimura DG, and Macovski A. A linear class of large-tip-angle selective excitation pulses. *J Magn Reson*, 82:571–587, 1989.

[58] Börnert P and Aldefeld B. On spatially selective RF excitation and its analogy with spiral MR image acquisition. *Magn Reson Materials in Phys, Bio and Med*, 7:166–178, 1998.

[59] Schomberg H and Börnert P. Off-resonance correction of *n*D spatially selective RF pulses. In *Proceedings of the 6th Annual Meeting of ISMRM, Sydney*, page 2059, 1998.

[60] Spielman D, Pauly J, Macovski A, and Enzmann D. Spectroscopic imaging with multidimensional pulses for excitation: SIMPLE. *Magn Reson Med*, 19:67–84, 1991.

[61] Block W, Pauly J, Kerr A, and Nishimura D. Consistent fat suppression with compensated spectral-spatial pulses. *Magn Reson Med*, 38(2):198–206, Aug 1997.

[62] Schick F. Simultaneous highly selective MR water and fat imaging using a simple new type of spectral-spatial excitation. *Magn Reson Med*, 40(2):194–202, Aug 1998.

[63] Zur Y. Design of improved spectral-spatial pulses for routine clinical use. *Magn Reson Med*, 43(3):410–420, Mar 2000.

[64] Morrell G and Macovski A. Three-dimensional spectral-spatial excitation. *Magn Reson Med*, 37(3):378–386, Mar 1997.

[65] Katscher U, Börnert P, Leussler C, and van den Brink JS. Transmit SENSE. *Magn Reson Med*, 49:144–150, 2003.

[66] Zhu Y. Parallel excitation with an array of transmit coils. *Magn Reson Med*, 51:775–784, 2004.

[67] Sodickson DK and Manning WJ. Simultaneous acquisition of spatial harmonics (SMASH): fast imaging with radiofrequency coil arrays. *Magn Reson Med*, 38(4):591–603, Oct 1997.

[68] Pruessmann KP, Weiger M, Scheidegger MB, and Boesiger P. SENSE: sensitivity encoding for fast MRI. *Magn Reson Med*, 42(5):952–962, Nov 1999.

[69] Griswold MA, Jakob PM, Heidemann RM, Nittka M, Jellus V, Wang J, Kiefer B, and Haase A. Generalized autocalibrating partially parallel acquisitions (*grappa*). *Magn Reson Med*, 47(6):1202–1210, Jun 2002.

[70] Saekho S, Boada FE, Noll DC, and Stenger VA. Small tip angle three-dimensional tailored radiofrequency slab-select pulse for reduced B1 inhomogeneity at 3 T. *Magn Reson Med*, 53(2):479–484, 2005.

[71] Saekho S, Yip CY, Noll DC, Boada FE, and Stenger VA. Fast-kz three-dimensional tailored radiofrequency pulse for reduced B1 inhomogeneity. *Magn Reson Med*, 55(4):719–724, Apr 2006.

[72] Hardy CJ, Cline HE, and Bottomley PA. Correcting for nonuniform k-space sampling in two-dimensional NMR selective excitation. *J Magn Reson Imag*, 87:639–645, 1990.

[73] Hoge RD, Kwan RK, and Pike GB. Density compensation functions for spiral MRI. *Magn Reson Med*, 38:117–128, 1997.

[74] Stenger VA, Boada FE, and Noll DC. Variable-density spiral 3D tailored RF pulses. *Magn Reson Med*, 50:1100–1106, 2003.

[75] Stenger VA, Boada FE, and Noll DC. Multishot 3D slice-select tailored RF pulses for MRI. *Magn Reson Med*, 48:157–165, 2002.

[76] Schomberg H. Off-resonance correction of MR images. *IEEE Trans Med Imag*, 18(6):481–495, 1999.

[77] Yip CY, Fessler JA, and Noll DC. Iterative RF pulse design for multi-dimensional, small-tip-angle selective excitation. *Magn Reson Med*, 54(4):908–917, 2005.

[78] Noll DC, Fessler JA, and Sutton BP. Conjugate phase MRI reconstruction with spatially variant sample density correction. *IEEE Trans Med Imag*, 24(3):325–336, 2005.

[79] Pipe JG and Menon P. Sampling density compensation in MRI: rationale and an iterative numerical solution. *Magn Reson Med*, 41:179–186, 1999.

[80] Conolly S, Nishimura DG, and Macovski A. Optimal control solutions to the magnetic resonance selective excitation problem. *IEEE Trans Med Imag*, MI-5(2):106–115, 1986.

[81] Murdoch JB, Lent AH, and Kritzer MR. Computer-optimized narrowband pulses for multislice imaging. *J Magn Reson*, 74:226–263, 1987.

[82] Conolly S. *Magnetic resonance selective excitation*. PhD thesis, Stanford University, CA, 1989.

[83] Lurie DJ. A systematic design procedure for selective pulses in NMR imaging. *Magn Reson Imag*, 3:235–243, 1985.

[84] O'Donnell M and Adams WJ. Selective time-reversal pulses for NMR imaging. *Magn Reson Imag*, 3:377–382, 1985.

[85] Hardy CJ, Bottomley PA, O'Donnell M, and Roemer P. Optimization of two-dimensional spatially selective NMR pulses by simulated annealing. *J Magn Reson*, 77:233–250, 1988.

[86] Harshbarger TB and Twieg DB. Iterative reconstruction of single-shot spiral MRI with off resonance. *IEEE Trans Med Imag*, 18(3):196–205, 1999.

[87] Munger P, Crelier GR, Peters TM, and Pike GB. An inverse problem approach to the correction of distortion in EPI images. *IEEE Trans Med Imag*, 19(7):681–689, 2000.

[88] Bazaraa MS, Sherali HD, and Shetty CM. *Nonlinear Programming*. Wiley, New York, 2nd edition, 1993.

[89] Glover GH. Simple analytic spiral K-space algorithm. *Magn Reson Med*, 42:412–415, 1999.

[90] Schneider E and Glover GH. Rapid in vivo proton shimming. *Magn Reson Med*, 18:335–347, 1991.

[91] Schröder C, Börnert P, and Aldefeld B. Spatial excitation using variable-density spiral trajectories. *J Magn Reson Imag*, 18:136–141, 2003.

[92] Nehrke K, Börnert P, Groen J, Smink J, and Böck JC. On the performance and accuracy of 2D navigator pulses. *J Magn Reson Imag*, 17(8):1173–1181, 1999.

[93] Fessler JA. Penalized weighted least-squares image reconstruction for positron emission tomography. *IEEE Trans Med Imag*, 13(2):290–300, 1994.

[94] Grissom WA, Yip CY, Zhang Z, Stenger VA, Fessler JA, and Noll DC. A spatial domain method for the design of RF pulses in multi-coil parallel excitation. *Magn Reson Med*, 56(3):620–9, 2006.

[95] Ullmann P, Junge S, Wick M, Seifert F, Ruhm W, and Hennig J. Experimental analysis of parallel excitation using dedicated coil setups and simultaneous RF transmission on multiple channels. *Magn Reson Med*, 54(4):994–1001, Oct 2005.

[96] Setsompop K, Wald LL, Alagappan V, Gagoski B, Hebrank F, Fontius U, Schmitt F, and Adalsteinsson E. Parallel RF transmission with eight channels at 3 Tesla. *Magn Reson Med*, 56(5):1163–1171, Nov 2006.

[97] Yip CY, Fessler JA, and Noll DC. Advanced three-dimensional tailored RF pulse for signal recovery in T_2^*-weighted functional MRI. *Magn Reson Med*, 56(5):1050–9, 2006.

[98] Noll DC. *Reconstruction techniques for magnetic resonance imaging*. PhD thesis, Stanford University, CA, 1991.

[99] Man LC, Pauly JM, and Macovski A. Multifrequency interpolation for fast off-resonance correction. *Magn Reson Med*, 37:785–792, 1997.

[100] Mansfield P, Howseman AM, and Ordidge RJ. Volumar imaging using NMR spin echos: echo-volumar imaging (EVI at 0.1 T. *J Phys E: Sci Instrum*, 22:324–330, 1989.

[101] Oelhafen M, Pruessmann KP, Kozerke S, and Boesiger P. Calibration of echo-planar 2D-selective RF excitation pulses. *Magn Reson Med*, 52:1136–1145, 2004.

[102] Fessler JA and Sutton BP. Nonuniform fast Fourier transforms using min-max interpolation. *IEEE Trans Signal Proc*, 51(2):560–574, 2003.

[103] Fessler JA, Desmond Yeo, and Noll DC. Regularized fieldmap estimation in MRI. In *Proc IEEE Intl Symp Biomed Imag*, 2006.

[104] Noll DC and Stenger VA. A 3D tailored RF pulse asymmetric spin-echo pulse sequence for susceptibility correction in functional MRI. *Proceedings of the 10th Annual Meeting of ISMRM, Honolulu*, 2002.

[105] Yip CY, Grissom WA, Fessler JA, and Noll DC. Joint design of trajectory and RF pulses for parallel excitation. *Magn Reson Med*, 58(3):598–604, 2007.

[106] Katscher U, Röhrs J, and Börnert P. Basic considerations on the impact of the coil array on the performance of Transmit SENSE. *MAGMA*, 18(2):81–88, May 2005.

[107] Levin YS, Pisani LJ, Spielman DM, and Pauly JM. Trajectory optimization for variable-density spiral two-dimensional excitation. In *Proceedings of the 14th Annual Meeting of ISMRM, Seattle*, number 3012, 2006.

[108] Nelder JA and Mead R. A simplex method for function minimization. *Comput. J.*, 7:308–313, 1965.

[109] Griswold MA, Kannengiesser S, Müller M, and Jakob PM. Autocalibrated accelerated parallel excitation. In *Proceedings of the 13th Annual Meeting of ISMRM, Miami*, number 2435, 2005.

[110] Xu D, Ying L, Jacob M, and Liang Z-P. Optimizing SENSE for dynamic imaging. In *Proceedings of the 13th Annual Meeting of ISMRM, Miami*, number 2419, 2005.

[111] Lange K, Hunter DR, and Yang I. Optimization transfer using surrogate objective functions. *J. Computational and Graphical Stat.*, 9(1):1–20, 2000.

[112] Koch KM, McIntyre S, Nixon TW, Rothman DL, and de Graaf RA. Dynamic shim updating on the human brain. *J Magn Reson*, 180(2):286–296, Jun 2006.

[113] Miller KL, Hargreaves BA, Lee J, Ress D, deCharms RC, and Pauly JM. Functional brain imaging using a blood oxygenation sensitive steady state. *Magn Reson Med*, 50(4):675–683, Oct 2003.

[114] Miller KL, Smith SM, Jezzard P, and Pauly JM. High-resolution FMRI at 1.5T using balanced SSFP. *Magn Reson Med*, 55(1):161–170, Jan 2006.

[115] Le Bihan D, Urayama S, Aso T, Hanakawa T, and Fukuyama H. Direct and fast detection of neuronal activation in the human brain with diffusion MRI. *Proc Natl Acad Sci U S A*, 103(21):8263–8268, May 2006.